CRANFIELD UNIVERSITY

Fabian Duarte Martinez

# Investigation into the environmental assisted crack initiation mechanism of CMSX-4 in simulated aero engine environments at 450 - 550°C

School of Aerospace, Transport and Manufacturing

PhD

Academic Year: 2018 - 2023

Supervisor: Prof. J. R. Nicholls

Associate Supervisors: Dr Simon Gray, Dr Gustavo Castelluccio

03/2023

CRANFIELD UNIVERSITY

School of Aerospace, Transport and Manufacturing

PhD

Academic Year 2018 – 2023

Fabian Duarte Martinez

# Investigation into the environmental assisted crack initiation mechanism of CMSX-4 in simulated aero engine environments at 450 - 550°C

Supervisor: Prof. J. R. Nicholls

Associate Supervisors: Dr S. Gray and Dr G. Castelluccio

March 2023

## Abstract

The aviation industry has continued to increase the efficiency of gas turbine engines, which are now designed to operate on a wide variety of flight routes. In general, the efficiency drive has led to components spending longer times at temperatures, where accelerated corrosion can occur. This has led to a complex degradation mechanism being identified in the lower shank region under the platform of single-crystal turbine blades.

This research aims to understand the mechanism of crack initiation due to the synergistic effect of stress and high temperature corrosion environments on CMSX-4 in the lower operating temperature range, 450°C - 550°C, of an aero gas turbine blade. The first part of the investigation consisted in comparing the effect of different salt deposits in a 50 ppm $SO_2$ - air environment at 550°C. A 50 ppm $SO_2$ – air concentration was considered because the air going through the lower shank is fed directly from the compressor, and not from the combustor (which is the main source of sulphur). Characterisation of the resulting scales were carried out using scanning electron microscopy, energy dispersive spectroscopy and X-ray diffraction. Results from thermodynamic modelling are also presented. The first part of the investigation showed that CMSX-4 sample under an applied stress and no applied salt did not experience accelerated corrosion attack or crack formation when exposed to 50 ppm $SO_2$ - air in a 400-hour period. The same observation was made for a CMSX-4 sample under an applied stress and salted with $CaSO_4$. Sea salt caused accelerated corrosion attack with cracks up to 1.3 mm through the substrate formed after 400 hours of exposure.

Further tests using NaCl salt in 50 ppm $SO_2$ – air showed that cracks can initiate after just 10 minutes of exposure at 550°C. Crack growth rates are significantly reduced after two hours of exposure within a 50-hour salt cycle. Cracks with NaCl in 50 ppm $SO_2$ – air have also been observed at temperatures as low as 450°C.

When NaCl salt was applied to CMSX-4 and exposed to air only for 50 hours, the corrosion attack was reduced considerably, and the initiation of cracks is either suppressed or significantly delayed beyond a 50-hour period. Although this PhD

has only focused on a 50-hour period, longer exposure times should be carried out to determine if air exposures delay crack initiation time, or if crack initiation is completely supressed.

This thesis has therefore shown that the interaction of stress, NaCl and a sulphur-containing environment are critical to cause early crack initiation in single crystal nickel-based superalloys in the temperature range 450 - 550°C. The effect of having small concentrations of moisture in the gaseous environment or as inclusions retained in the salt are still to be investigated. A working hypothesis is that that the interaction of alkali chlorides with a sulphur-containing atmosphere is the trigger to a self-sustaining cycle where metal chloride formation, vaporisation and oxidation leads to high amounts of $H_2$ formed at the scale/alloy interface. Potentially, the $H_2$ formed at the alloy/scale interface may dissociate into atomic hydrogen, and lead to hydrogen embrittlement. For further verification of this hypothesis, a set of tests have been suggested.

# Acknowledgements

First and foremost, I would like to express my gratitude to Professor John Nicholls, Dr Simon Gray and Dr Gustavo Castelluccio for their enthusiastic supervision throughout the course of this project.

Special thanks to Professor Gordon Tatlock and Dr Karl Dawson at Liverpool University for offering their technical microscopy expertise, discussions and assisting greatly with this project. In addition, also a special thanks to Dr Maadhav Kothari and collaborators at ZEISS for supporting this work with NanoXCT characterisation

Also, I want to thank Rolls Royce plc. for supporting this thesis and providing their technical expertise, especially to Jonathan Leggett, Julian Mason-Flucke, Grant Gibson, Ian Edmonds and Jane Woolrich for fruitful discussions.

Finally, thanks also to Dr Nicolau Morar and Dr Adnan Syed, who have provided great technical support during this project. Their help has been very valuable.

# Table of Contents

# List of Tables

# List of Figures

# List of Equations

## List of Abbreviations

| | |
|---|---|
| APB | Antiphase boundary |
| BSE | Backscattered secondary electrons |
| CMSX-4 | Canon Muskegon single-crystal 4 |
| XCT | X-ray computer tomography |
| EDS | Energy dispersive x-ray spectroscopy |
| FE | Finite element |
| STEM | Secondary transmission electron microscope |
| ODP | Oxygen diffusion path |
| SCO | Secondary crystallographic orientation |
| DE | Dynamic embrittlement |
| SAGBO | Stress assisted grain boundary oxidation |
| FIC | Film induced cleavage |
| SXRD | Synchrotron X-ray diffraction |
| HELP | Hydrogen enhanced localised plasticity |
| HID | Hydrogen induced decohesion |
| HSSCC | Hot salt stress corrosion cracking |
| IPA | Isopropyl alcohol |
| NanoXCT | Nano X-ray Computed tomography |

# 1 Introduction

## 1.1 Background

Gas turbines comprise the core of conventional aircraft propulsion systems. Since their first use, there have been significant technological improvements that continue to expand their performance capability. These improvements have taken place due to developments in aerodynamics, materials science, mechanics, and fluid dynamics.

Currently, gas turbines are reaching turbine inlet temperatures of approximately 1600°C, and components such as turbine blades are subjected to high centrifugal stresses and aggressive high temperature environments. These aggressive environments ultimately degrade the performance of turbine blades through mechanisms such as creep, fatigue, and high temperature corrosion. To improve the performance of these components in these aggressive environments, considerable research is therefore undertaken to develop new alloys, coating systems, heat treatments and advanced manufacturing processes.

A complex degradation mechanism has been identified in the lower shank (region under the platform) of intermediate pressure turbine blades, which has led to a considerable increase in maintenance costs. The lower shank of turbine blades operates at moderate temperature ranges (450-700°C) and higher stresses than other regions of the blade.

At temperatures between 450 and 550°C the thermodynamic driving force for high temperature corrosion is significantly reduced. So, although corrosion alone may not be the predominant damage mode, it may typically be considered as the precursor for the initiation of cracks when components are subjected to external stresses. The synergistic interaction between mechanical loads and the environment can be catastrophic, therefore its characterisation and understanding are of key importance to develop new alloy systems, protection methods and lifing methods.

Deposit-induced high temperature corrosion is a common corrosion mechanism affecting turbine blade components in aero and industrial gas turbines. It occurs due to the sulphur-containing gases and inlet air contaminants reacting and depositing on turbine components. When constituents such as NaCl react with sulphur containing gases, that are produced in the combustion process, it forms $Na_2SO_4$ that deposits on the blades. As a result, deposits of $Na_2SO_4$ leads to two well-known types of corrosion, which are defined as Type I and Type II hot corrosion. Type I hot corrosion typically occurs between 800-900°C and Type II hot corrosion between 670-800°C. In Type I hot corrosion, a liquid melt of $Na_2SO_4$ is produced, while in Type II hot corrosion a eutectic melt such as $NiSO_4$-$Na_2SO_4$ or $CoSO_4$-$Na_2SO_4$, is produced.

However, the temperatures present in the lower shank region are below those typical of Type I and Type II hot corrosion. Therefore, there is a gap in the research aiming to understand the corrosion assisted cracking mechanisms that operate below 600°C and at high stress. This leads to the catastrophic failure of turbine blade components through stress assisted corrosion.

Based on literature findings and discussions with Rolls Royce plc, $Na_2SO_4$, $CaSO_4$, and sea salt were considered important contaminants. As a starting point, $CaSO_4$ was considered given that it is typically present as a deposit in the lower shank region of blades removed from engine service. $Na_2SO_4$ given that it also deposits on turbine blade components and is the main driver of hot corrosion. Ultimately, sea salt was considered because it is present as part of the atmospheric aerosol and enters the gas turbine as an air inlet contaminant when flying over marine environments.

## 1.2 Project scope and thesis structure

The aim of this thesis is to examine the synergistic effect of stress, salt chemistries and high temperature gases on the damage processes that occur in the early stages of crack formation a single nickel-based superalloy, CMSX-4, at moderate temperatures (450 - 550°C). The following objectives have been set.

1. Investigate the effect of no salt, $CaSO_4$, $Na_2SO_4$ and sea salt on the corrosion and crack initiation mechanisms of CMSX-4 in a 50 ppm $SO_2$ + Air environment under a constant load.
2. Based on the results from the phase 1 of the test, the effect of sea salt was worth studying further. Phase 2 consists in investigating the effect of NaCl (75% of sea salt) on the high temperature corrosion and crack initiation behaviour of CMSX-4.
    a. Carry out the tests in a 50 ppm $SO_2$ + Air and Air only to examine the effect of $SO_2$ on the corrosion and crack initiation mechanism.
    b. Examine how NaCl salt plays a role in the crack initiation mechanisms at 500°C (50 hr) and 450°C.

The thesis is divided into the following three sections:

1. Background and literature

The background section includes the remaining of chapter 1 and the literature review in chapter 2. The aim of the literature review is to provide a theoretical and technical background to the subject. Chapter 2 is divided into three sections. The first section introduces fundamental concepts of nickel-based superalloy design. The second section presents the high temperature corrosion mechanisms that operate in turbine blade components, focusing on moderate temperatures (approximately 550°C). The final section summarises mechanisms of embrittlement that have been reported in nickel-based superalloys and summarises other reported mechanisms of near surface weakening observed in other material systems and environments.

2. Experimental methodology, results, and discussion.

Chapters 3 and 4 define the bulk of the experimental work. Chapter 3 presents the C-ring test method that has been used to achieve a desired sustained stress level on test specimens. Also, the characterisation methods used throughout the thesis, which includes X-ray diffraction (XRD), scanning electron microscopy and transmission electron microscopy (SEM/TEM).

Chapter 4 examines the effect of no salt, $CaSO_4$, $Na_2SO_4$ and sea salt on the corrosion and crack initiation behaviour of CMSX-4 and a discussion of the stress assisted cracking behaviour. Based on the observed effects of sea salt, chapter 5 examines the effect of NaCl in an air and air – 50 ppm $SO_2$ environment. Tests at lower temperatures have also been examined. Based on the experimental findings, two postulated mechanisms are proposed.

3. Conclusions and further work.

The final part of the thesis includes chapters 6, 7 and 8. Chapter 6 provides a general discussion before drawing conclusions in chapter 7 and proposing future work in chapter 8.

## 1.3 Presentations and publications

Presentations of this work have been made in the following conferences.

- F. Duarte, oral presentation “Investigation into the effects of salt chemistry and $SO_2$ on the crack initiation of CMSX-4 in static loading conditions” in *TMS Superalloys 2020.*
- F. Duarte, oral presentation “Effect of NaCl and $SO_2$ on the stress corrosion cracking of CMSX-4 at 550°C” in *Microscopy of Oxidation 11.*

The following conference and journal papers have been published.

**Conference papers**

- F. Duarte Martinez, N. I. Morar, M. Kothari, G. Gibson, J. Leggett, J. C. Mason-Flucke, J. R. Nicholls, G. M. Castelluccio, and S. Gray “Investigation into the effects of salt chemistry and $SO_2$ on the crack initiation of CMSX-4 in static loading conditions” in *TMS Superalloys 2020. This conference paper contains parts of Chapter 5.*

**Journal papers**

- F. Duarte Martinez, A. Syed, K. Dawson, G. J. Tatlock, N.I. Morar, M. Kothari, C. Tang, J. Leggett, J.C. Mason-Flucke, G. Gibson J.R. Nicholls, S. Gray, G.M. Castelluccio *"Effect of NaCl and $SO_2$ on the stress corrosion cracking of CMSX-4 at 550°C" in the journal "Materials at High Temperatures" (under review).*

  *This journal paper contains part of Chapter 6.*
- K. Dawson, F. Duarte-Martinez, S. Gray, J. Nicholls, G. Gibson, J. Leggett and G. J. Tatlock *"Environmentally Assisted Cracking of a Single Crystal Nickel-Based Superalloy" in Materials at High Temperatures" (under review).*
- A. Syed, F. Duarte Martinez, T. Roberts, A. Encinas-Oropesa, N. Morar, M. Grohne, M. Frommherz, J.R. Nicholls, S. Gray, *"Performance Comparison Between Isothermal Hot Corrosion And In Situ Cyclic Hot Corrosion of Nickel-Based Superalloys" in Oxidation of Metals 96, 43-55 (2021)*
- Adnan. U. Syed, Manon Waeytens, Tracey Roberts, Fabian Duarte Martinez, Jonathan Leggett, Grant Gibson, Simon Gray and John. R. Nicholls, *"A microscopy study of nickel-based superalloys performance in Type I hot corrosion conditions"* in *Materials at High Temperatures (Under review)*

# 2 Literature review

## 2.1 Materials used in aeroengines

Aeroengines are typically manufactured with a range of materials in different sections of the engine and the material selection depends on their operating conditions. Due to weight considerations, titanium alloys are used for the compressor and fan sections [1]. However, they have a poor resistance to high temperature oxidation, so their application is limited to below 700°C [2]. Nickel-based superalloys alloys are the material of choice for turbine blades, as they have high creep resistance, thermal fatigue resistance and high temperature corrosion resistance.

Table 1 shows the main metallic systems used in different sections of a gas turbine.

*Table 1 - Summary of sections and materials used in a typical gas turbine*

| | **Inlet** | **Compressor** | **Combustion cans** | **Turbines** |
|---|---|---|---|---|
| **Requirements** | 1. Low density<br>2. Impact strength<br>3. Fracture and fatigue strength | 1. Resistance to thermal shock<br>2. Creep resistance | 1. Buckling resistance<br>2. Thermal fatigue resistance<br>3. Creep resistance<br>4. Oxidation resistance | 1. Creep resistance<br>2. Thermal fatigue resistance<br>3. Oxidation and corrosion resistance<br>4. Impact tolerance |
| **Materials** | 1. Aluminium alloys<br>2. Titanium alloys<br>3. Fibre reinforced composites | 1. Entry – Titanium alloys<br>2. Exit – Nickel alloys | 1. Nickel alloys | 1. Single crystal Nickel alloys<br>2. Advanced coating systems |

Single crystal nickel-based superalloys are used in turbine blades (hotter temperatures) due to their structural properties and improved creep resistance in the 650-1100°C range [3]. Key requirements in these hotter areas of the jet engine are high temperature strength, oxidation and creep resistance. In the past, conventionally cast superalloys were replaced by single crystal superalloys to resist higher mechanical and thermal loads as well as oxidation and corrosion environments. One of the superalloys commonly used in turbine blades for aero engines is CMSX-4.

The strengthening mechanisms in nickel-based superalloys can either be by solid solution strengthening, precipitation hardened and by oxide dispersion. The strengthening mechanism mainly depends on the alloying elements. Table 2 describes the role of different alloying elements in nickel base superalloys.

*Table 2 - Alloying elements in nickel based superalloys* [4]

| **Elements** | **Effect on microstructure** |
|---|---|
| Co, Cr, Fe, Mo, W, Ta, Re | Solid solution strengthening |
| C, Ti, W, Mo, Ta, Nb, Ha, Cr | Carbide former |
| Al, Ti | Gamma prime (γ') former |
| Nb, Ta | Gamma double prime (γ'') former |
| Al, Cr, Y, La, Ce | Increase oxidation resistance |
| La, Th | Increase hot corrosion resistance |
| Cr, Co, Si | Increase sulphidation resistance |
| B, Ta | Increase creep resistance |
| B | Improve rupture strength |
| B, C, Zr, Hf | Grain refiners |

Nickel based superalloys are composed of a γ phase, that represents the matrix, and also of ordered γ' (gamma prime) precipitates. The γ matrix has an FCC

disordered structure. The γ’ phase has an $L1_2$ crystal structure, and the composition is generally $Ni_3Al$, where nickel atoms tend to sit in the cube faces and aluminium atoms in the corners. Different alloying chemistries and heat treatments can vary the size of these γ’ precipitates and hence change the precipitation hardening response of the alloy when subjected to stress. The presence of γ’ precipitates provide a high number of obstacles to hamper dislocation movement at elevated temperatures, which provides high temperature creep resistance to the alloy. It is also considerably important that the matrix and precipitate have similar or identical lattice parameters as the optimum strength is achieved when the precipitate is coherent with the matrix phase. Figure 1 shows the cubic structure of γ’.

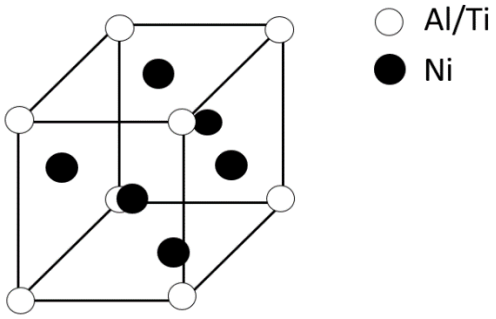


*Figure 1 - Cubic structure of γ’ phase*

Table 3 shows different phases formed in nickel base superalloys.

*Table 3 - Phases in nickel based superalloys* [4]

| Phase | Composition | Temperature range (°C) | Crystal structure | Lattice parameter |
|---|---|---|---|---|
| Gamma (γ) | - | - | FCC | a = 3.58 - 3.62 |
| Gamma prime (γ') | $Ni_3(Al, Ti)$ | > 600 | $L_{12}$ | a = 3.58 - 3.62 |
| Gamma double prime (γ'') | $Ni_3Nb$ | 600-920 | BCT | a = 3.62, c = 7.41 |
| $M_6C$ Carbide | $Fe_3Nb_3C$ | < 630 | FCC | a = 10.85 - 11.75 |
| $M_7C_3$ Carbide | $Cr_7C_3$ | 900 - 1050 | Hexagonal | a = 13.98, c = 4.52 |
| $M_{23}C_6$ Carbide | $Cr_{23}C_6$ | 650 - 950 | FCC | a = 10.56 - 10.65 |
| MC Carbide | TiC | 750 – 1040 | Cubic | a = 4.47 |
| Boride | $(Mo_3Fe)B_2$ | - | Tetragonal | - |
| $M_2SC$ Sulfocarbide | (Ti, Zr)SC | - | - | - |
| Laves | $(Nb,Ti)(Fe,Ni,Cr)_2$ | < 1150 | Hexagonal | a = 4.74, c = 7.72 |
| η phase | $Ni_3(Ti,Nb)$ | 650 - 1000 | HCP | a = 5.10, c = 8.31 |
| σ phase | CrFeMoN | 540 - 980 | Tetragonal | a = 8.80, c = 7.70 |
| δ phase | $Ni_3Nb$ | 750 - 1080 | Orthorhombic | a = 5.14, c = 4.25 |

One of the key advantages of nickel-based superalloys is that both the yield and tensile strength increases with increasing temperature up to a certain limit. For the case of CMSX-4 and CMSX-10, the yield strength increases with increasing temperature up until approximately 800°C [2]. Superalloys such as CMSX-4 have a high volume fraction of γ' precipitates (approximately 70%) so any decrease in yield strength in the gamma matrix caused by an increase in temperature can be compensated by an increase in yield strength of the γ' precipitate [5]. This increase in strength of the γ' precipitate with an increase in temperature has been investigated by Thorton et al. [6] and takes place due to thermally activated cross slip of dislocations from the {111} octahedral plane to the {100} cubic plane. This cross slip of dislocations occurs with increased ease as temperature increases.

In addition, strengthening in nickel base superalloys occurs due to coherency hardening and order hardening, which involves the presence of γ' precipitates [6]. Coherency hardening takes place due to the mismatch in lattice parameter between the γ phase and γ' precipitate [2]. Ordered hardening takes place due to the creation of antiphase boundaries (APB). Anti-phase boundaries are created when a dislocation passes through the ordered $L1_2$ precipitate, and the energy required to generate APB opposes the passage of dislocations. This barrier to the passage of dislocations is what ultimately leads to an increase in strength [2].

## 2.2 Heat treatment

The mechanical properties of the alloy are significantly impacted by the microstructure. One way to manipulate the microstructure is to control the composition and by the application of heat for a certain period of time. Two typical heat treatment techniques applied to superalloys are the solution heat treatment (annealing) and the aging heat treatment [2].

Solution heat treatment is done to reduce elemental segregation, which promotes gamma prime coarsening. The superalloy is held at temperatures between the solidus and the solvus for a certain period of time to achieve a homogenous solution of the phases [2]. In order to achieve the desired microstructure, the alloy is cooled rapidly to room temperature by water quenching or air cooling and may be followed by an aging treatment. The heat treatment for the CMSX-4 samples used in this study will be described in the methodology section.

## 2.3 Mechanisms of high temperature corrosion in gas turbine components

Oxidation, Type I and Type II hot corrosion are the main degradation mechanisms, currently identified, that operate in gas turbine blade components. Figure 2 highlights the temperature ranges where the identified degradation mechanisms are most prevalent in turbine blade components. This chart assumes sodium sulphate and associated eutectics are the predominant hot

corrosion initiator. In this section a description of the mechanisms of high temperature oxidation and hot corrosion will be given.

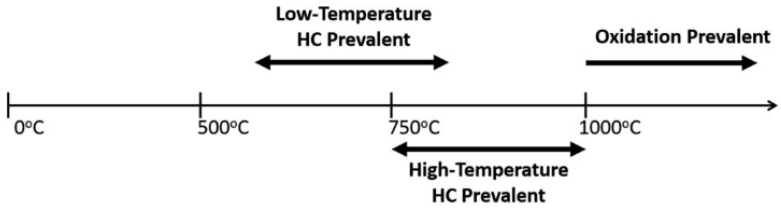


*Figure 2 – Temperature range of typical high temperature corrosion mechanisms in aero turbine blade* [7]

### 2.3.1 High temperature oxidation

Oxidation can be defined as the chemical reaction between a metal and oxygen and has a significant effect on the degradation of metals in high temperature environments, such as those experienced by gas turbines. From a thermodynamic point of view, metals are unstable in ambient gases and tend to react to form sulphides, nitrides, oxides and carbides.

Typically, oxidation mechanisms can start with the absorption of $O_2$ on the metal surface and subsequently the splitting of $O_2$ into oxygen atoms takes place. Ultimately, an oxide is formed by the reaction of oxygen and the metal. This chemical reaction can be expressed as follows [8]:

$$aM + \frac{b}{2}O_2 \rightarrow M_aO_b \qquad \text{Equation 1}$$

Where a and b are the reacting moles and $M_aO_b$ is the oxidation product. A chemical reaction will occur if the total free energy of the product is less than the total product of the reactants [8].

$$\Delta G = G_{products} - G_{reactants} < 0 \qquad \text{Equation 2}$$

In the oxidation of metals, the Gibbs free energy can be written as shown below [8].

$$\Delta G = \Delta G^0 + RTln\left[\frac{\alpha_{metal\ oxide}}{{\alpha_M}^a\ x\ {\alpha_{O_2}}^{b/2}}\right]$$ Equation 3

$\Delta G^0$ is the standard free energy, a and b are the reacting moles, R is the universal gas constant and α is the thermodynamic activity of the products, which is defined as [8]:

$$\alpha = \frac{p_i}{p_i^0}$$ Equation 4

, where $p_i$ is the partial pressure of the gas and $p_i^0$ is its partial pressure in standard state [8]. An oxide is more stable the more negative its standard free energy of formation ($\Delta G^0$). An Ellingham diagram (Figure 3) consisting of the standard free energy per mole of oxygen of a reaction as a function of temperature. They consist of lines of: $\Delta G^0 = \Delta H^0 - T\Delta S^0$ and can be used to determine the relative stability of an oxide [8].

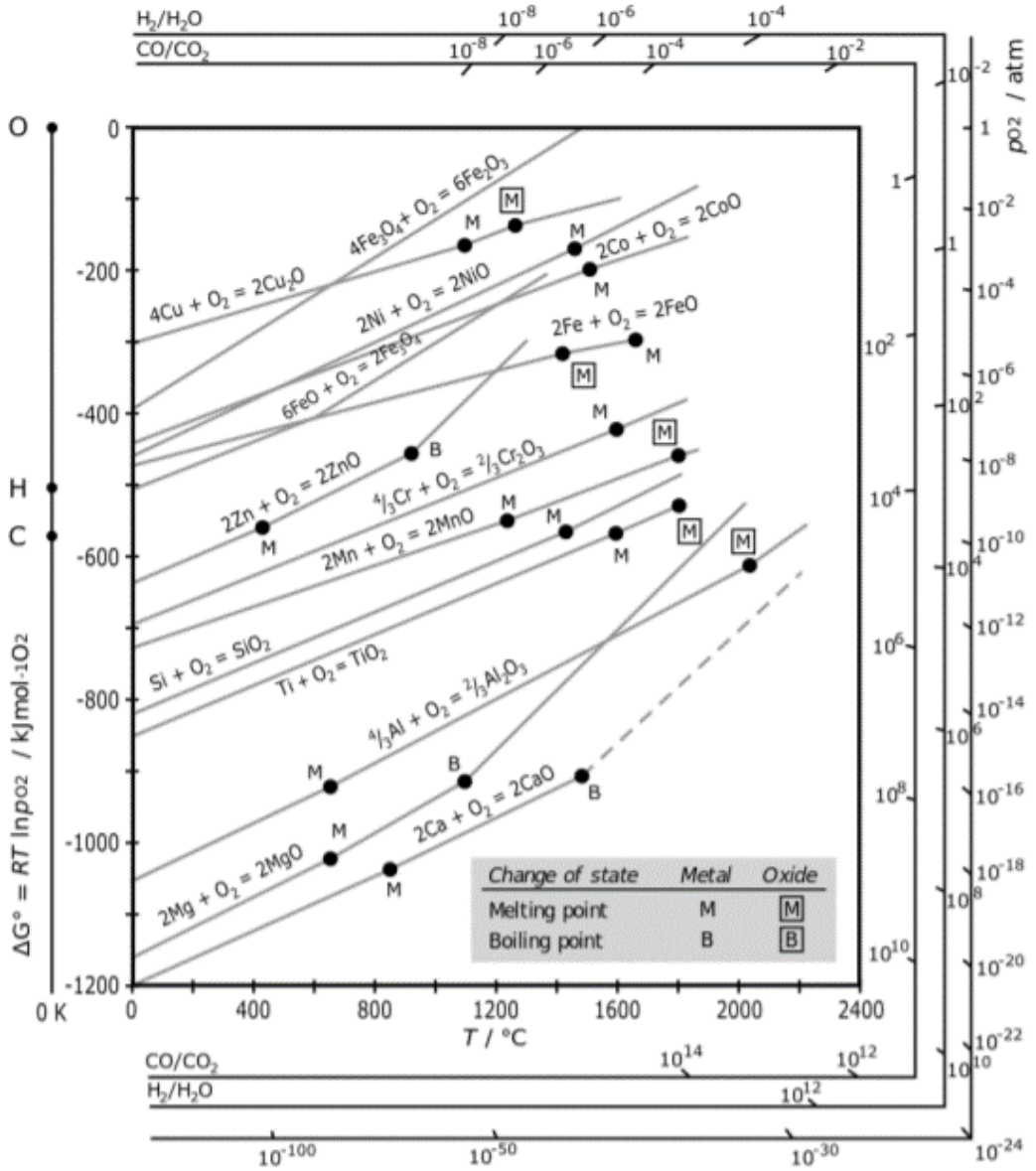


*Figure 3 - Ellingham diagram of selective oxides in high temperature corrosion applications* [9]

### 2.3.2 Physical mechanisms

The growth of continuous oxide scales typically occurs through solid-state diffusion of atoms, ions and/or electrons, which are dependent on the presence of defects in the oxide scale [10]. Defects in metals and oxides can be categorised as point defects (e.g. vacancies), bulk defects (i.e. precipitates and voids) and linear and planar defects (i.e. dislocations). Planar, linear and point defects can combine and lead to non-stoichiometric and stoichiometric compounds. $Al_2O_3$, for instance, is close to ideal stoichiometry as it exhibits a low defect content.

Therefore, the formation of $Al_2O_3$ generally results in a dense and continuous layer. In stoichiometric compounds, the defects maintain electroneutrality, which leads to Frenkel and Schottky defects. Schottky defects consist of an anionic and cationic vacancy, while Frenkel defects consist of an interstitial cation and a cationic vacancy. An illustration of Schottky and Frenkel defects in oxide scales in provided in Figure 4.

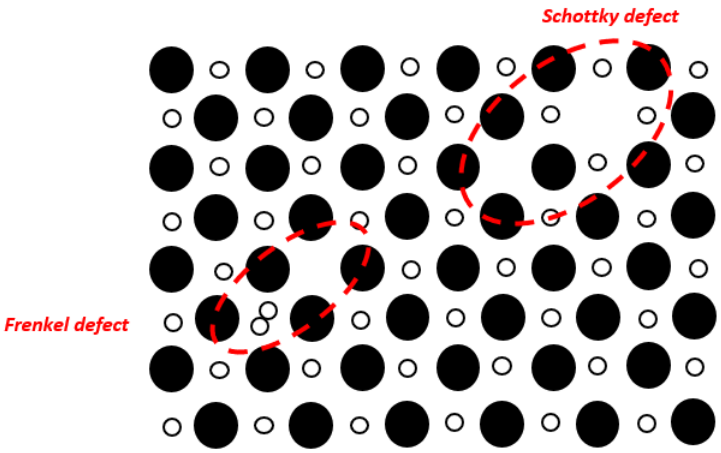


*Figure 4 – Illustration of Schottky and Frenkel defects in oxide scales* [11]

The mechanisms of diffusion can be categorised into lattice diffusion and short circuit diffusion. Lattice diffusion occurs due to the presence of point defects and normally leads to several types of diffusion mechanism. The interstitial mechanism occurs when an interstitial ion diffuses to a neighbouring interstitial site [11]. This mechanism may occur when the interstitial ion/atom is smaller in size than the ion/atom in the lattice sites. The vacancy mechanism occurs when an atom/ion migrates from a normal lattice site to a neighbouring and unoccupied lattice site. This mechanism results in a vacancy created where the ion/atom was located [11]. The intersticialcy mechanism involves the migration of an ion/atom to a normal lattice site and the ion/atom that was in that normal lattice site migrates to the neighbouring interstitial site.

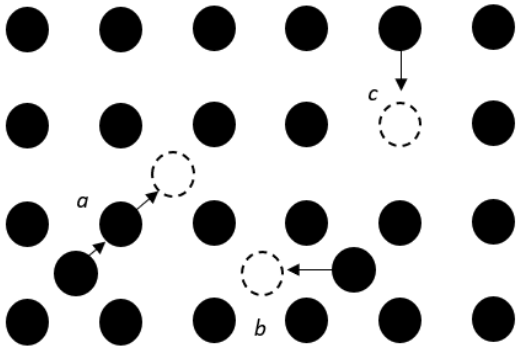


*Figure 5 – Interstitial and vacancy sites in oxide scales(a) intersticialcy diffusion, (b) interstitial diffusion, (c) vacancy diffusion* [11]

Short circuit diffusion takes place with two-dimensional defects, such as dislocations and grain boundaries. These defects are known to be fast diffusion paths through the oxide as their diffusion coefficient is higher than lattice diffusion. The activation energies for short circuit diffusion tend to be 0.5 – 0.7 times lower than those for lattice diffusion [12]; so, this type of diffusion mechanism typically occurs at low temperatures, below 80% of the alloy/metal's melting point [13]. As temperature increases, lattice diffusion becomes dominant and short circuit diffusion contributes less. As the temperature approaches the melting point of the alloy, short circuit diffusion becomes negligible.

Ultimately, the resistance of materials to environmental degradation at high temperatures increases due to the formation of a thermodynamically stable, adherent, continuous, and slow growing protective oxide. The reaction that leads to oxide formation can take place at the oxide/gas interface or at the metal/oxide interface.

Generally, metal alloys containing nickel, chromium, and aluminium form a range of oxides when exposed to high temperature oxidizing environments. These oxides include NiO, $Cr_2O_3$, $Al_2O_3$, $TiO_2$ and $Ta_2O_5$ [14]. In terms of thermodynamic stability, $Cr_2O_3$ and $Al_2O_3$ are the most stable phases among these oxides and, apart from the thermodynamic stability the formation of $Cr_2O_3$ and $Al_2O_3$ is highly dependent on the amount of chromium and aluminium within the alloy. The formation of $\alpha$-$Al_2O_3$ is known to be very protective due to its strong adherence to the base metal, its stoichiometry, and its slow growth rate. For illustration

purposes, Figure 6 shows the reaction rates of different oxides at specific temperatures [8].

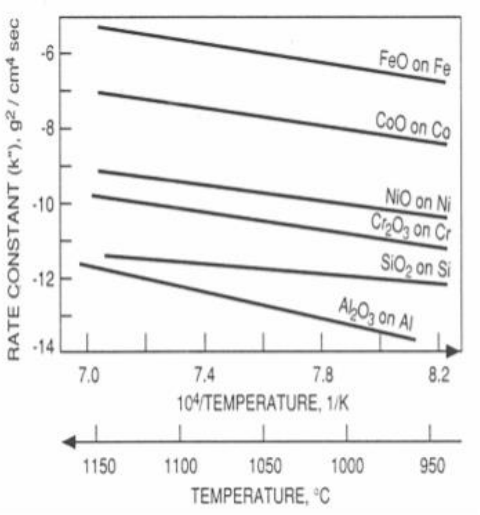


*Figure 6 - Reaction rate constants of selective oxide growth* [8]

Spinel type oxide layers of the form $Ni(Cr, Al)_2O_4$ are also protective oxide layers, which tend to form underneath the external oxide layer [8]. The formation of such spinel layers is also highly dependent on the composition of the alloy; however, the composition of the spinel layer may also change with the exposure duration at a specific temperature.

Chromium oxide tends to be protective in a variety of gas atmospheres but become non protective at high temperatures or low oxygen partial pressures. Above 1000°C, α-alumina scales tend to be more protective than chromium oxide. α-Alumina is also stable at significantly low partial pressures (as low as $10^{-37}$ bar) [15].

The mechanisms of diffusion during oxide formation can vary greatly depending on the operating conditions. For instance, Atkinson et al. [16] proposed that the diffusion of nickel in nickel oxide can occur through either bulk diffusion, grain boundary diffusion or dislocation diffusion mechanisms, with bulk diffusion the slowest and grain boundary diffusion the fastest. Kimm and Hobbs report that bulk diffusion can be the predominant mechanism in high temperature oxidation, whereas short circuit diffusion is predominant in low temperature oxidation [17]. In a similar investigation, Haugsrud [18] reported that pure nickel follows

Wagner's parabolic diffusion at temperatures below 600°C and at high temperatures above 1100°C. However, sub-parabolic oxidation was followed at temperatures between 600°C and 1100°C [18].

An illustration of the potential rates of mass gain during oxidation is shown in Figure 7.

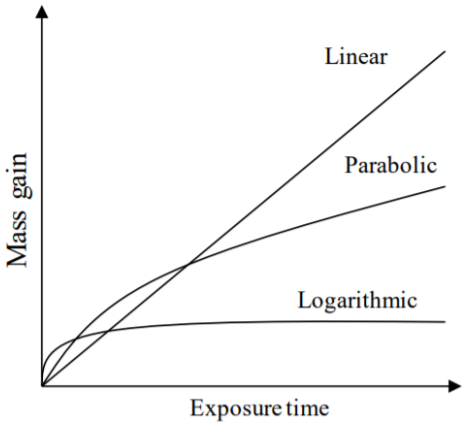


*Figure 7 - Mass gain against exposure time during oxidation for parabolic, logarithmic and linear growth* [8]

### 2.3.3 Oxidation mechanisms of CMSX-4 at moderate temperatures

Previous work was carried out to understand the oxidation mechanisms of CMSX-4 at 550°C [3], which can be summarised as follows. The oxidation mechanism follows a transient stage and a stable stage, as shown in Figure 8. The transient oxidation process starts by the outward diffusion of Ni cations, which forms bulges of NiO over the γ channels. Also, a thin aluminium rich oxide begins to form over the γ' particles. The outward diffusion of Ni forms a Ni depleted region adjacent to the surface of the alloy [3]. During this transient period, growth rates are still high as the porous morphology of NiO that forms at these temperatures provides an easy path of oxygen transport to the material substrate.

Oxygen atoms travels down the γ/γ' interface and comes into contact with both the γ and γ' phases. This oxygen diffusion path (ODP) through the γ/γ' interface could be explained by considering the stress state of the γ/γ' interface. Although the "disc" samples used for this test were not subjected to an external load, there are small differences in the lattice parameter between the γ and the γ', which becomes a source of additional strain in the microstructure. This source of

additional strain can be significantly increased when exposed to high temperatures, due to the difference in thermal expansion between the two phases. This results in increased dislocation densities at the γ/γ' interface, which lead to the formation of fast diffusion paths for oxygen ingress [19]. Oxygen travelling down the γ/γ' interface, as shown in the transient stage of Figure 8, comes into contact with both the γ and γ' phases. At the oxide/scale interface, the $pO_2$ and local concentration of elements seem to favour the formation of ternary spinel oxides, such as $NiWO_4$ [3]. As the oxide thickness increases, the $pO_2$ decreases further, so the activity of oxygen is insufficient to oxidise the γ phase (Ni, Co and Cr). Oxygen then readily reacts with Al from the γ' phase given that it is more thermodynamically favourable [3].

After the initial stages of oxidation, a thin and continuous alumina has started to grow internally below the spinel oxide and within the nickel depleted region. XRD results suggested the formation of a transient type of alumina (η-$Al_2O_3$) [3]. In addition, no $Cr_2O_3$ was detected [3].

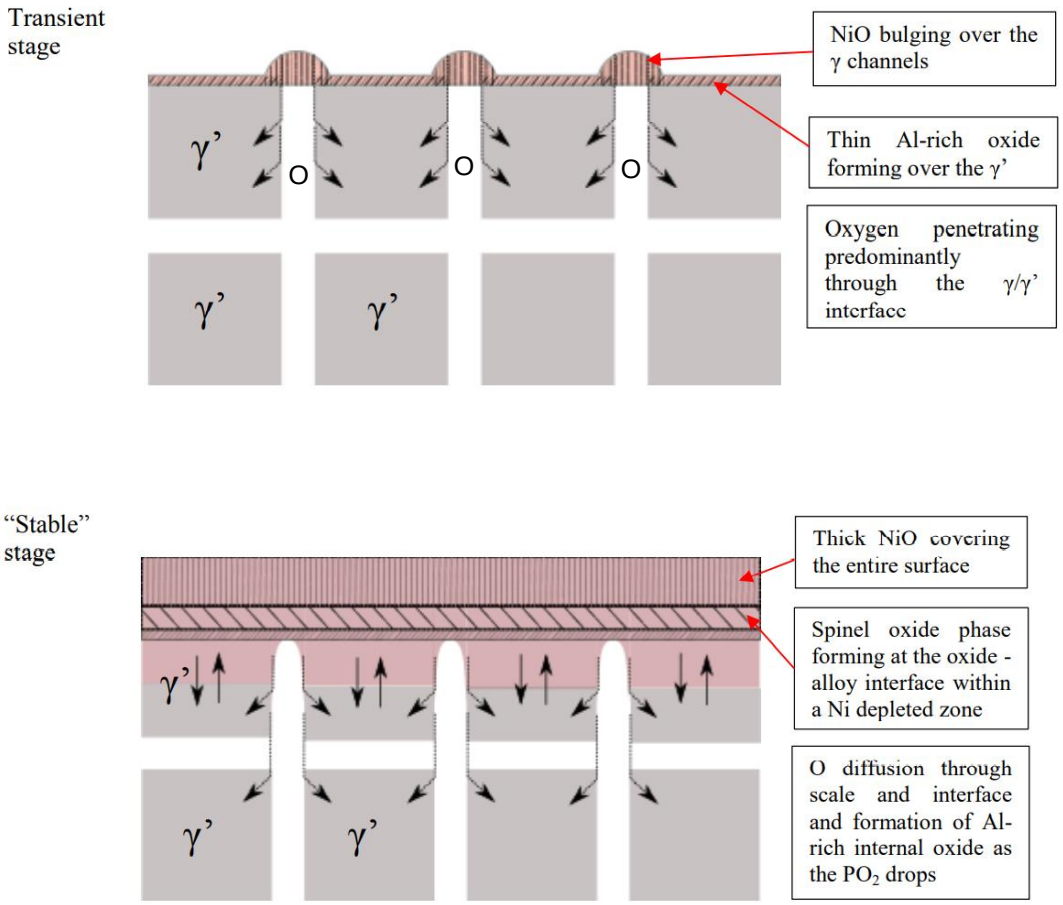


*Figure 8 – Transient and stable stages of oxidation of CMSX-4 at 550°C* [20]

## 2.4 Sulphidation and hot corrosion

### 2.4.1 Sulphidation

There is a significant interest in studying the behaviour of metals in sulphur containing environments, as it is a typical high temperature corrosion mechanism in a range of industrial processes. In many of these cases, the problems caused by sulphidation arise due to the natural occurrence of sulphur in fuels. Therefore, materials that come into contact with combustion atmospheres at high temperatures may suffer from severe corrosion as is the case in heat exchangers, processing plants in petroleum and chemical industries, superheaters and gas turbines [21].

For the case of aerospace engine components, the source of sulphur comes either from the fuel and/or the air intake. All petroleum or hydrocarbon-based

fuels contain small concentrations of sulphur. For instance, the specification for Jet A, A-1 (JP-8) fuel allows a maximum concentration of 0.3% by mass of sulphur so generally gas turbine engines are not immune from the effect of sulphur containing environments at high temperatures [22]. Sulphidation is typically reported in the shrouds, blade root and in some cases in the blade airfoil [22].

High temperature corrosion rates of metals in sulphur containing environments is several orders of magnitude higher than their corresponding oxidation rates (typically between $10^4$ and $10^6$ times higher than that corresponding to an oxidation conditions [23]). This is due to the large deviation from stoichiometry of sulphides, compared to oxides, and this, in turn, is caused by the lattice energy, which is such that point defects are easily created. For instance, Wooton and Birks investigated the corrosion rates of pure nickel in an Ar-$SO_2$ between 475°C and 900°C and found corrosion rates to be $10^7$ times higher than the oxidation rate of nickel in 0.1 atm $O_2$ [24]. This high corrosion rates in sulphur containing environments are due to the nature of the sulphide scale, which is highly porous, non-adherent and has greater non-stoichiometry (therefore, a higher defect concentration) than their corresponding oxides. On the other hand, refractory metals have sulphides with very low deviations from stoichiometry, and they show superior resistance to sulphide corrosion. For example, the sulphidation rates of niobium and molybdenum are comparable to their oxidation rates [23].

Matter transport through metal sulphides takes place mainly through point defects (i.e. volume diffusion), therefore transport properties through sulphide scales may be characterised by self and chemical diffusion coefficients [25]. Oxides tend to be more compact and have a stronger adherence to the substrate, therefore corrosion rate in air or oxygen tend to be significantly lower than that in sulphur containing environments [26]. Figure 9 shows the comparison of self-diffusion coefficients in sulphides and oxides, clearly indicating that the rate of cation self-diffusion in sulphides exceeds considerably that of the corresponding oxide.

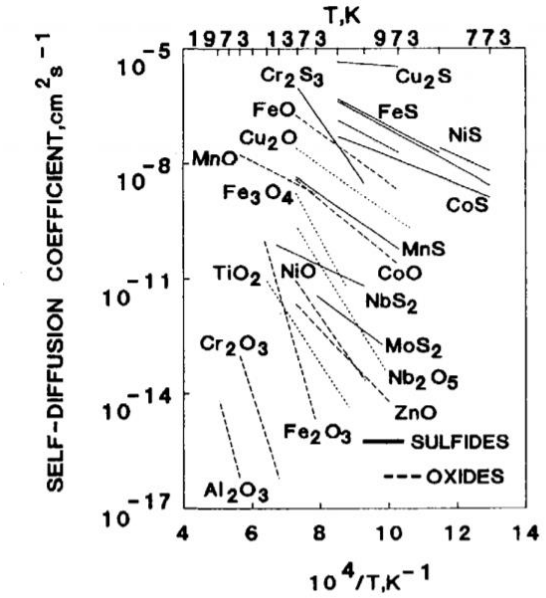


*Figure 9 - Self diffusion coefficients in some metal sulphides and oxides* [27]

Gas turbine components, such as turbine blades, may be susceptible to corrosion mechanisms such as sulphidation and two related types of high temperature corrosion, known as Type I and Type II hot corrosion. Temperature is one of the factors that has a crucial impact on the type of corrosion mechanism observed. As the temperature distribution across a turbine blade is non-uniform there are distinct types of corrosion mechanisms that can take place in different regions of the blade.

Jalowicka et al. [28] investigated the oxidation effects of CMSX-4 and CM247 at 1050°C in the presence of $SO_2$. CMSX-4 formed a dense and adherent alumina oxide, which provided a barrier against oxidation in the $SO_2$ containing environment. In contrast, the CM247 underwent significant degradation, potentially due to its microstructure. The dendritic regions in alloy CM247 contains high amounts of Cr and low amounts of Al, which promoted the formation of a chromia scale. Subsequently, internal Cr sulphide formed, which depleted the Cr content on the surface of the alloy leading to the formation of nickel rich oxides and Ni sulphides. Eutectic areas in alloy CM247, which feature a larger volume fraction of γ' are rich in Al and formed an alumina scale on the surface. Alumina scales are more "gas tight" in comparison with chromia scales, therefore they don't easily allow molecular transport of $SO_2$ molecules, or the diffusion of

sulphur, through the scale. As a result, these eutectic regions in CM247 were less affected by $SO_2$.

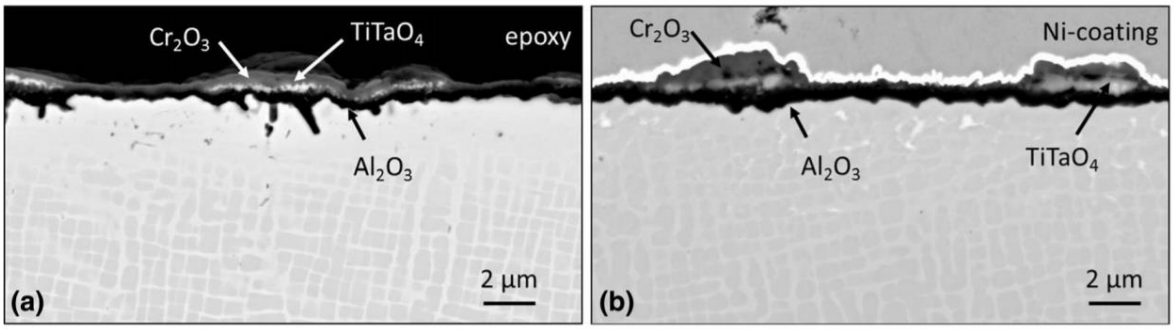


*Figure 10 - SEM back-scattered electron images of CMSX-4 in synthetic air + 2% vol. $SO_2$ at 1050°C after a) 1 hour, b) 20 hours* [28]

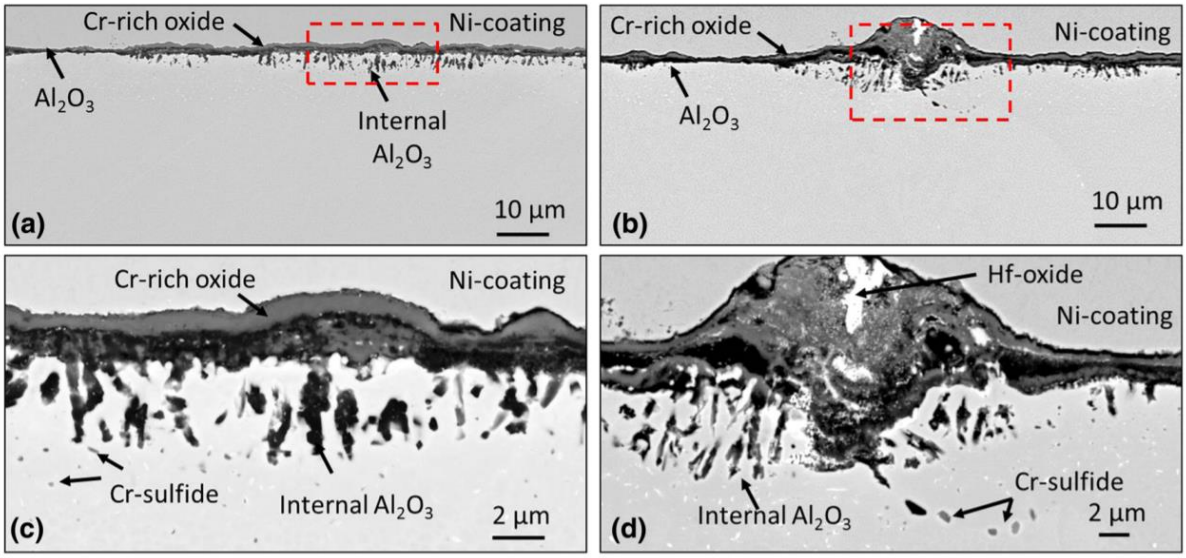


*Figure 11 - SEM backscattered electron images of CM247 after 1 hr isothermal oxidation in synthetic air + 2% SO2 at 1050°C* [28]

In certain cases, the sulphidation of Cr or Al can be significantly detrimental as it prevents the formation of protective oxides. For chromia forming alloys, the depletion of chromium results in a non-sustained growth of chromia scales and subsequently nickel will start to be oxidized. For alumina-forming alloys, the depletion of chromium results in a loss of the “gettering effect” and as a result the alumina formation can no longer be sustained [29].

### 2.4.2 Hot corrosion

This type of high temperature corrosion is common in the turbine section of gas turbine components. The mechanism of hot corrosion can take place as a result of the deposition of different deposits such as sodium sulphates, calcium, potassium, magnesium sulphates [30][31]. However, $Na_2SO_4$ tends to be the species most commonly deposited onto gas turbine components.

Hot corrosion can take place when the deposit is in the liquid state initially or is a solid deposit turns into liquid during the exposure due to reactions within the environment. Type I hot corrosion is normally observed between 825°C and 950°C, where the condensed phase is in the liquid state. $Na_2SO_4$ is normally formed due to the reaction of sodium chloride (mainly from sea salt that has been ingested with air) and compounds of sulphur, which are often found in many fuels [30]. The morphology for Type I hot corrosion is typically characterised by internal sulphidation and a depletion zone under the layer [32].

The sulphation of NaCl to form $Na_2SO_4$, which is required for the hot corrosion mechanism can be described according to the following reaction [33].

$$2\,NaCl + SO_2 + 1/2\,O_2 = Na_2SO_4 + Cl_2 \qquad \text{Equation 5}$$

Type II hot corrosion has been reported to occur below the melting point of $Na_2SO_4$ (884 °C), due to the formation of a liquid eutectic $Na_2SO_4$ – $NiSO_4$. This mechanism has been observed to take place in the temperature range 600°C - 750°C; Low temperature hot corrosion is typically associated with formation of a $NiSO_4$-$Na_2SO_4$ or a $CoSO_4$-$Na_2SO_4$ eutectic. Typically, the reaction of type II hot corrosion proceeds in two stages [34].

1. An initial stage in which $NiSO_4$-$Na_2SO_4$ is formed.
2. Propagation stage in which $SO_3$ migrates inwards and cobalt/nickel oxide migrates outwards through the eutectic melt that is formed.

The molten eutectic is typically formed when the mole fraction of $NiSO_4$ reaches 0.26 at 700°C and 0.12 at 800°C [34]. This means that an incubation period is required to form the critical concentration of $NiSO_4$ to yield the liquid sulfate

sulphate eutectic before any accelerated corrosion is observed. As temperature decreases the incubation period increases because higher mole fractions of $NiSO_4$ are required to form the eutectic melt. The partial pressure of $SO_3$ depends on the gas composition, temperature and thermodynamic equilibrium between $SO_2$ and $SO_3$.

Although Type I and Type II hot corrosion are key mechanisms for degrading gas turbine blades, there are many other possible reactions that may modify the hot corrosion reactions. Alloying additions can influence these reactions as degradable elemental species are susceptible to corrosion or oxidation at engine metal temperatures. Table 4 highlights some of these species and reactions as well as the temperature range in which they occur.

*Table 4 – Corrodent type and its resultant corrosion mechanisms* [33]

| **Corrodent** | **Mechanism** | **Temperature (°C)** |
|---|---|---|
| $O_2$ | Oxidation | > 1000 |
| $Na_2SO_4$ | Hot corrosion, sulfidation | 850 – 950 |
| $Na_2O$ | Basic fluxing | 850 – 950 |
| $SO_2$ | Sulfidation - Oxidation | 650 – 950 |
| $MoO_2$ ($WO_2$, $V_2O_3$) | Acidic fluxing | 850 - 950 |
| $CoSO_4$ – $Na_2SO_4$ (eutectic sulphates | Low temperature hot corrosion (LTHC) | 650 – 750 |
| NaCl | Chloride attack | 650 - 950 |

### 2.4.3 Mechanisms of hot corrosion

#### 2.4.3.1 Incubation stage

Hot corrosion has an initiation stage, in which the oxide scale is broken down and the alloy is degraded at a low rate, and a propagation stage, where the alloy is degraded at a significantly higher rate, due to the interaction of oxidation and sulphidation [35].

During the incubation stage, the alloy is exposed to normal oxidation conditions to the same extent as if the deposit was not present [36]. This stage can also be defined as the period in which the conditions for accelerated degradation are established, which includes the establishment of a liquid salt, for example, and the fluxing of the oxide scale. Two reported mechanisms of oxide scale fluxing are known as “basic” and “acidic” (the conditions required for each of these fluxing mechanisms will be described shortly). As an example, the equations below highlight basic and acidic fluxing reactions of NiO [12]. The incubation period depends significantly on the composition of the alloy and the environmental conditions. However, as a general guideline for CMSX-4 salted with a 4/1 $Na_2SO_4/KSO_4$ salt, exposed to 300 vpm $SO_2$ - air at 700 °C most of the sample had finished the incubation period after 500 hours as all locations showed non-zero good metal loss [37]. Good metal loss (GML) is defined as the amount of metal lost from the surface of the sample, including damage incurred beneath the surface in terms of distance [38]. Regions of the sample that are in incubation will give GML values of ≈ 0 µm [37].

Acidic dissolution: $NiO + SO_3 = Ni^{+2} + SO_4^{2-}$ Equation 6

$\mathrm{NiO} = Ni^{+2} + O^{2-}$ Equation 7

$NiO + Na_2SO_4 = Ni^{2+} + SO_4^{2-} + Na_2O$ Equation 8

Basic dissolution: $$2\mathrm{NiO} + \mathrm{Na_2O} + \frac{1}{2}\mathrm{O_2} = 2\mathrm{NaNiO_2}$$ Equation 9

$$NiO + Na_2O = 2Na^+ + NiO_2^{2-}$$ Equation 10

$$NiO + Na_2SO_4 = 2Na^+ + NiO_2^{2-} + SO_3$$ Equation 11

### 2.4.4 Propagation stage

The end of the initiation stage typically takes place when the salt penetrates through the protective oxide, as a result of salt fluxing, or potentially through mechanical defects, through cracks created by thermal cycling or through cracks due to the presence of chloride in the deposit [39].

There are two modes of propagation, which depend on the mechanism by which the molten deposit causes the continued fluxing of any oxide that is formed and the internal sulphidation of alloying elements, permitting the protectiveness of the reaction-product oxide to be damaged. These two propagation mechanisms are defined as modes involving various fluxing reactions, plus modes involving components in the deposit [35]. An important effect of the deposit is its ability to separate the metal alloy from the gas environment, hence creating an oxygen gradient. This results in a lower oxygen activity at the alloy's surface than if the deposit wasn't present. This condition can make the process of selective oxidation more difficult.

Three of the potential fluxing propagation mechanisms are comprehensively reviewed in the literature; these are known as "basic", "acidic" and "alloy induced" acidic fluxing. Using thermodynamic stability diagrams, the basicity or acidity of the fluxing mechanism can be assessed and therefore can infer the corrosion product morphologies observed during hot corrosion for a range of deposit compositions [40] [41]. For instance, the elements that make up the metal or the

protective scale can dissolve through either basic or acidic dissolution before precipitating out at the gas/salt interface.

Rapp et al. [42] conducted a series of experiments to determine the solubility of metal oxides as a function of melt basicity or oxygen activity in the $Na_2SO_4$ melt at 1200 K. Data from this work is illustrated in Figure 12. The left side leg of each of the oxides represents the basic dissolution of the oxide into the oxide melt interface, whereas the right-side leg of each oxide represents the acidic dissolution. Ultimately, each trough represents a minimum of solubility for that specific oxide.

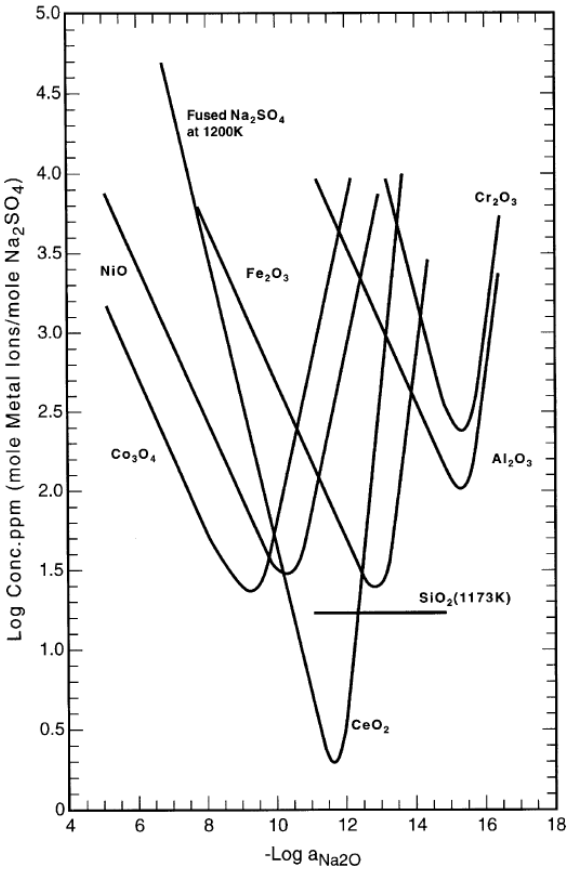


*Figure 12 - Solubility curves for various metal oxides in fused $Na_2SO_4$ at 1200 K* [42]

The equilibrium of the $Na_2SO_4$ salt in the melt can be expressed as an acid-base reaction as follows. $Na_2O$ (or $O^{2-}$) acts as base and $SO_3$ as an acid.

$$Na_2SO_4 \rightarrow Na_2O + SO_3 \qquad \text{Equation 12}$$

The basicity of the melt is then defined as -log ($a_{Na2O}$). The acid-base chemistry can then be expressed according to the equation below.

$$loga_{Na_2O} + loga_{SO_3} \rightarrow -16.7 \qquad \text{Equation 13}$$

Type II hot corrosion is another degradation mechanism commonly experienced by turbine blades at temperatures between 600°C and 750°C. In this degradation mechanism a $NiSO_4$-$Na_2SO_4$ eutectic phase is formed with a melting point of 671°C due to the reaction between the alloy and the deposit. For this reaction to take place, there is a minimum partial pressure of $SO_3$ that must be present. Figure 13 shows a stability diagram of NiO-$NiSO_4$-$Na_2SO_4$ highlighting the different stable phases that are present at different partial pressures of $SO_3$ and different temperatures.

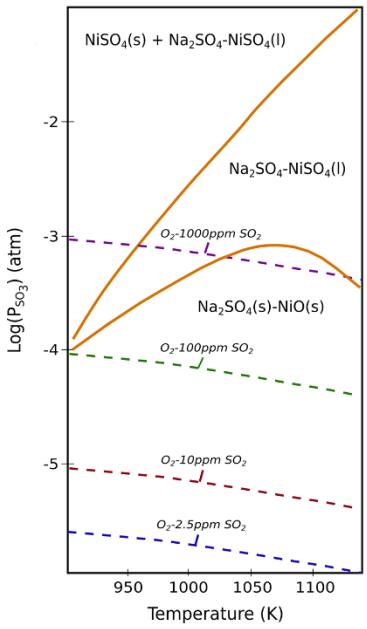


*Figure 13 - NiO-$NiSO_4$-$Na_2SO_4$ stability diagram* [43]

Possible mechanisms of sub melting point hot corrosion have also been discussed in [44][45] and the work highlights that hot corrosion degradation mechanisms can occur below the melting point of the deposits, so the mechanism differs from the typical Type II hot corrosion eutectic, where eutectic melts are formed. One of these mechanisms involves an accelerated outward diffusion due to the presence of a nanocrystalline phase and is reviewed below.

### 2.4.5 Solid state hot corrosion mechanism at temperature between 550 - 650°C

Recently a hot corrosion mechanism below between 550 - 650°C was reported to occur in nickel-based superalloys and pure nickel, where liquid formation is not predicted to occur [45]. A salt load of 2.5 mg/cm$^2$ was applied and samples were exposed to a 10 ppm $SO_2$ gaseous environment. For the case of pure Ni and after just a 5.5-hour exposure period at 650°C, the morphology of the corrosion product consisted of porous NiO at the deposit/gas interface with entrapped $Na_2SO_4$ and an internal mixed oxide/sulphide scale.

It was observed that filaments of NiO penetrated into the $Na_2SO_4$, and these filaments were enveloped by a nanocrystalline phase, as shown in Figure 14. From multiple EDS measurements, the atomic percent of this phase was (16 ± 3) Na, (18 ± 5) Ni, (7 ± 3) S, and (58 ± 5) O. Based on this atomic percent composition, an approximated stoichiometry of $Na_2Ni_2SO_5$ was predicted to form [45]. Selective area diffraction of this phase was not possible due to the rapid electron beam damage incurred by this phase. The $Na_2Ni_2SO_5$ phase was metastable, and its decomposition resulted in NiO and particles of $Na_2SO_4$. The nanocrystalline structure of $Na_2Ni_2SO_5$ enabled the rapid Ni transport required for the rapid attack, which resulted in accelerated corrosion rates [45].

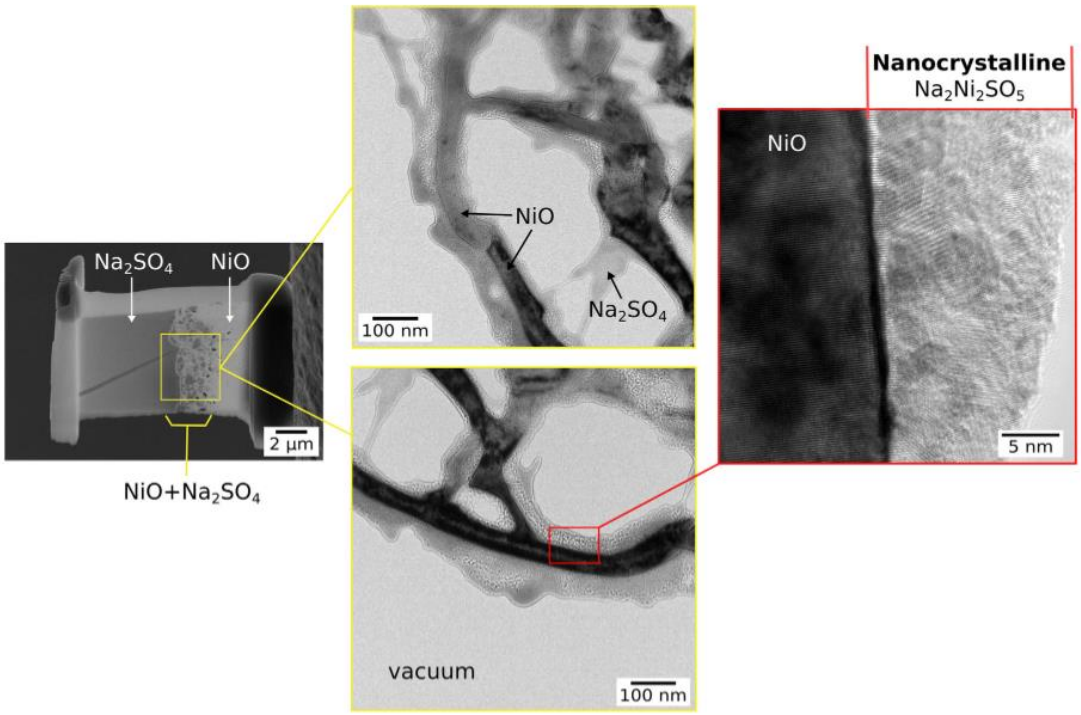


*Figure 14 - Image of TEM sample along with TEM images from the NiO + $Na_2SO_4$ region in the product formed on pure nickel. TEM transmission electron microscope* [45]

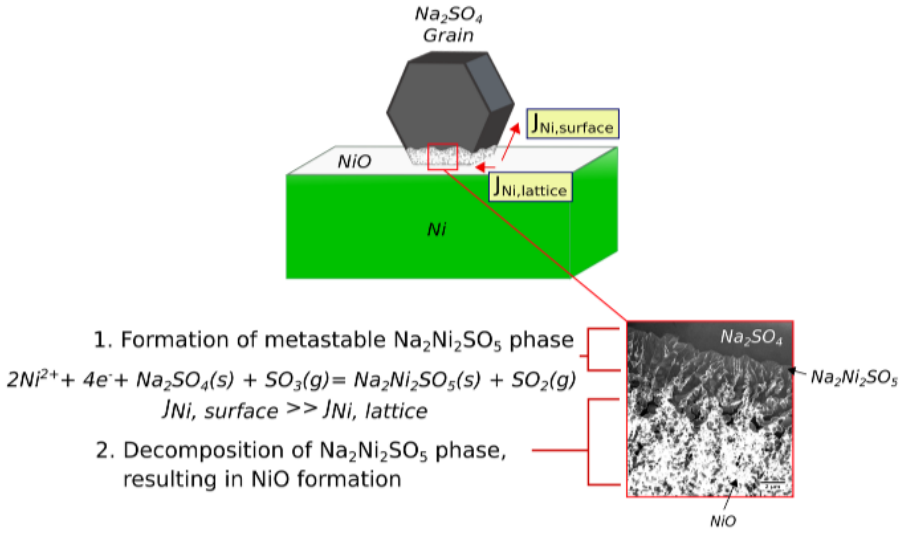


*Figure 15 – Postulated mechanism of solid state hot corrosion at 550°C* [45]

## 2.5 Effects of $Cl_2$ and HCl on the corrosion behaviour of pure nickel

In this section, the importance of chlorine containing species on the high temperature corrosion of gas turbine components will be discussed. Given that most of the work regarding the effect of chlorine in modifying high temperature corrosion has been undertaken in the field of fireside corrosion, knowledge from this field will be summarised and provide context to understanding the potential effect of chlorine-containing species in the aerospace field.

The main characteristic of high temperature corrosion induced by chlorine or hydrogen chloride is associated with the formation, vaporisation and reoxidation of metal chlorides, where chlorine is the “active oxidation agent” [46].

### 2.5.1 Effect of chlorine containing gases on high temperature corrosion

In oxidising/chlorinating atmospheres, metal oxides are present in the solid state but metal chlorides may be present in the gaseous state [47]. Some of the reasons that lead to high corrosion rates in chlorine containing environments is the low melting points and the high vapour pressures of metal chlorides compared to their oxides [48]. A metal chloride vapor pressure equal to or higher than $10^{-4}$ atm can lead to considerable metal consumption [49]. Table 5 lists the limiting vapor pressure for certain metal chlorides. From this table, one can infer that significant corrosion rates can be expected in metals containing nickel and chromium above 600°C.

*Table 5 - Physical properties of certain metal chlorides* [50]

| Chloride | $T_M$ in °C | $T_B$ in °C | $T_P$ in °C |
|---|---|---|---|
| $AlCl_3$ | 193 | 183 (Subl. *) | 76 |
| $CoCl_2$ | 740 | | 587 |
| $CrCl_2$ | 820 | | 741 |
| $CrCl_3$ | 1150 | | 611 |
| $FeCl_2$ | 676 | 1020 | 536 |
| $FeCl_3$ | 303 | 316 | 167 |
| $MoCl_4$ | 317 | 407 | |
| $MoCl_5$ | 194 | 268 | 58 |
| $NiCl_2$ | 1030 | | 607 |
| $SiCl_4$ | -70 | 58 | |
| $TiCl_4$ | -24 | 136 | -38 |

$T_M$ = Melting point, $T_B$ = Boiling point, $T_P$ = Temperature, where $p(MeCl_x) = 10^{-4}$ bar, (Subl*) = Sublimation point at 2,27 bar

Mechanisms of chlorine induced active oxidation can be described as follows [51] and an illustration of the mechanism is shown in Figure 16.

1. Formation of chlorine species ($Cl_2$, HCl and $Cl^-$) on the scale surface
2. Penetration of chlorine through the scale (perhaps through pores and cracks in the scale [52]) to the metal/scale interface. There is a lot controversy regarding the transport mechanism of chlorine through the scale. According to Nielsen et al. [49], active oxidation starts with almost no incubation time once chlorine is introduced into the system. The authors argue that neither grain boundary diffusion, solid state diffusion nor molecular diffusion through pores and cracks in the scale can account for the rapid corrosion rates observed in experimental results [49]. Potential mechanisms of chlorine diffusion through the scale will be discussed in more detail at the end of this section.

3. At the metal/scale interface, the partial pressure of oxygen is very low. This enables the formation of metal chlorides on the metal surface.
4. Metal chlorides have high vapour pressures. For instance, previous work done in steels report that $FeCl_2$(g) has a vapour pressure of 5 x $10^{-4}$ at 500°C, so it will evaporate steadily [53]. Therefore, metal chlorides diffuse outward through pores and cracks of the scale. This leads to loose, fragile and multi-layered oxides, which are unprotective [53].

$$M(s) + Cl_2(g) \rightarrow MCl_2(s) \qquad \text{Equation 14}$$

$$M(s) + 2HCl(g) \rightarrow MCl_2(g) + H_2 \qquad \text{Equation 15}$$

$$MCl_2(s) \rightarrow MCl_2(g) \qquad \text{Equation 16}$$

5. Reaction of metal chloride with oxygen to form an oxide and release chlorine gas. This can happen at the scale/gas interface or perhaps just under the deposit. This has shown to be extremely detrimental; for the case where $FeCl_2$ oxidises to form voluminous $Fe_2O_3$, which induces cracks in the scale and can further reduce the protectiveness of the scale [54]. The chlorine is then set free, which increases the chlorine partial pressure and leads to enhanced attack [55].

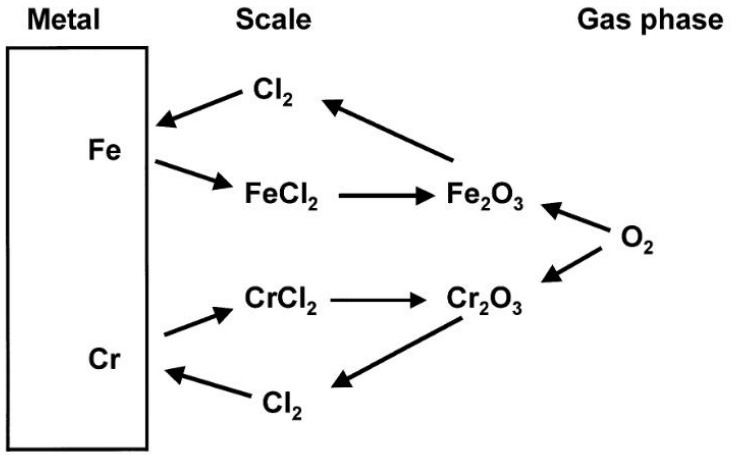


*Figure 16 - High temperature corrosion mechanism caused by $Cl_2$* [49]

### 2.5.2 The effect of alkali chlorides in a sulphur containing environment

Previous work have reported the accelerated corrosion rates observed due to the sulphation of alkali chlorides, such as KCl [56][49][57]. For instance, KCl can react with $SO_2$ or $SO_3$ from the environment to form $K_2SO_4$ and release either $Cl_2$ or HCl according to the expressions below:

$$2KCl(s) + SO_2(g) + \left({}^{1}/_{2}\right)O(g) + H_2O(g) \rightarrow K_2SO_4(s) + 2HCl(g) \quad \text{Equation 17}$$

$$2KCl(s) + SO_2(g) + O_2(g) \rightarrow K_2SO_4(s) + Cl_2(g) \quad \text{Equation 18}$$

The released HCl or $Cl_2$ can diffuse through pores and cracks in the scale to the alloy/scale interface and react with the alloy elements to form metal chlorides (i.e. $NiCl_2$ or $CrCl_2$). The metal chlorides that are formed typically have high vapour pressures (which will depend on temperature); therefore, they will diffuse out to regions with higher partial pressures of $O_2$. At this point, they will form metal oxides according to the following expression.

$$4MCl_2(g) + 3O_2(g) \rightarrow 2M_2O_3(s) + 4Cl_2(g) \quad \text{Equation 19}$$

$$4MCl_2(g) + 4H_2O(g) + O_2(g) \rightarrow 2M_2O_3(s) + 8HCl(g) \quad \text{Equation 20}$$

When alkali chlorides are exposed to gases containing $SO_2$ and $H_2O$, the sulphation of chlorides can occur as well as the release of HCl. The release of HCl can then lead to mechanisms of active oxidation. Different alkali chlorides exhibit different kinetics of HCl formation. For instance, Ozawa et al. [58] studied the reaction kinetics of NaCl, $CaCl_2$ and KCl and they report that under specific gas compositions $CaCl_2$ exhibits the highest rates of HCl evolution. Figure 17 highlights this difference in reaction kinetics.

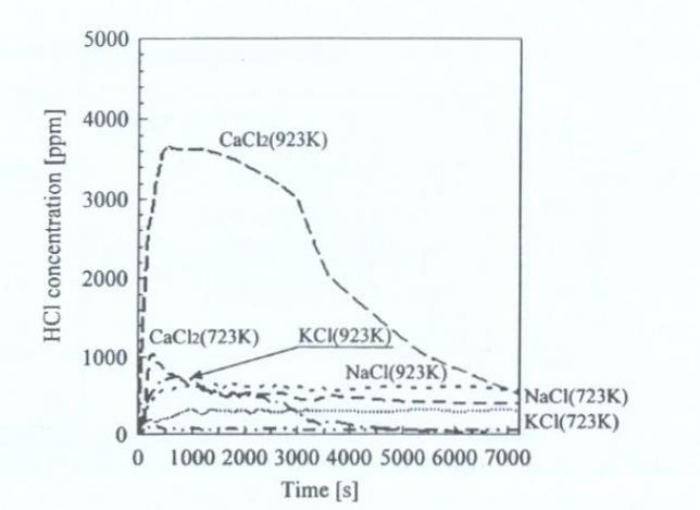


*Figure 17 - HCl concentration profile from $CaCl_2$, KCl and NaCl (gas flow rate: 2 x $10^{-4}$ $m^3$/min, SO2: 0.9 vol%, O2: 5 vol%, $H_2O$: 10%, $N_2$: balance at 723 K and 923 K)* [58]

Tang et al. [59] reports that the chlorine releasing effect of NaCl is smaller than $CaCl_2$ as the alkaline metals have a higher affinity for chlorine than the earth alkaline metals [59][60]. Furthermore, it has also been reported that sulphation of KCl takes place at a faster rate than NaCl [61].

According to Liu et al. [62] the sulphation kinetics of KCl depends on temperature, partial pressure of $O_2$ and partial pressure of $SO_2$. The partial pressure of $H_2O$ does not seem to affect the sulphation kinetics of KCl as long as the vol% of $H_2O$ is above 0%; however, having no water vapour at all seems to accelerate the reaction kinetics compared to having $H_2O$ in the system as observed in Figure 18. In Figure 18, $R_{s,d}$ is the sulfation degree and is calculated by (2S/2S + Cl molar ratio).

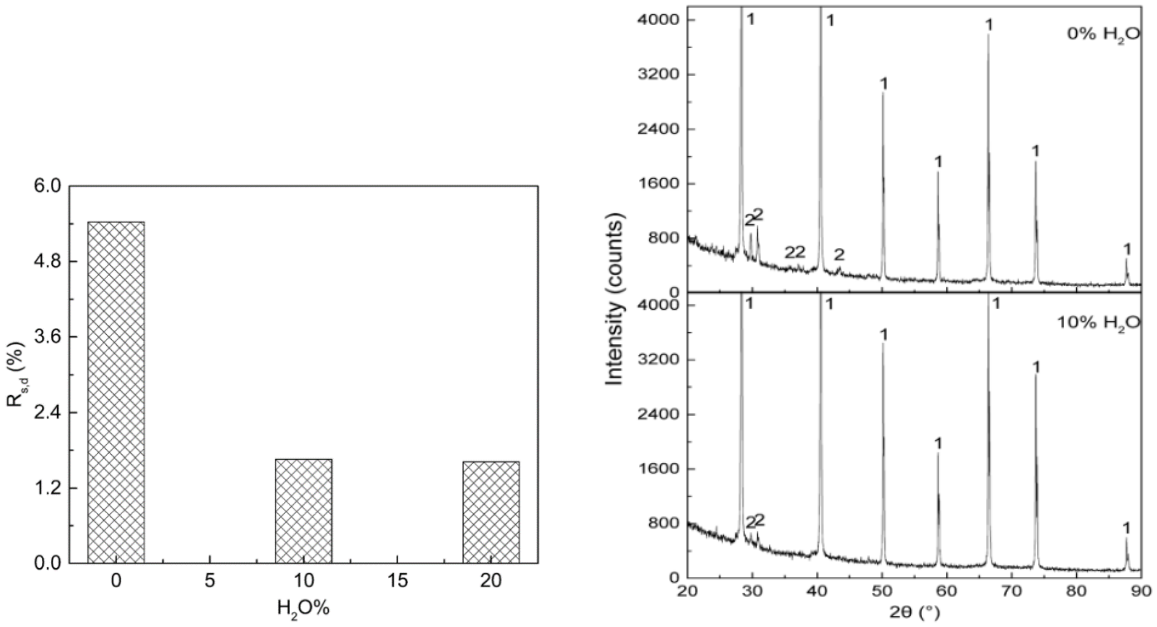


*Figure 18 – Influence of the concentration of water vapour on RSD, XRD pattern of (1) $K_2SO_4$, (2) KCl* [62]

Liu et al. [62] reports that the oxidation of $SO_2$ is the limiting step in the sulphation of KCl in the presence of $H_2O$. The reaction between $SO_3$ with nascent H radicals can limit the concentration of $SO_3$ in the gas phase as highlighted in the expression below, and this may suppress the sulphation of KCl. Therefore, the presence of H radicals can influence the sulfation efficiency of KCl.

$$SO_3 + H \leftrightarrow SO_2 + OH \qquad \text{Equation 21}$$

If the sulphation of NaCl is the cause for the chlorine-based degradation mechanism observed, a reduction in the kinetics of NaCl sulphation may lead to reduced corrosion degradation in a predefined amount of time.

Another cause for concern of having sulphur and chlorine containing gases is that the presence of chlorine will reduce the protective properties (increasing porosity, voids and cracks) of the scale, which then enables the ingress of sulphur containing species to form a mix of sulphides, chlorides and oxides in the scale or in the alloy/scale interface [63] [64].

In boiler environments, it has been reported that increased sulphur addition can reduce the corrosion due to the sulphation of alkali chlorides. This is the case because when KCl reacts with sulphur it forms $K_2SO_4$, and at the moderate

temperatures present in boiler environments $K_2SO_4$ doesn't cause the breakdown of the protective scale or form low melting point eutectics; therefore, accelerated corrosion rates are not observed. For instance, on A106 carbon steel, corrosion rate increased with the addition of up to 0.75% of sulphur and then drops dramatically with further addition of sulphur [65].

### 2.5.3 The effect of alkali chloride reactions with the metal scale

The detrimental effect of alkali chloride deposits well below the melting point of the salt can occur due to the reaction of these chlorides with the metal scale. For instance, Grabke [66] reports the reaction of NaCl with $Cr_2O_3$ that leads to an increase in corrosion rates. The breakdown of the $Cr_2O_3$ due to its reaction with NaCl is found in the expression below.

$$2NaCl(s,l) + 1/2\, Cr_2O_3(s) + 5/4\, O_2(g) \rightarrow Na_2CrO_4(s,l) + Cl_2(g) \quad \text{Equation 22}$$

This reaction can result in the release of $Cl_2$, which leads to the active oxidation of the metal. Chromate type oxides are considerably less protective than a chromia oxide. Hence, the materials are more susceptible and higher degradation rates are observed when chromate is formed. The reaction of NaCl with $Cr_2O_3$ is suggested to more likely occur when NaCl is present in the gas phase and not in the solid phase according to thermodynamic calculations [67].

One of the fields where chlorine induced high temperature corrosion is typically observed is in boilers where co-firing with coal and biofuel is used. In these environments, chlorine can be present as a chloride salt or in the gaseous atmosphere. Liu et al. [68] reported the effects of different alkali metal chlorides on the corrosion behaviour of different types of steel. In this work they mention the low melting point eutectics that can form when alkali chlorides react with other corrosion products within the scale, and highlight that eutectics with $FeCl_2$, $Na_2CrO_4$, $Na_2SO_4$ and other corrosion products can reduce the melting point of the salt mix significantly [68]. One example that is commonly observed is the eutectic NaCl-$Na_2CrO_4$ that has a melting point of 557°C.

It should also be highlighted that the reaction between KCl and $Cr_2O_3$ is more favoured than the reaction between KCl and $Al_2O_3$. Therefore, alumina forming alloys tend to be more resistant against chlorine-containing atmospheres, as the protective $Al_2O_3$ is not broken down in reactions with the salt [69] [70].

$K_2CO_3$ has also been reported to cause high rates of corrosion degradation as it can also react with the scale. Overall, alkali chlorides and alkali carbonates can more favourably react with the scale than alkali sulphates [71]. However, alkali chlorides tend to be most aggressive, more corrosive than alkali carbonates due to the presence of chlorine, which can trigger an active oxidation mechanism [72].

### 2.5.4 Chlorine transport mechanisms

One of the problems with the active oxidation (or chlorine cycle) described above is the current understanding of the inward transport mechanism of $Cl_2$ to the alloy/scale interface, where low oxygen activity is thought to prevail. It is postulated that the low oxygen activity at the alloy/scale interface is difficult to maintain, given that cracks and defects in the scale open to $Cl_2$ diffusion must also be open to $O_2$ diffusion. It is argued that the problems associated with the active oxidation mechanism can be resolved by applying an electrochemical reaction for the formation of metal chlorides. An electrochemical reaction as the one described below, where $Cl^-$ ions are formed, may explain certain chlorination processes observed, for instance, the presence of chlorine in the scale surface [73]. The mechanism by which $Cl^-$ ions are formed can be described by the following expression, occurring at the scale surface.

$$2KCl + {}^{5}/_{4}\, O_2 + {}^{1}/_{2}\, Cr_2O_3(s) + 2e^- \rightarrow K_2CrO_4(s) + 2Cl^- \qquad \text{Equation 23}$$

At the scale/alloy interface:

$$Fe(s) \rightarrow Fe^{2+}(oxide) + 2e^- \qquad \text{Equation 24}$$

$$Cr(s) \rightarrow Cr^{2+}(oxide) + 2e^- \qquad \text{Equation 25}$$

$$Al(s) \rightarrow Al^{3+}(oxide) + 3e^{-}$$ Equation 26

At these moderate temperatures, the ionic transport (of $Cl^-$) in this electrochemical mechanism is dominated by grain boundary transport. The transport rates of metal ions and chloride ions determines whether the metal chloride forms at the metal/scale interface or on the top of the scale.

Alternative transport mechanisms have been argued and include the substitution of chloride ions for oxygen ions in $Cr_2O_3$ scales [74][75]. In the case of HCl, these mechanisms suggest that the protons would annihilate the substitution mechanism and hence it explains why $Cl_2$ would cause enhanced oxidation rates whereas HCl does not. It would also explain the higher rate of transport in $Cr_2O_3$ scales than $Al_2O_3$ given that the substitution mechanism of chloride ions for oxide ions is easier in $Cr_2O_3$ given that it has a less closely packed structure.

A thick stoichiometric oxide should be impermeable to both chlorine and oxygen molecules. However, the oxide scale may not be impermeable to the ions. Chloride ions are larger than oxygen ions and are monovalent as opposed to divalent. This makes chloride ion's transport through the oxide lattice insignificant. However, due to their lower charge, the chloride ions that are adsorbed are mobile on the oxide surfaces. Given that oxide grain boundaries have similar properties to the oxide surface, they may offer a viable path to transport chloride ions from the surface of the oxide scale to the metal surface [76]. The chloride ions move along the grain boundaries of the oxides scale and when they encounter metal ions, metal chlorides are formed.

### 2.5.5 Influence of water vapour in chlorine containing environments

The degrading behaviour of $H_2O$ in high temperature chlorine-containing environments has been reported previously and vary greatly depending on the conditions. and the mechanisms involved can be summarised as follows [77].

1. Formation of volatile metal-oxyhydroxide species that lead to the formation of non-protective oxide scales.

2. Accelerated growth of the oxide scale due to a more rapid transport rate of $OH^-/H^+$ in the scale.
3. Assist in the internal oxidation of alloy elements and, consequently, accelerating the growth of specific metal oxides.
4. Competitive $O_2/H_2O$ adsorption at the scale/metal and scale/gas interface.

The influence of water vapour in chlorine containing environments varies significantly depending on the gas composition, alloy used and temperature. For instance, Wang and Shu [78] observed a significantly accelerated corrosion degradation of a Fe-Cr alloy with NaCl deposit corroded in air and water vapour compared to air only, as shown in Figure 19. They observed a denser and more uniform $Cr_2O_3$ scale when tests were carried out in air. However, introducing water vapour into the test led to a loss in the protectiveness of the oxide scale, as a loose and porous oxide was formed.

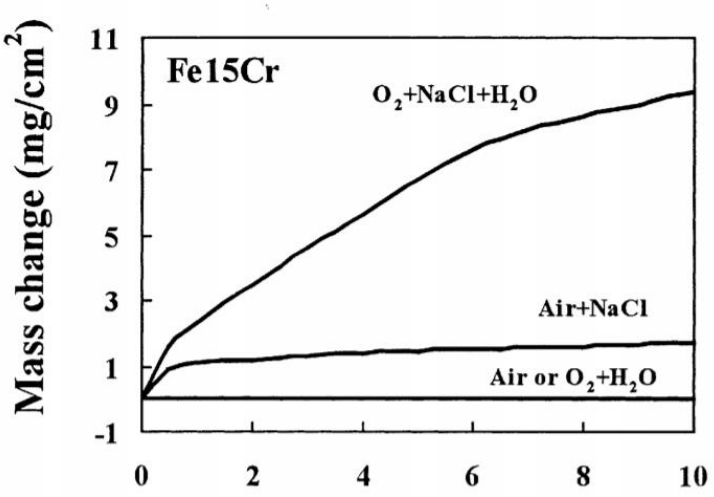


*Figure 19 - Corrosion kinetics of Fe-Cr alloy at 600°C*

On the other hand, Okoro et al. [77] reported that increasing the level of water vapour in a test atmosphere containing $SO_2$, $CO_2$ and $N_2$ and deposits of KCl decreased the measurable corrosion attack and decreased the rate of sulphation observed. They suggest that the addition of $H_2O$ caused competitive adsorption on active sites, that consequently lead to reduced corrosion rates.

### 2.5.6 Effect of chlorides on molten salt corrosion

The formation of a molten phase in high temperature environments typically leads to accelerated corrosion rates [49]. Metal chlorides generally have a lower melting point than oxides because $M\text{-}O^{2-}$ bonds are typically stronger than $M\text{-}Cl^{-}$ bonds [79]. For instance, sea salt contains a range of alkali chlorides, as shown in Table 6, and the interaction between them can lead to the formation of eutectic chloride compositions with very low melting points. Also, the reaction of alkali chlorides with metal chlorides can also lead to the formation of eutectic compositions with very low melting points. Table 7 shows the melting temperature of certain eutectic compositions.

*Table 6 - Wt % of sea salt constituents BS3900/F4 (1968)*

| Constituent | Wt% |
|---|---|
| NaCl | 76.6 |
| $NaHCO_3$ | 0.58 |
| KCl | 2.13 |
| NaBr | 0.82 |
| $MgCl_2$ | 7.01 |
| $MgSO_4$ | 9.65 |
| $CaCl_2$ | 3.21 |

*Table 7 - Chloride compositions with low melting points* [49]

| Salt mixture | Melting temperature (°C) |
|---|---|
| $MgCl_2$ - NaCl | 470 |
| $CaCl_2$ - NaCl | 500 |
| $CaCl_2$ - KCl | 590, 650 |
| KCl – $MgCl_2$ | 460, 450 |
| KCl – $MgCl_2$ – $CaCl_2$ | 620 |
| NaCl – $MgCl_2$ - $CaCl_2$ | 460 |
| NaCl – KCl – $CaCl_2$ | 500 |
| NaCl – $NiCl_2$ | 570 |
| KCl-$NiCl_2$ | 508 – 653 [80] |
| KCl – $CrCl_2$ | 462 – 475 [80] |
| NaCl-$Na_2CrO_4$ | 577ºC [81] |

Other molten compounds can be formed as well. For instance, NaCl may react with chromium or $Cr_2O_3$, to form $Na_2CrO_4$. $Na_2CrO_4$ can then react with excess NaCl to form a low melting eutectic NaCl-$Na_2CrO_4$ (577ºC), which leads to a molten salt dominated high temperature corrosion mechanism [81].

### 2.5.7 Hot salt stress corrosion cracking

Hot salt stress corrosion cracking is a typical failure mechanism experienced in Ti-alloys in aerospace and chemical industries. Hot salt stress corrosion cracking occurs when these alloys are exposed to halides in the temperature range 200 - 500°C. It is believed that the electrochemical reaction between titanium and salt leads to production of nascent hydrogen, which is responsible for the failure of

the alloy. Typical failure mechanisms due to hydrogen are hydrogen induced decohesion, hydrogen enhanced localised plasticity, brittle hydride formation and adsorption induced dislocation emission (recently reported) [82].

Chevrot [83] performed work on Ti-alloys, particularly IMI84, looking at the pressure effects on the HSSCC mechanism. The mechanism described by Chevrot starts with the reaction of $TiO_2$ with the salt and humidity in the atmosphere to form $Na_2TiO_3$ and HCl. The $H_2O$ in the reactions below can be present in the form of fluid inclusions in the salt or in the form of adsorbed moisture. HCl diffuses through microchannels and imperfections in the oxide scale and readily react with Ti, Al and other alloying elements at the alloy/scale interface.

$$TiO_2 + 2NaCl + H_2O \rightarrow Na_2TiO_3 + 2HCl \qquad \text{Equation 27}$$

$$Ti + 4HCl \rightarrow TiCl_4 + 4H \qquad \text{Equation 28}$$

$$Al + 3HCl \rightarrow AlCl_3 + 3H \qquad \text{Equation 29}$$

These reactions would inject nascent hydrogen into the material [83]. The volatile metal chlorides diffuse towards the scale/salt interface under a concentration gradient. Near the surface they are hydrolysed and deposited as solid oxides according to the following reactions [83].

$$TiCl_4 + 2H_2O \rightarrow TiO_2 + 4HCl \qquad \text{Equation 30}$$

$$2AlCl_3 + 3H_2O \rightarrow Al_2O_3 + 6HCl \qquad \text{Equation 31}$$

Since the oxygen activity is significantly reduced below the salt bead, the activity of $H_2O$ is likely to increase, therefore leading to the reactions of metal chlorides with $H_2O$ to release HCl. This explains why water vapour is required for this hot salt stress corrosion cracking mechanism. These reactions again form HCl, which

generate a self-sustaining cycle that further injects hydrogen into the material. Hydrogen diffuses to regions of high triaxial stress and when it exceeds the hydrogen solubility limit of the alloy, a crack is initiated. This mode of cracking was observed up to temperatures of 507°C.

This mode of failure is mainly observed in lab experiments but not in aircraft components, although they are exposed to halide containing environments. One reason for this is that the airflow in flight might remove corrosive products. The other reason is that these alloys are exposed to high pressures, and according to Chevrot [83], the effect of increasing the pressure on the hot salt stress corrosion can supress the hot salt stress corrosion cracking mechanism. It was found that increasing the partial pressure of oxygen results in the oxygen activity increasing below the salt beads. Therefore, Equation 32 and Equation 33 have to be considered. These reactions are competing with the pyrohydrolysis reactions described above and are producing chlorine gas instead of hydrochloric acid. So, at high pressures HCl is not produced, which is the main hydrogen carrier and, therefore, hydrogen is not injected into the material.

$$TiCl_4 + O_2 \rightarrow TiO_2 + Cl_2 \qquad \text{Equation 32}$$

$$2AlCl_3 + \frac{3}{2}O_2 \rightarrow Al_2O_3 + 3Cl_2 \qquad \text{Equation 33}$$

Boyd and Fink in 1969 mentioned there was a possibility that for HSSCC to occur quickly, a critical moisture level must be exceeded. Several investigators tried to prove this concept by testing in so called “dry” and “wet” conditions. However, it became obvious that only minute amounts of moisture were enough to cause HSSCC, rendering the task significantly difficult.

To further study the effect of “dry” and “wet” conditions, Hatch et al. [84] claimed that no cracks were observed in Ti – 5Al – 2.5 Sn at 427°C when the specimen and the salt were baked out before testing and kept in an anhydrous form during the exposure under stress. No cracks were observed in two hours of exposure, but it is possible that cracking was only delayed and not completely stopped.

Ondrejcin et al. [85] used similar conditions but at 347°C and with alloy Ti – 8Al – 1 Mo – 1V and no cracks were observed after 7 days of exposure in “dry conditions”, where the moist system showed cracking in ninety minutes.

Ultimately, there are various forms in which water can be formed in the process. Water can be present in vapor, occluded in the oxide scale or as crystallisation water within the salt. Lapasset [86] tried to isolate the effects of crystallisation water in the salt and atmospheric moisture on the HSSCC of Ti alloys. Firstly, he used infrared (IR) spectroscopy to measure the average concentration of water retained in sodium chloride salt and measured an average amount of 40 mg/cm$^3$. He also eliminated this crystallisation water to measure the influence of atmospheric moisture on the HSSCC and the conclusions were that atmospheric water plays a minor role in the HSSCC of Ti alloys compared to crystallisation water, particularly during the crack initiation stage in Ti alloys. So, it seems that the amount of moisture required for HSSCC is so low that crystallisation water occluded in the salt is enough to induce crack initiation in Ti alloys.

Although the maximum temperature tested in Chevrot’s work was 500°C, he argued that the extent of damage due to HSSCC may increase at higher temperatures. This may be the case because at higher temperatures, the kinetics of HCl formation, HCl diffusion through the scale and the kinetics of metal chloride formation increase and, consequently, the rate at which H is injected into the alloy will also increase [83].

Logan’s stress sorption model [87] suggests that reactions between the salt, oxide scale and alloy leads to the production of hydrogen, oxygen, and chloride ions. The model suggests that chloride ions diffuse down a stress and oxygen gradient. The subsequent reaction of chloride ions with alloying elements destroys the atomic bonds in the alloy and leads to stress corrosion cracks.

## 2.6 Effects of stress on high temperature corrosion and reported mechanisms of environmentally assisted crack initiation

In this section, a summary of reported mechanisms of environmentally assisted crack initiation will be provided. The first part will focus on reported mechanisms of crack initiation in high temperature environments (environments containing oxygen and sulphur). The last parts will provide a summary of the mechanisms reported in aqueous environments.

## 2.7 Stress assisted oxidation

The rate of transport of oxygen decreases in the following order fissures/voids>grain boundaries>dislocation pipes>lattice [88][89]. Stress may also lead to cracks and detachment of the oxide scale with increased oxidation rates in cracked areas [90], and detachment typically occurs at higher stresses where the stress can't be relieved by creep processes and hence through scale cracking does not occur. Stresses may also affect the segregation of impurities during oxidation [91].

Jiang [92] suggests that the presence of stress does not change the chemical composition of the oxidising products but typically leads to thicker oxide scales than specimens with no stress applied. It is suggested that the thicker oxide scales produced due to the applied stress is due to the accelerated diffusion of alloy elements given the presence of high-density dislocations and vacancies in the presence of an accumulated strain. On the other hand, Barnard et al. [93] studied the oxidation behaviour of Haynes 75 and Haynes 230 in air at 800°C for 1000 hours and they observed thinner oxide scales were observed. They attributed the thinner oxide scales to the faster formation of a protective $Cr_2O_3$, as the defects produced due to the external stress facilitates the diffusion of chromium and reduces the less protective transient oxidation period. Overall, it seems that stress can increase oxidation rates or reduce oxidation rates and which one of these occurs highly depends on the test conditions (i.e. alloy system, temperature of the test) [93].

Calvarin-Amiri et al. [94] investigated the effect of mechanical loads on the oxidation behaviour of Ni-10Cr foils at different temperatures. Their results suggest that the effect of stress have significant implications on the depth of internal oxidation in the alloy in a range of temperatures and several mechanisms regarding the formation of fast diffusion and short circuit paths are proposed. It also suggested that mechanical loads did not affect the nature of the oxide layers, but it led to an accelerated growth of some oxide layers. The presence of a mechanical load also seems to promote anionic diffusion, increase the porosity of the NiO layer, and may induce the formation of cracks. As a result of porosity, and microcracks fast diffusion paths are formed, which leads to accelerated rates of corrosion [94].

### 2.7.1 Stress assisted grain boundary oxidation (SAGBO)

SAGBO and dynamic embrittlement are two important mechanisms where high temperature oxidation plays a role in the crack propagation of high temperature materials, such as nickel-based superalloys [95]. As mentioned by Krupp et al. [96], dynamic embrittlement involves the penetration of embrittling elements (i.e. oxygen atoms) along grain boundaries, which leads to the decohesion of the grains. The role of stress in dynamic embrittlement is to provide the driving force for the diffusion of embrittling elements into the material. Stress assisted grain boundary oxidation refers to the enhanced oxidation attack in the grain boundaries of a material. Due to the brittle nature and low fracture toughness of the oxides formed, enhanced crack propagation rates are encountered. Evidence of SAGBO can be observed by the presence of layered structure of the oxides along or across the grain boundaries [97]. For instance, in RR1000 and U720Li the layered oxide across grain boundaries consist of an external Co/Ni oxide followed by an intermediate Cr oxide layer and an inner Ti/Al layer at the oxide/alloy interface [97]. This reduces the partial pressure of oxygen in the alloy/oxide interface. At this low partial pressure of oxygen, only alloy elements such as Cr, Ti and Al can form stable oxides. They do so in this same sequence measured inwards from the outer oxide layer, which is also the sequence of increasing thermodynamic stability [98]. SAGBO typically involves a transition in

crack path from transgranular crack propagation to intergranular crack propagation (promoting crack growth along grain boundaries).

Apart from SAGBO, Andrieu et al. [99] proposed mechanism that involves the formation of nickel oxide at the fracture surface. This formation of nickel oxide leads to the injection of vacancies and the accumulation of vacancies, which promotes grain boundary fracture.

### 2.7.2 Dynamic embrittlement

Mechanisms of dynamic embrittlement occur when elemental oxygen diffuses into the bulk metal, causing a reduction in cohesion, which leads to enhanced crack growth. This mechanism has been reported with the regards to intergranular fracture, where elemental oxygen reduces the cohesion in grain boundaries. The criterion for rupture in grain boundaries can be expressed as follows [100]:

$$\sigma_{loc} > \sigma_{GB} \qquad \text{Equation 34}$$

Where, $\sigma_{loc}$ is the local stress acting on the grain boundary and $\sigma_{GB}$ is the strength of the grain boundary. As the concentration of the embrittling species in the grain boundary increases, the grain boundary strength ($\sigma_{GB}$) decreases. The concentration of embrittling species depends on the chemical potential of the species, which can be expressed as follows [100].

$$\mu = \mu^0 + KTln(\gamma c) - \sigma_{loc}\Omega \qquad \text{Equation 35}$$

Where Ω is the atomic volume of the embrittling species, $\gamma$ its chemical activity coefficient, c its concentration and $\sigma_{loc}$ is the local stress acting at 90° to the path of diffusion. Ultimately, the driving force of diffusion is highly linked to the chemical potential gradient. As a result, an increase in stress can lead to a decrease in $\sigma_{GB}$ and an increase in $\sigma_{loc}$ [100].

### 2.7.3 Type II hot stress corrosion cracking in single crystal nickel-based superalloys

Brooking et al. [101] performed research on stress corrosion cracking of C-ring specimens and found that type II hot stress corrosion cracking in CMSX-4 can occur at temperatures as low as 550 °C. Tests were taken with 80/20 mol % $Na_2SO_4/KSO_4$ salt in air – 300 ppm $SO_2$ atmosphere at 550°C and a salt flux of 5 µg/cm$^2$/hr deposited every 100 hours. Cracks were observed in the tensile stressed region of the sample and an electrochemical stress corrosion mechanism was proposed, where the local strain conditions of the phases affect their anodic potential to a different extent.

The proposed mechanism was evidenced by the finding of Na in the crack, as highlighted in the EDX map in Figure 20, which supports the formation of a liquid melt, possibly containing $Na_2SO_4$. This is because, in order for Na to migrate from the specimen surface to the crack tip at the test temperature at 550°C, it is likely to have been in liquid solution.

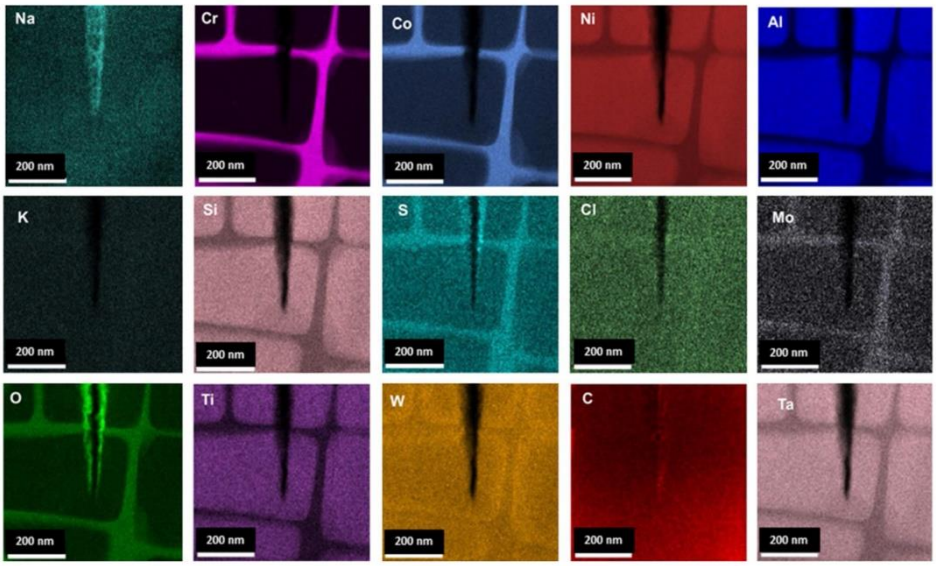


*Figure 20 - STEM EDX mapping showing elemental segregation between the bulk γ'/γ and the crack tip post-exposure* [101].

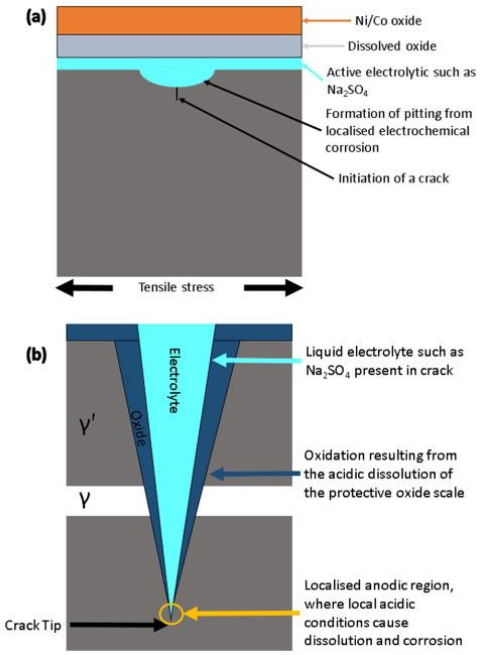


*Figure 21 - Proposed mechanism of electrochemical corrosion generating LTHC stress corrosion cracking (a) Stage 1 where LTHC initiates and small pits start to form (b) Stage 2 where a crack has propagated, and electrochemical corrosion is established at the crack tip* [101]

A key observation in this type II hot stress corrosion cracking mechanism is that cracks tend to split the γ' precipitates, propagating along [100] perpendicular to the surface of the specimen whereas with no corrosion, cracks in uniaxial state propagate along slip bands of the [111] family [102].

## 2.8 Stress corrosion cracking

Some of the reported mechanisms leading to enhanced crack growth in stress corrosion cracking and corrosion fatigue are anodic dissolution (stress assisted dissolution), film rupture, hydrogen enhanced assisted cracking and adsorption induced dislocation emission [103] [104].

Other stress corrosion cracking mechanisms are described in Gibbs [105]. Some of these mechanisms are the slip-dissolution model, corrosion-deformation interaction, internal oxidation and fracture and the vacancy-creep model. Some of the mechanisms relating anodic dissolution and crack growth have been given by Hai sheng et al. [106]. Also, Yahalom et al. [107] describe three SCC

mechanisms known as stress-sorption mechanism, film rupture-metal dissolution mechanism and hydrogen embrittlement mechanism.

It is also important to consider that environments that don't necessarily generate corrosion may lead to embrittlement at the crack tip and hence an increase in crack propagation rate. Some proposed mechanisms of environmental assisted crack growth are as follows [108].

1. Active corrosion of material at the crack tip
2. Adsorption of environmental species
3. Reactions of the bulk material ahead of the advancing crack
4. The formation of oxide films

### 2.8.1 Dissolution-based mechanisms

The slip dissolution model is based on the fact that the crack tip is passivated by a film and the film is then ruptured due to tensile stress [109][110]. The microstructural, mechanical and environmental factors that have an effect in the slip dissolution mechanism is described by Omar and Miguel [111].

### 2.8.2 Adsorption-based mechanisms

Based on the literature, the adsorption of environmental species enhances crack propagation by either a decohesion or an enhanced dislocation mechanism. Let us explore these two mechanisms further.

Benedicks in 1947 [112] was perhaps one of the first authors reporting the effects of adsorption on interatomic bonds. He argued that the wetting effect of liquids facilitates cracking by reducing the binding forces between surface atoms. In the late 1950 Uhlig [113] proposed that chemisorption of specific ions weakened the strained interatomic bonds at crack tips, hence promoting crack growth by a decohesion mechanism along a cleavage plane.

Lynch in 1977 [114] proposed an adsorption induced dislocation emission mechanism in SCC where, in this model, the adsorption of environmental species weakens interatomic bonds at crack tips, facilitating the formation of dislocations

as opposed to decohesion. Facilitating the dislocation formation promotes the coalescence of the crack tip with voids formed in the plastic zone ahead of the crack tip, therefore this led to a macroscopically brittle cleavage like fracture surface.

### 2.8.3 Film induced cleavage

The model of film-induced cleavage consists of repeated sequences of (i) formation of an environmentally induced brittle film at the crack tip, (ii) rapid fracture of the brittle film, (iii) continuation of brittle fracture into the substrate for a distance greater than 100x or 1000x the film thickness and (iv) crack tip blunting [115]. This model proposes that crack growth is discontinuous and crack arrest markings should be present on the fracture surface [115].

One of the assumptions of the film-induced cleavage model is that the crack in the brittle film propagates at significantly high velocities (hundreds of metres per second or more) and further propagates into the substrate [115]. It assumes that crack velocities decrease as it propagates due to dislocation formation or due to encountering obstacles such as slip bands. This leads to extensive dislocation activity and, ultimately, crack arrest or crack tip blunting [116].

De-alloyed or nanoporous films are effective in promoting cleavage, particularly if the porosity is fine. However, coarsening of the film may reduce its ability to inject a brittle crack into the substrate [116].

## 2.9 Other embrittlement mechanisms

Interfacial embrittlement (i.e. Intergranular embrittlement) is also a common embrittlement mechanism [117]. In this form of embrittlement, the metal's ability to relieve stress concentrations in regions such as notches is impaired due to the segregation of embrittling species (i.e. sulphur, boron and phosphorus). This means that the metal will not be able to withstand bending, impact or deformation and fails in a brittle manner. The mechanism of segregation is labelled as non-equilibrium segregation and is thought to occur due to the coupling of solutes to the vacancies in grain boundary sinks [117]. One of the proposed mechanisms is

that the absorbed solute reduces drastically the energy of formation of fresh surfaces exposed when fracture occurs [117].

A number of factors are known to affect interfacial embrittlement such as electronegativity of the solute or its atom size [118][119][120]. The weakening caused by elements such as sulphur, boron or phosphorus has been suggested to occur due to the difference in electronegativity between the impurity and the metal substrate. In addition, for a given electronegativity, a larger atom will be more embrittling than a smaller atom presumably due to the strains produced by the impurity. The difference in electronegativity between the impurity and the metal atom causes the impurity atom to draw charge from the metal atom to themselves, causing the metal-metal bonds to weaken [117].

## 2.10 C-ring test method

C-ring specimens have been used previously to study the mechanisms of stress corrosion cracking [121]. The setup consists of a C-ring specimen that is assembled with washers at either side of the specimen and a screw that goes through it. The idea of the C-ring specimen is that you can apply a tensile stress on the apex of the C-ring specimen by tightening the bolt [121]. Consequently, this reduces the outer diameter of the C-ring specimen. The two benefits of using C-ring specimens is that it does not require of a jig to apply the stress during the exposure and the specimens are relatively small in size. In this study, the small size (19 mm in length) of the C-rings enabled us to test several specimens in the hot zone of a furnace.

A standard methodology to undertake this test for stress corrosion applications has been developed previously and the standard provides an equation which relates the displacement that needs to be applied to attain a desires stress level on the apex region of the C-ring specimen (where the stress magnitude is maximum) [121]. However, the equation that relates the applied displacement to the stress magnitude in the apex of the C-ring has been designed for isotropic materials and for conditions where the temperature of the C-ring setup is the

same as the temperature of the test. Hence the effects of the component's thermal expansion do not affect the resulting stress distribution on the specimen.

The tests carried out in this thesis involve using single crystal nickel-based superalloys, which have highly orthotropic properties [102], and high temperature exposures. As a result, the orthotropic nature of the material and the difference between the temperature in which the C-ring setup is done and the exposure temperature must be considered when determining how much displacement should be applied to achieve a desired stress level at the apex of the C-ring.

As mentioned in [122], the stress of interest in the C-ring is the circumferential stress or the stresses that tend to open the cracks in the longitudinal direction. The stress is applied by tightening the bolt to compress the C-ring. There is a stress gradient throughout the thickness of the C-ring, which varies from maximum tension on one surface to maximum compression on the opposite surface [122]. The stress also varies around the circumference of the C-ring from near zero close to the bolt hole to a maximum (depending on the crystallographic orientation) at the middle section of the arc perpendicular to the stressing bolt.

According to the standard test guidelines (designed for isotropic materials), the required displacement to achieve a target stress level is calculated theoretically following Equations 1 and 2 from the ISO 7539-5 standard [121]. The calculated compression distance is based on the C-ring thickness, diameter, and elastic modulus. The constant-strain C-ring test involves constraining the specimen by tightening a bolt on one side and a nut on the other, such that the stress level in the apex region of the C-ring achieves the desired magnitude and does not exceed the material's yield strength at room temperature [121].

$$\Delta D = \sigma \pi d^2 / 4EtZ \qquad \text{Equation 36}$$

Where:

$\Delta D = Change\ in\ outer\ diameter$

$\sigma = Maximum\ stress$

$D = Outer\ diameter\ of\ the\ C-ring\ before\ stressing$

$t = Thickness$

$d = Mean\ diameter\ (D - t)$

$E = Young's\ modulus$

$Z = Correction\ factor\ that\ depends\ on\ the\ \frac{d}{t} ratio$

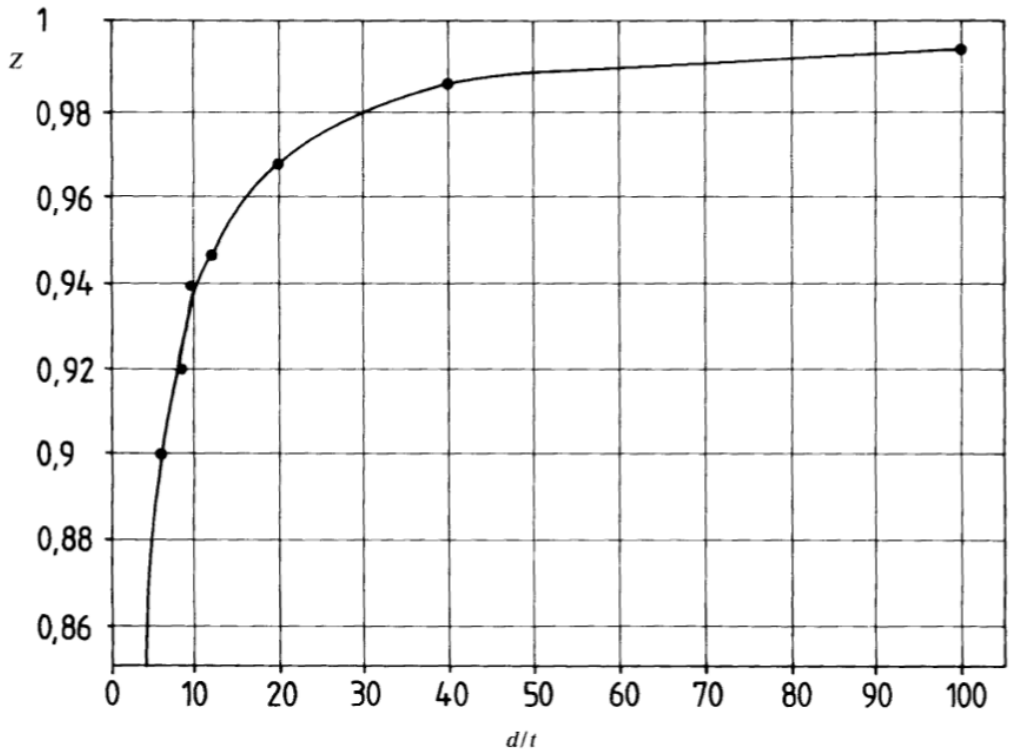


*Figure 22 – Correction factor as a function of d/t for C-ring stress calculation* [121]

The standard test guidelines are designed for isotropic materials [121]. Therefore, given the anisotropic nature of single crystal nickel-based superalloys, the equations provided in the standard test guidelines cannot be applied. For this reason, one of the aims of this study was to conduct finite element analysis to calculate the amount of deflection required to achieve the desired stress level.

Brooking et al. [123] has previously utilised the C-ring test method to study stress corrosion cracking in a hot corrosion environment and an FEA model was used to calculate the stress distribution in the C-ring specimens. However, the model used isotropic material properties, did not consider the secondary

crystallographic orientation of the single crystal nickel-based superalloys and steel nuts, bolts and washers were used. A major drawback of using steel as nuts, bolts and washers will eventually undergo significant stress relaxation during the test, as reported by Chapman et al. [124]. For that reason, Waspalloy nuts, bolts and washers were used in this thesis to minimise this stress relaxation. The methodology section will cover these aspects in more detail.

# 3 Methodology

As mentioned in the thesis structure, the first chapter of results compares the effect of different salts on the corrosion and crack initiation behaviour of CMSX-4 at 550°C. Based on the fact that sea salt was the only deposit that caused cracks to initiate after an exposure time of 400 hours, the rest of the work consisted in simplifying the salt chemistry of sea salt by focusing on the effect of NaCl, given that it makes up 75% wt of sea salt. In order to undertake these tests, C-ring specimens have been used throughout the project as a means of studying the effect of a sustained load and aggressive environments on the corrosion and crack initiation behaviour of superalloys.

The figure below highlights the chronological method that was used in this study to apply the sustained load on the C-rings, undertake the exposures and perform the characterisation.

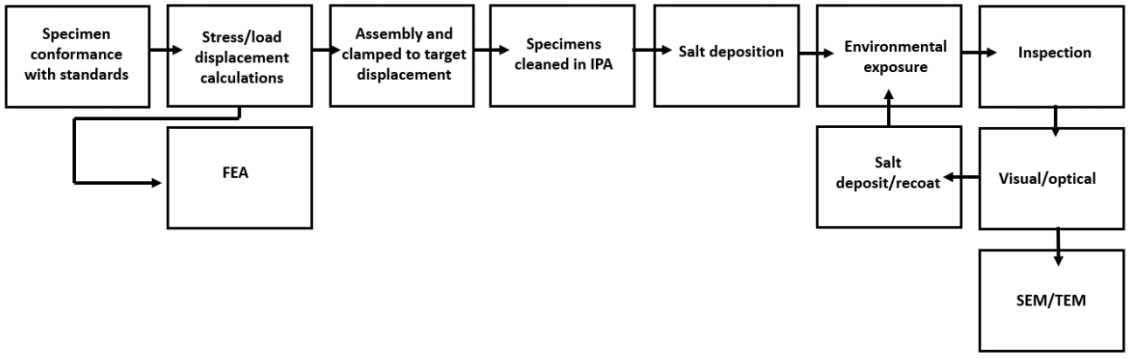


*Figure 23 – Sequential flowchart of C-ring test method*

The methodology section is divided in two parts. The first part consists in explaining the FEA model setup that was used to calculate the stress distribution on the C-ring, a description of the salting procedure and the exposure procedure of the C-ring to a high temperature gaseous environment. The second part describes the characterisation techniques that have been used. These include optical, SEM and TEM microscopy, synchrotron x-ray diffraction and nano XCT that has been utilised during the project.

Although this section provides a general description of the methodology followed throughout the thesis (e.g. a description of the FEA simulation used to apply the

stress on the C-rings, the method of salting), each results chapter (Chapter 5 and Chapter 6) has its own methodology section providing details of the stresses, the salts and the gaseous environment used in that particular test.

## 3.1 C-ring stress estimation method

### 3.1.1 Introduction

This section focuses on developing a finite element analysis model, that will enable us to calculate the required displacement that needs to be applied on the C-ring specimen to attain a desired stress level on the apex of the C-ring.

The CMSX-4 C-ring test specimens have been provided by Rolls Royce. And were produced from CMSX-4 bars in the fully solutioned and aged heat-treated condition as per Rolls Royce Ltd specification with a [001] crystallographic orientation aligned with the cylinder axis, following ISO 7539-5 guidelines. Regarding the heat treatment process, the as received bars are solution treated at 1276°C for 2 h, at 1287°C for 2 h, at 1296°C for 3 h, at 1304°C for 3 h, at 1315°C for 2 h, at 1321°C for 2 h, at 1324°C for 2 h, and then finally air cooled. Then, it is primary aged at 1140°C for 4 h, and the secondary age is done at 870°C for 16h. The dimensions of the machined C-ring specimen are shown in Figure 24. Two through holes of 7.0 mm (±0.05) diameter were drilled to compress the C-ring using a bolt, nut and two washers. The bolt, nut and washers used are made of commercial Waspalloy. Previous work has utilised steel washers, but there was a significant relaxation of stress on the C-ring during its exposure [124]. In this work, Waspalloy was used to minimise the stress relaxation on the C-ring.

A commercial FE software Ansys Workbench v19 was used to perform the simulation and analysis of the C-ring model. Figure 24 shows a three-dimensional (3-D) geometric model of the C-ring assembly that was used for the FE analysis. There are two key aspects that need to be considered when estimating the stress distribution on the C-ring.

1. Firstly, the applied deflection on the C-ring is performed at room temperature, whereas the test exposure is done at high temperature (≈ 550°C). The increase in temperature will affect the stress distribution on the C-ring due to the difference in the thermal expansion coefficient of the C-ring's material (CMSX-4) and the nut and bolt's material (Waspalloy). Therefore, a study of the resulting stress distribution at 550°C on the C-ring given a predefined deflection at room temperature must be undertaken.
2. Secondly, the secondary crystallographic orientation (SCO) (or kappa angle) is not controlled during the casting of the bars, which means that not every specimen used in this study has the same secondary crystallographic orientation. Eventually, specimens with different crystallographic orientations will be subjected to a different stress distribution when the same deflection has been applied to them. To investigate this effect, a predefined deflection of 0.44 mm has been chosen and a study has been undertaken to calculate the resulting stress distribution on the C-ring specimens with several secondary crystallographic orientations at 550°C. All specimens used throughout this project have a kappa angle between 20° - 40°.

### 3.1.2 FEA simulation setup

The first part of this section will summarise the setup and results of the FEA model.

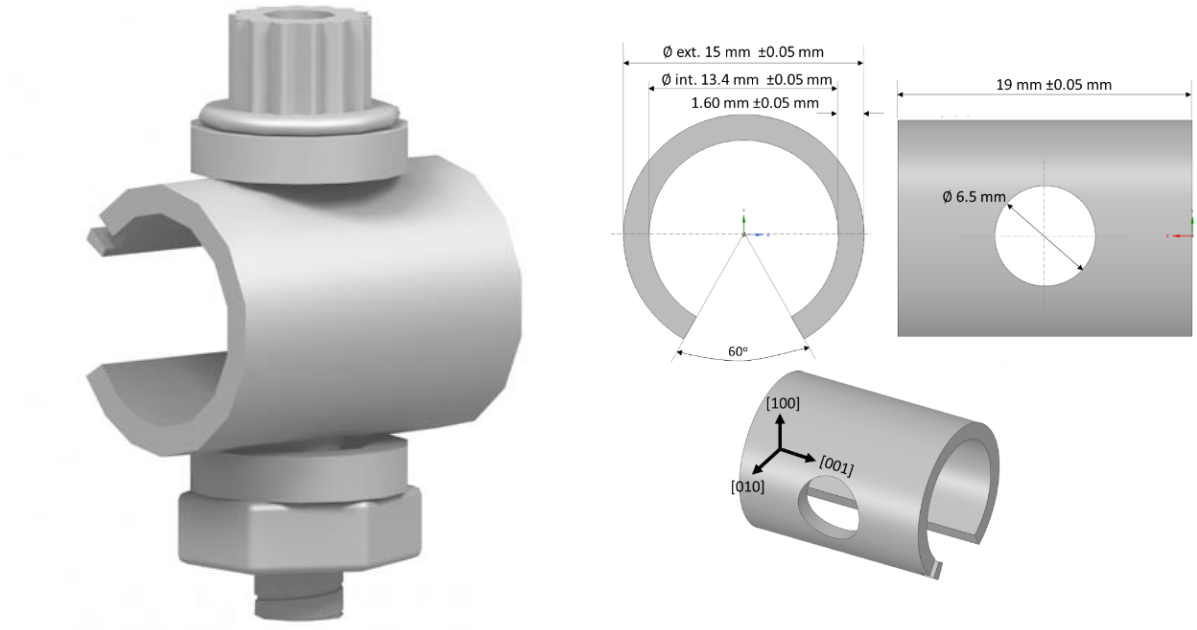


*Figure 24 – Dimensions of C-ring specimen used throughout this thesis*

An analysis of static structure and an anisotropic material model was used to compute the stress distribution in the C-ring geometric model. Table 8 shows the elastic constants of CMSX-4 (provided by Rolls Royce), which describes its mechanical response in the elastic regime when it is subjected to different kind of loads. The material properties were input according to the equations below provided by Sieborger et al. [102].

*Table 8. CMSX-4 elastic properties (provided by Rolls Royce Ltd)*

| Temperature (°C) | $E_{001}$ (MPa) | $G_{001}$ (MPa) | P. $R_{001}$ | Coefficient of thermal expansion |
|---|---|---|---|---|
| 0 | 1.2845E+05 | 1.31425E+05 | 3.7675E-01 | 1.2074E-05 |
| 100 | 1.2570E+05 | 1.2880E+05 | 3.78E-01 | 1.22E-05 |
| 300 | 1.18900E+05 | 1.23200E+05 | 3.81E-01 | 1.24E-05 |
| 500 | 1.1190E+05 | 1.16100E+05 | 3.85E-01 | 1.29E-05 |
| 520 | 1.11164E+05 | 1.153640E+05 | 3.85427E-01 | 1.298E-05 |
| 540 | 1.10456E+05 | 1.14603E+05 | 3.858E-01 | 1.306E-05 |
| 560 | 1.09756E+05 | 1.13819+05 | 3.8616E-01 | 1.314E-05 |
| 700 | 1.04000E+05 | 1.07900E+05 | 3.9E-01 | 1.38E-05 |

$$\overset{++}{C} = \begin{bmatrix} c_{11} & c_{12} & c_{12} & 0 & 0 & 0 \\ c_{12} & c_{11} & c_{12} & 0 & 0 & 0 \\ c_{12} & c_{12} & c_{11} & 0 & 0 & 0 \\ 0 & 0 & 0 & c_{44} & 0 & 0 \\ 0 & 0 & 0 & 0 & c_{44} & 0 \\ 0 & 0 & 0 & 0 & 0 & c_{44} \end{bmatrix} \quad \text{Equation 37}$$

Where:

$$c_{11} = \frac{E_{001}(1 - v_{001})}{(1 + v_{001})(1 - 2v_{001})} \quad \text{Equation 38}$$

$$c_{12} = c_{11}\frac{v_{001}}{1 - v_{001}} \quad \text{Equation 39}$$

$$c_{44} = G_{001} \quad \text{Equation 40}$$

Values for $E_{001}$, $v_{001}$ and $G_{001}$ at 20°C are as follows.

$$E_{001} = 1.28 \times 10^5\ Pa \qquad \text{Equation 41}$$

$$G_{001} = 1.31 \times 10^5\ Pa \qquad \text{Equation 42}$$

$$v_{001} = 0.377 \qquad \text{Equation 43}$$

Figure 25 shows the contact parameters that were defined for the FEA model, where a frictional contact (input value 0.3) was applied for the bolt-hole contact, the washer-C-ring contact, the nut-washer contact and the bolt-washer contact (the colours and the box in each image highlight the components involved in the contact parameters set up). Figure 26 shows the boundary conditions that have been defined for the FE analysis, where a fixed support was applied on the bottom face of the nut (highlighted in blue), and an axial displacement was applied on the bottom face of the bolt (highlighted in yellow). A tetrahedral mesh was applied on the C-ring, bolt, washer, and nut. The element size for the C-ring mesh was 0.0005 m, and the element size for the bolt, washer and nut mesh was 0.0008 m.

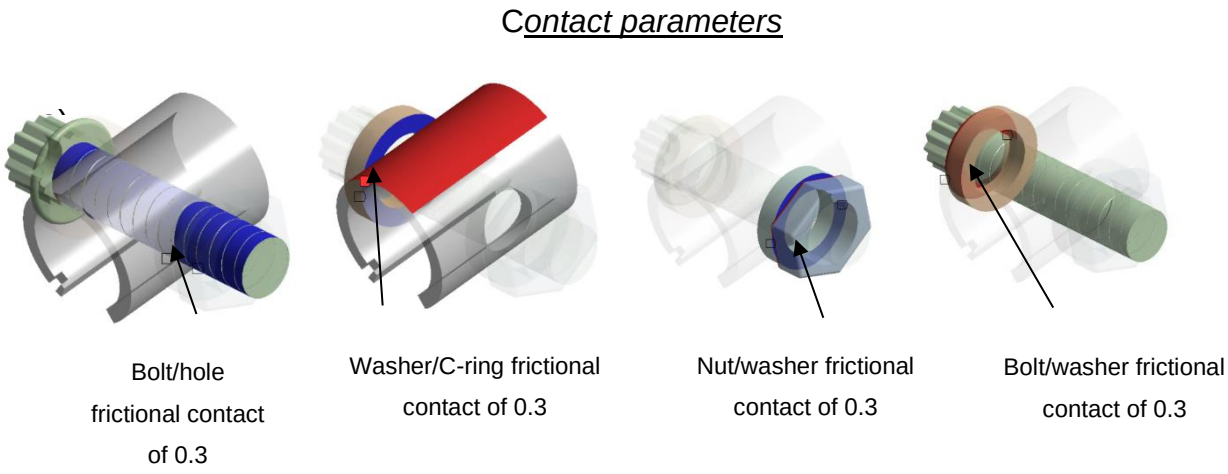


*Figure 25 – Contact parameters between the bolt-hole, washer-C-ring, nut-washer and bolt-washer in the FEA model*

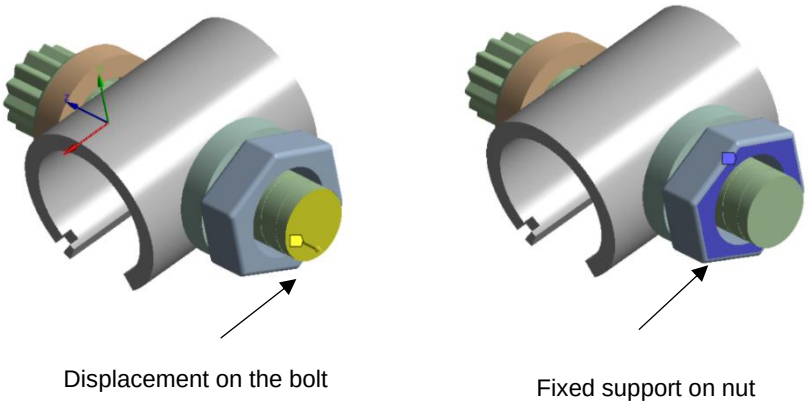


*Figure 26 – Displacement and fixed support set up in the FEA model*

### 3.1.3 Effect of thermal exposure on the resulting stress distribution on the C-ring specimen

In accordance with actual test conditions, the loading is set in two steps. The first step consists in exerting a load by applying axial displacement (in this case 0.44 mm has been applied) on the lower face of the bolt and applying a fixed support constraint on the bottom face of the nut to mimic the initial bolt-nut pre-tension procedure at room temperature (22$^{o}$C).

The second step consisted in increasing the temperature of the components from 22°C to 550°C. The increase in temperature causes a thermal expansion of the C-ring and the other components which, in turn, causes a relaxation in the stress on the C-ring specimen. The Maximum Principal Stress (MPS) criterion is read as the calculation results of the C-ring model. For simplicity, a secondary crystal orientation of 0° is applied in this model. Figure 27 shows the resulting stress distribution on the C-ring at both room temperature and at 550°C. The graph in Figure 27 shows the stress distribution from the edge of the left-hand side of the C-ring, labelled “a” to the edge of the right-hand side of the C-ring, labelled “b” (this is also highlighted by the white dashed lie). At both temperatures it can be observed that the peak MPS occurs on the edges and on the middle region of the specimen’s apex.

Figure 27 shows that the MPS at the peak location drops from 921.2 MPa on the edge of the C-ring to 768.3 MPa as the temperature increases from 22ºC (step 1) to 550ºC (step 2). The decrease in stress is due to the difference in thermal expansion between the C-ring (CMSX-4) and the rest of the components (made of Waspalloy). This difference in the magnitude of the component’s expansion causes a stress relaxation on the C-ring specimen.

Evangelou [3] found that the yield stress of CMSX-4 is approximately 873 MPa at 550°C, so by applying a displacement of 0.44 mm on the C-ring. the peak MPS at 550°C is 768.3 MPa (assuming a kappa angle of 0°), which is below the yield strength of CMSX-4.

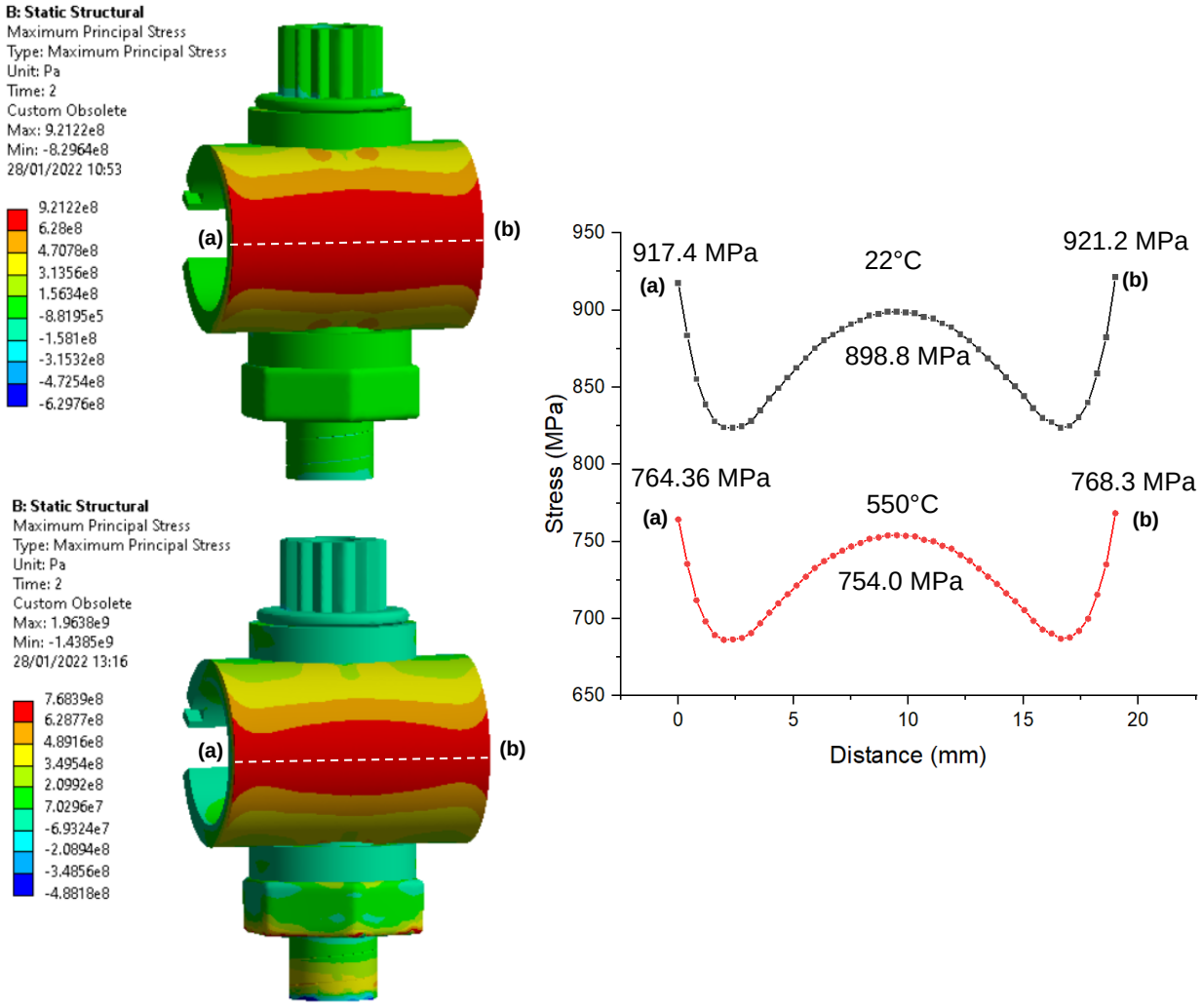


*Figure 27 – Stress distribution on the C-ring at 22°C and 550°C with an applied deflection of 0.44 mm*

### 3.1.4 Effect of secondary crystal orientation on the stress distribution of the C-ring at 550°C

During the manufacture of the specimens, the primary crystal orientation (001) is controlled and aligned with the cylinder axis of the C-ring. However, the secondary crystal orientation is not controlled, and its variation affects the stress distribution for a predetermined amount of deflection. Therefore, a sensitivity study was undertaken to examine the effect of secondary crystal orientation on the stress distribution of the C-ring. Again, an axial displacement of 0.44 mm was applied to the bottom face of the bolt.

For the simulation setup, a material coordinate system was applied to the C-ring specimen. The y-axis of the material coordinate system represents the [001] and the x and z axis represent the [100] and [010] directions respectively. To change the secondary crystallographic orientation, the material coordinate system was rotated about the y-axis, as shown in Figure 28.

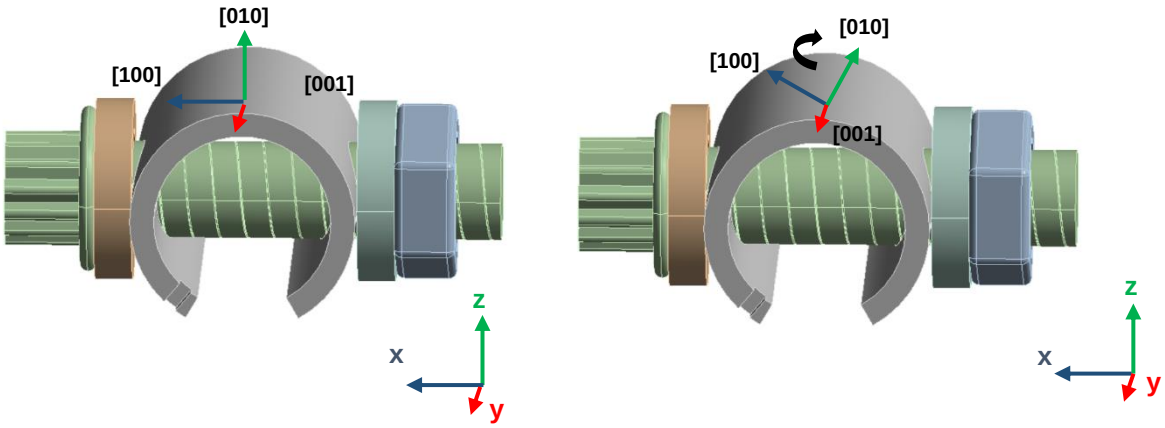


*Figure 28 – Rotation of the material coordinate system applied to the C-ring specimen*

The results shown in Figure 29 represent the stress distribution of C-rings with different SCO at 550°C. According to the results, the maximum “bell shaped” stress region on the C-ring shifts towards the lower side of the bolt as you increase the secondary crystallographic orientation between 0 and 45°. In addition to that, the stress magnitude along the maximum “bell shaped” stress region decreases from 0 to 45°C with the drop from 30° to 45° being very significant.

*Effect of secondary crystallographic orientation on stress distribution of the C-ring at 550°C*

SCO (κ) = 0°

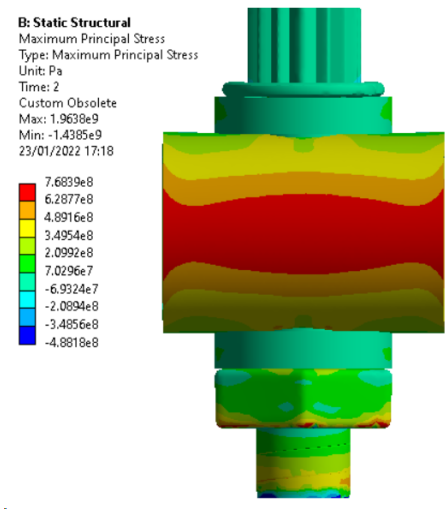


SCO (κ) = 10°

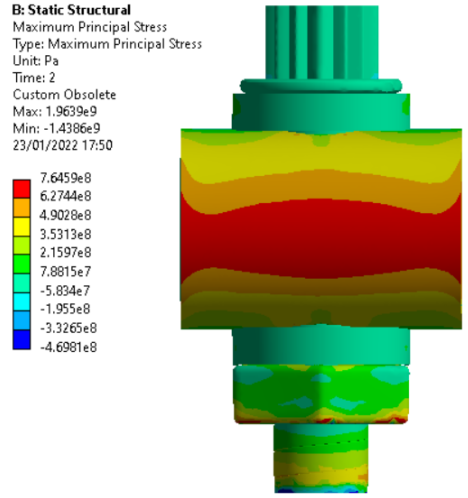


SCO (κ) = 20°

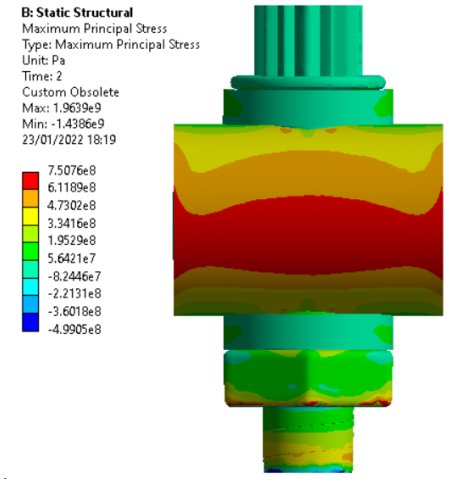


SCO (κ) = 30°

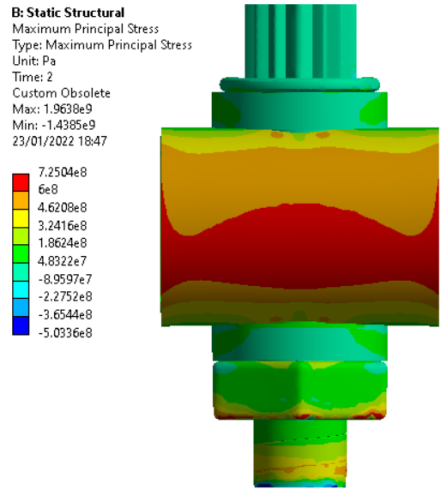

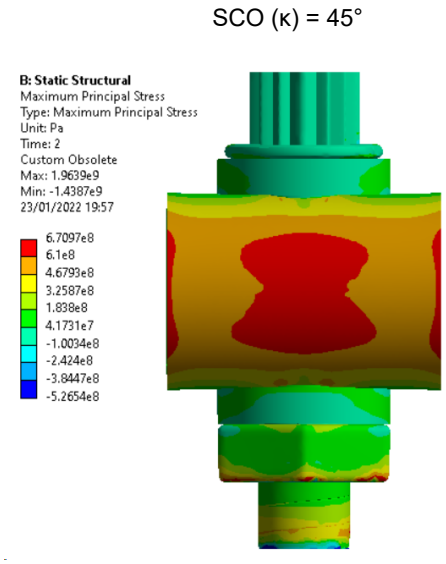


*Figure 29 - Effect of SCO (0° - 45°) on the stress distribution of the C-ring at 550°C with an applied displacement of 0.44 mm*

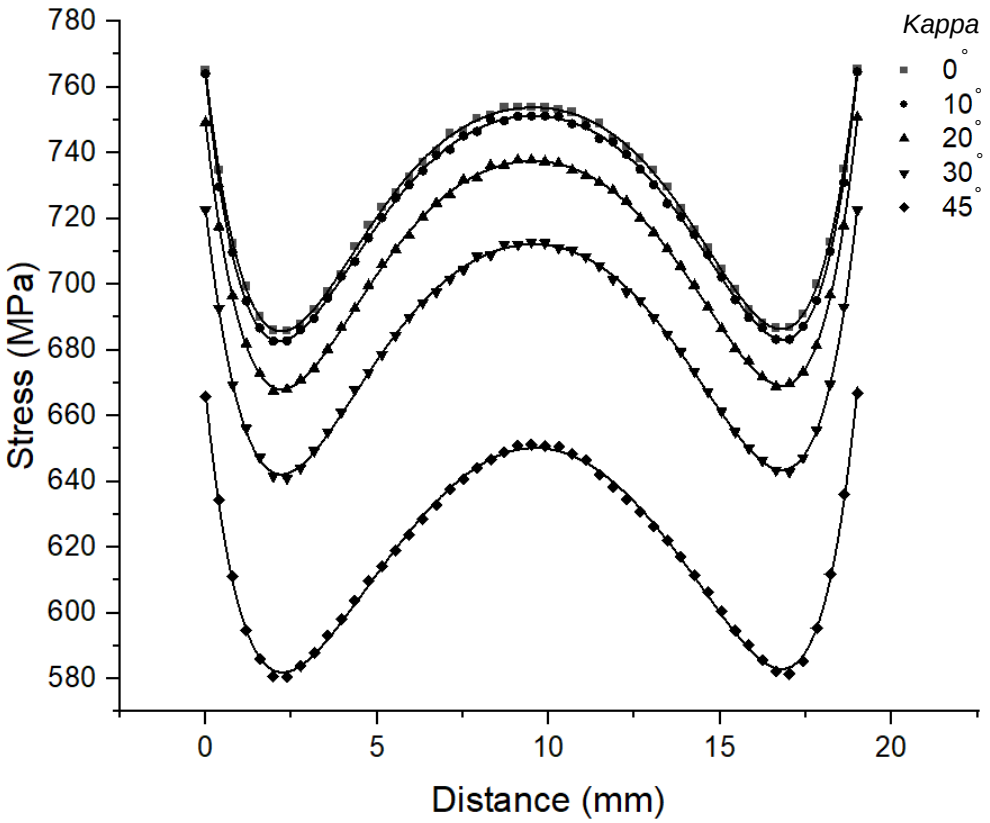


*Figure 30 – Graph showing the stress distribution along the region of maximum stress of the C-ring specimen at different values of secondary crystallographic orientation at 550°C*

## 3.2 Comparison of strain gauge measurements with calculated values of strain from the FEA model

To validate the FEA model, strain gauge measurements were undertaken to compare with calculated strain values from the FEA model. The strain gauges measured the strain value at the apex's centre of two C-ring specimens that had a kappa angle of 61.4° and 80.2°. The strain value was measured for applied displacements of 0.2 mm, 0.3 mm and 0.4 mm at room temperature and the displacement was applied with the displacement jig described in section 3.3.

For the strain calculation, maximum principal elastic strain values were calculated along a path (arc shaped) that went from the top hole to the bottom hole of the C-ring as highlighted by the coloured line in Figure 31. Strain calculations were performed in intervals of 0.25 mm along that path; therefore, in total, 69 values of strain were calculated. As we are mainly interested in the strain values at the centre of the C-ring's apex, only the strain values that were within 1.5 mm of the centre-point in the apex (7 strain values in total, which are highlighted in Figure 31 (b)) were averaged and compared with the measured value from the strain gauge. The measured values and calculated values are shown in Table 9. Table 9 shows that the % error in the difference between the calculated strain and the measured strain varies from 1.61 % to 12.82 %. This % error difference is not significantly high, seems to capture the secondary crystal orientation effects, and supports the correct estimation of the stress applied on the C-rings at room temperature.

Eventually, there are several sources of error that may have led to the difference in measured and calculated strain values. These errors include the following:

1. A slight difference between the thickness of the C-ring used in the FEA model compared to the actual C-ring, The thickness used in the FEA model was 1.6 mm; however, the tolerance of the C-ring's thickness is ± 0.02 mm, and this difference may have resulted in some difference between calculated and measured values of strain. For future work, the

real thickness of the C-ring should be used to minimise the error difference between the calculated strain and measured strain.

2. Although the main purpose of this test was to calculate the strain in the exact region where the strain gauge was attached on the C-ring, getting a perfect match is unlikely. The strain gauge may not have been vertically aligned between the through holes of the C-ring, and the strain gauge may not have been placed in the exact centre position of the C-ring's apex. Eventually, this would lead to differences between measured strain values and calculated strain values.
3. The resolution of the displacement applied by the jig, which is 0.001 mm is another factor to consider. This means that although the applied displacement in the FEA model was set to 0.2 mm, 0.3 mm and 0.4 mm, the real displacement applied during the strain measurement may have deviated by 0.001 mm for each displacement applied. Therefore, there will be a slight difference between the real displacement applied on the C-ring, and the displacement applied in the FEA model.

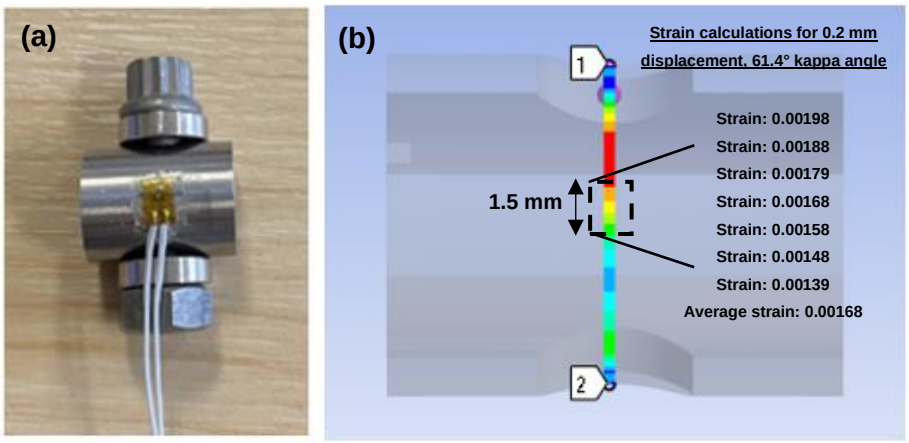


*Figure 31 – (a) Strain gauge position on the C-ring specimen, (b) strain calculations in the apex centre of the C-ring from the FEA model*

*Table 9 – Comparison of strain measured values with calculated FEA strain values*

| Kappa angle (°) | Displacement (mm) | Strain measured | Strain calculated | % Error |
|---|---|---|---|---|
| 61.4 | 0.2 | 0.00187 | 0.00168 | 10.09778 |
| | 0.3 | 0.00287 | 0.00260 | 9.571926 |
| | 0.4 | 0.00348 | 0.00354 | 1.60591 |
| 80.2 | 0.2 | 0.00286 | 0.00249 | 12.8231 |
| | 0.3 | 0.00404 | 0.00383 | 5.27263 |
| | 0.4 | 0.00533 | 0.00521 | 2.3841 |

## 3.3 Sample loading and salting

A jig developed by Rolls Royce was used as an automated tool to apply the desired displacement on the C-ring specimens. The C-ring is held in a jig, slotted into a nut holder which is spring loaded to keep the C-ring in place as a stepper motor tightens the bolt on the C-ring. An illustration of the setup is shown in Figure 32.

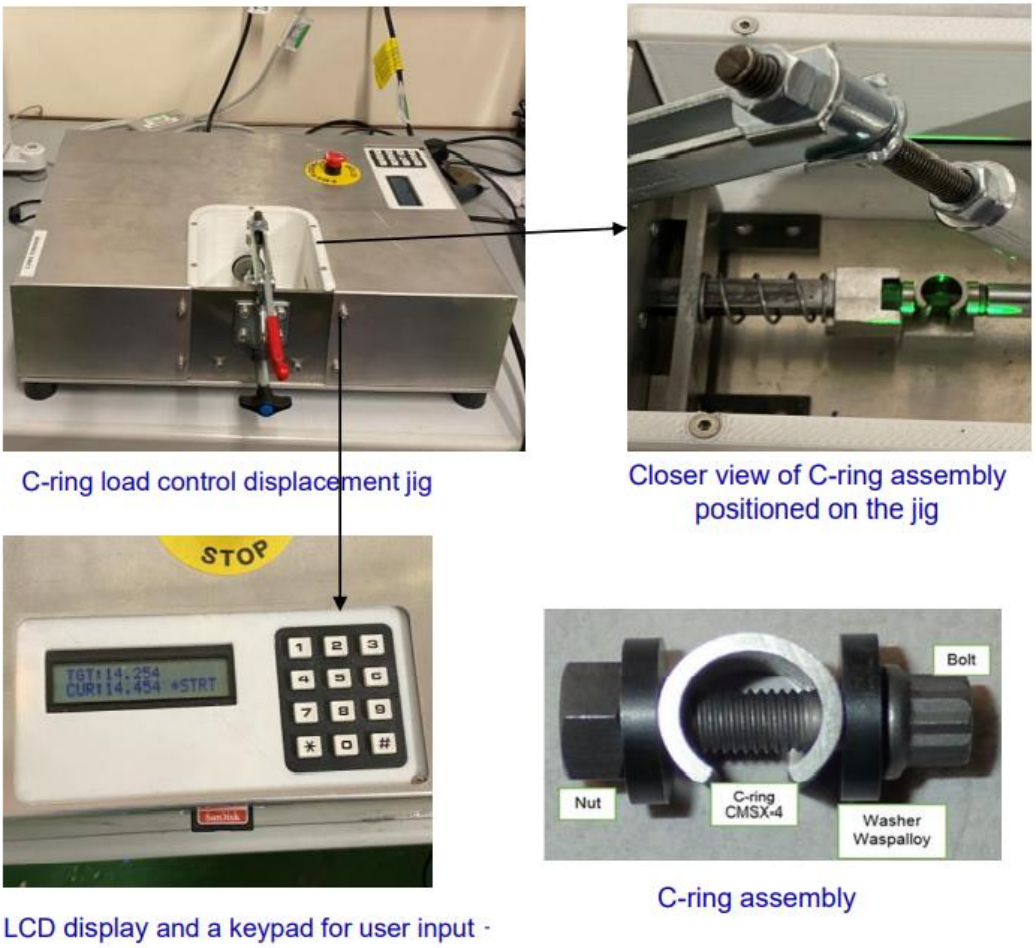


*Figure 32 – Load control displacement jig for C-ring set up*

The system measures the initial outer diameter of the C-ring using a laser, and subsequently the desired displacement is entered in the keypad. Both the stepper motor and laser are connected together in a feedback loop through an Arduino (microcontroller), so the reduction in outer diameter is measured in situ as the bolt is tightened until it reaches the outer diameter of interest. The outer diameter measurement has an absolute uncertainty of 0.001 mm. Prior to salting, the specimens were cleaned using Isopropyl alcohol (IPA) and then placed on a hot plate at 200°C. A saturated solution of deionised water + salt was used to spray the deposit onto the surface of the sample. Once the sample was heated, the saturated solution was sprayed onto the surface of the sample, which caused the water in the sprayed deposit to evaporate, leaving behind the salt.

The salt flux used throughout these studies was 1.2 µg/cm$^2$/hr and the region salted on the C-ring was a 3 cm$^2$ area. A mask was designed to ensure a 3 cm$^2$ of the front side (apex) was salted. So, for a 3 cm$^2$ and a 50-hour exposure, a target of 0.18 mg of salt was applied to the specimen.

After salting, the specimens were placed in a horizontal furnace and exposed to the high temperature gaseous environment. The specific time, temperature and gaseous conditions will be specified in each chapter.

## 3.4 SEM/EDS

Analytical electron microscopy was performed using a Tescan S8000 and the samples were analysed by both secondary and backscattered electrons. The instrument was equipped with an Oxford instruments EDX system. The acceleration voltage used for plan view imaging of the surface was 20 KeV and a beam current of 3 nA.

To characterise the corrosion products formed during the test, cross-sectional analysis and focused ion beam milling was undertaken. Conventional cross-sectional techniques typically involve encasing the sample in an epoxy resin, and then polishing to a flat surface. However, the cutting and polishing process may generate stresses and the lubricating liquids may dissolve the alkali or metal chlorides as well as damaging the often-fragile corrosion scales. For that reason, the microstructure of selective features was examined through cross-sections using a FIB-workstation. This enables us to pinpoint specific features and make cross-sections up to 40 µm surrounding a region of interest. Ultimately, if the region of interest was too large, FIB processes take too long to carry out and conventional cross-sectional techniques were employed.

Electron transparent thin lamellae TEM specimens were prepared using an FEI Helios 600i dual beam focussed ion beam (FIB) instrument. The FIB microscope was equipped with gas injection sources, which enable deposition of platinum and an Omniprobe 100.7 micro-manipulator used for specimen manipulations.

Thin lamellae were prepared by a lift out method similar to that described by Tomus [125] and Gianuzzi [126]. Specimens were excavated from bulk samples by first depositing a strap of Pt, to help protect the underlying material, before milling trenches either side of the region of interest. During the trenching and initial stages of milling an acceleration voltage of 30kV and high beam current (21nA) was selected for fast material removal rates. The lamellae were released from the bulk sample, by making a J-cut incision, subsequently specimens were transported to Cu support grids, using the Omniprobe manipulator and attached to the grid with ion beam deposited platinum. A target thickness of approximately 80nm was achieved by thinning with a 30kV Ga ion beam and reduced beam currents (80pA to 2.5nA); the lamellae were tilted ± 2° to the ion beam during this preparation step. Specimens were finished by applying a low kV (5kV) polish to help remove material damaged by previous stages of thinning.

## 3.5 TEM

Analytical TEM and STEM observations were performed using a LaB6 equipped JEOL 2100+ instrument, operating at 200kV. EDS analysis was carried out using an Oxford Instruments X-Max 65T EDS Detector and Aztec software.

## 3.6 XRD

Given the thin scales that form at the moderate temperatures tested, high resolution x-ray diffraction was required for accurate identification of the phases formed. The C-ring specimens were examined for phase identification using synchrotron X-ray diffraction (SXRD) at the Diamond Light Source synchrotron, Oxfordshire, UK.

Similar to conventional X-ray diffraction, synchrotron X-ray diffraction works on the principle of Bragg's law, so it relates the positions of the peaks obtained to the atomic structure of crystalline materials. Due to the higher flux, the well-defined wavelength and improved collimation in synchrotron radiation, SXRD improves the resolution of diffraction peaks compared to conventional XRD. This

technique made it possible to resolve phases that would have otherwise been significantly challenging using conventional XRD.

# 4 Effect of stress and salt chemistry on the high temperature corrosion behaviour of CMSX-4 in a sulphur containing environment.

## 4.1 Introduction

The aim of this chapter is to gain insight into the effect of $Na_2SO_4$, $CaSO_4$ and sea salt on the stress corrosion cracking mechanisms in CMSX-4, when exposed to a 50 ppm $SO_2$ – air environment at 550°C.

With regards to the salt selection for this study, $Na_2SO_4$ is of key interest as it is the main driver for Type I and Type II hot corrosion in jet engines. Although 550°C is below the temperatures at which Type I and Type II hot corrosion occurs, Kistler et al. [127] has shown that accelerated corrosion rates occur at these moderate temperatures and a solid-state mechanism was postulated. However, the influence of stress on the high temperature corrosion behaviour and near surface weakening in the presence of $Na_2SO_4$ and a sulphur-containing environment has not yet been investigated.

In addition, a common mineral deposit present in the region under the platform of turbine blades is anhydrous calcium sulphate. Calcium sulphate has been reported to be present in locations where unpredictable failures have occurred. Nevertheless, the effect of $CaSO_4$ on the corrosion degradation and crack initiation mechanisms in stressed components has not yet been investigated at 550°C.

Further, sea salt is a contaminant that enters the jet engines in the air inlet, particularly in marine environments. Sea salt contains alkali chlorides such as NaCl and $MgCl_2$ and as discussed in the literature review section, alkali chlorides are known to be highly corrosive at these intermediate temperatures due to the potential release of $Cl_2$, HCl and its ability to breakdown a protective oxide scale. Hence, the effect of no salt, $Na_2SO_4$, $CaSO_4$ and sea salt on the high temperature corrosion behaviour and near surface weakening of CMSX-4 under a sustained load was studied.

## 4.2 Methodology

C-ring specimens were loaded to achieve 700 MPa of stress in the apex region of the C-ring following the FEA calculations described in section 3.1.2.

The secondary crystallographic orientation of specimens used in this study is 20°, and Figure 33 shows the calculated stress distribution.

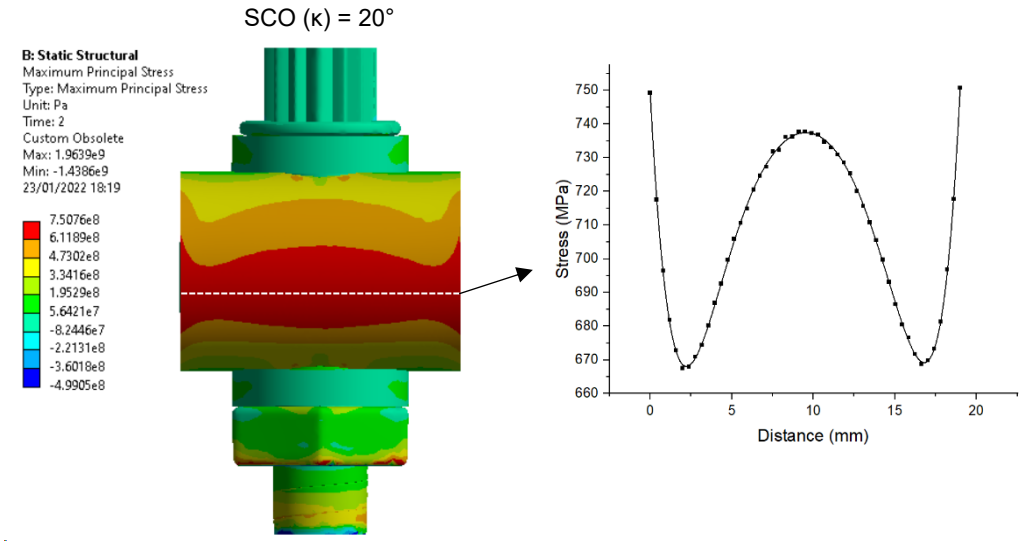


*Figure 33 – Stress distribution on a C-ring with a SCO of 20° at 550°C (applied displacement of 0.44 mm)*

### 4.2.1 Salting

The specimens were salted with a flux of 1.2 µg/cm$^2$/hr for each of the salts applied. Given that the coverage area is 3 cm$^2$, this translates to a 0.18 mg deposit recoat on each specimen every 50 hours. The weight percent of sea salt constituents are given in Table 10.

*Table 10 - Wt % of sea salt constituents BS3900/F4 (1968)*

| Constituent | Wt% |
|---|---|
| NaCl | 76.6 |
| $NaHCO_3$ | 0.58 |
| KCl | 2.13 |
| NaBr | 0.82 |
| $MgCl_2$ | 7.01 |
| $MgSO_4$ | 9.65 |
| $CaCl_2$ | 3.21 |

The specimens were then exposed in a clean alumina liner inside a horizontal furnace. The temperature was kept at 550 ± 1°C. The gaseous atmosphere consisted of 50 ppm $SO_2$ – air. The specimens were exposed for a total of 400 hours and were resalted every 50 hours of exposure. After the exposure, the samples were stored in desiccators and subsequently characterised. For the characterisation, the samples were sectioned, hot mounted and subsequently ground and polished for SEM assessment. Figure 34 shows SE images that were taken before the exposure to show the morphology of the salt deposited on the specimen.

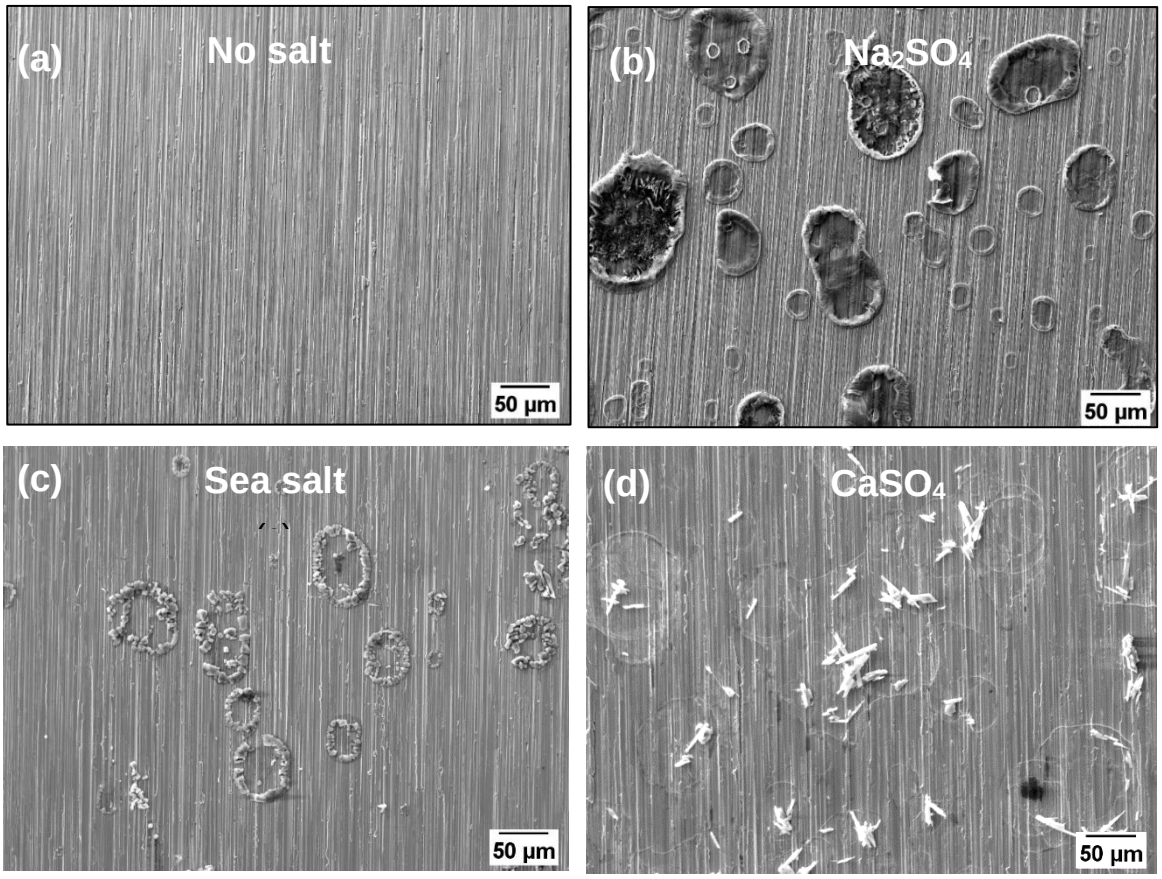


*Figure 34 – SEM top surface images of salted C-rings before the exposure*

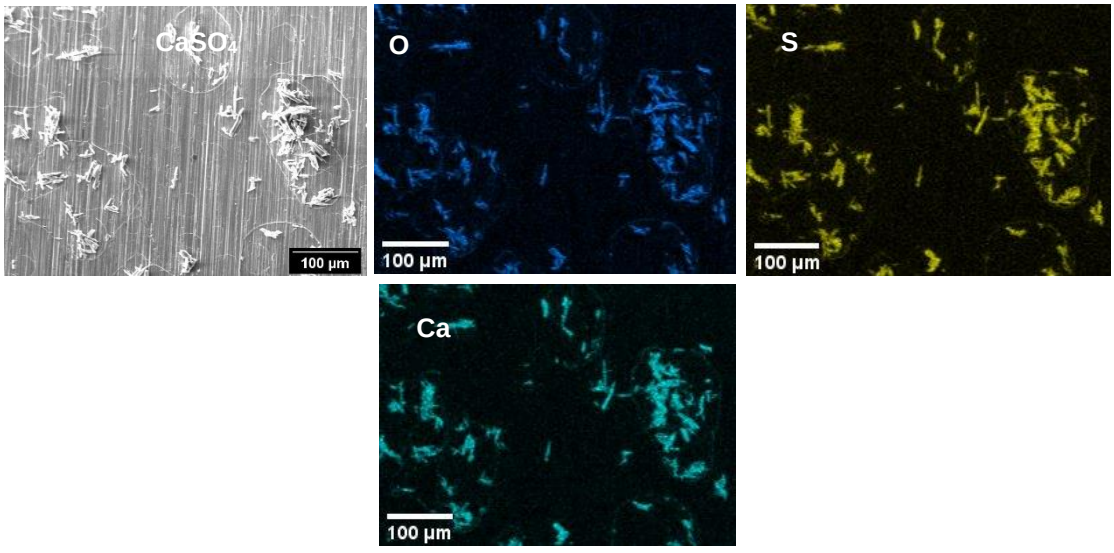


*Figure 35 – EDS map before the exposure of the $CaSO_4$ salted specimen*

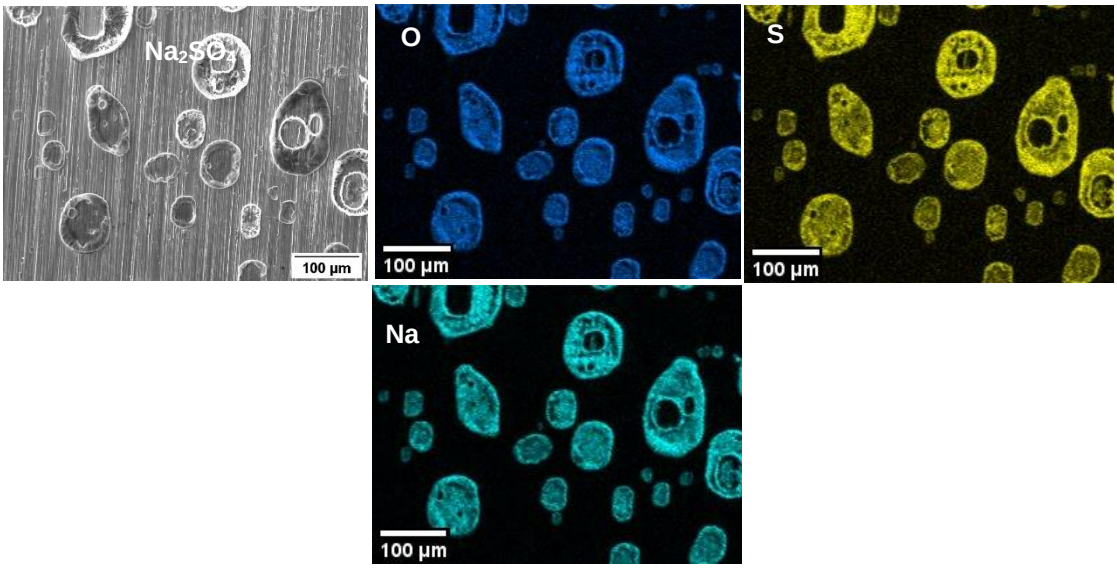


*Figure 36 – EDS map before the exposure of the $Na_2SO_4$ salted specimen*

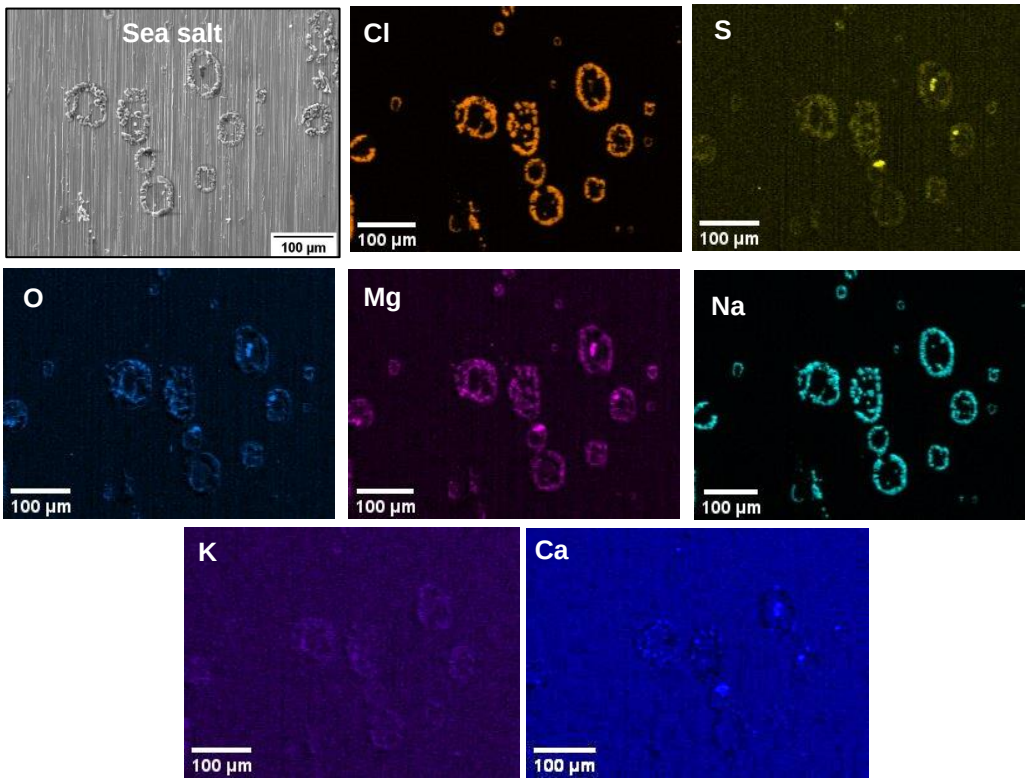


*Figure 37 – EDS map of the top surface of the C-ring salted with sea salt before the exposure*

## 4.3 Results

### 4.3.1 Characterisation of the sea salt, $CaSO_4$, $Na_2SO_4$ and non-salted samples

Figure 38 shows optical images of the non-salted, $Na_2SO_4$, $CaSO_4$ and sea salt coated specimens after the 400-hour exposure. From these images it is evident that the non-salted sample and $CaSO_4$ salted sample did not undergo as much corrosion attack as the $Na_2SO_4$ and the sea salt salted specimen.

Based on the top surface SEM and cross-sectional BSE images shown in Figure 39, no cracks were observed on the non-salted, $CaSO_4$ and $Na_2SO_4$ salted samples, but cracks were observed on the sea salt salted sample.

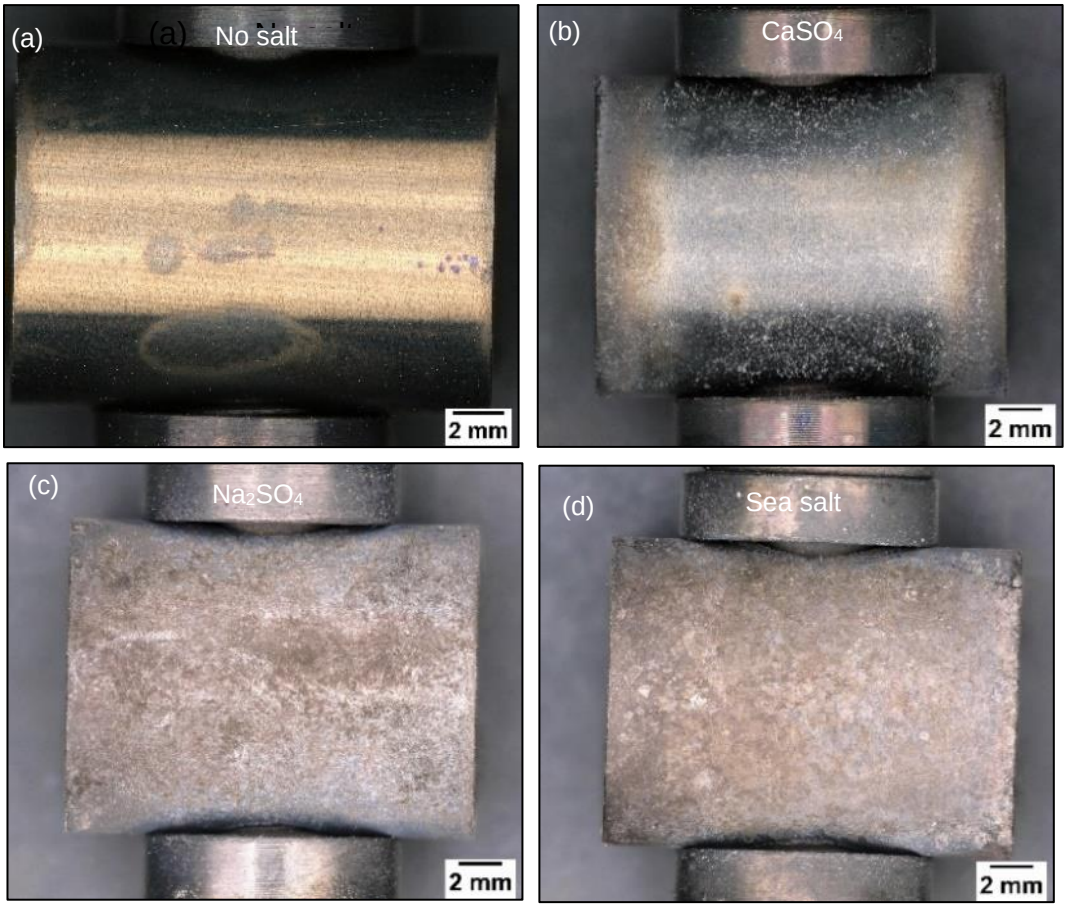


*Figure 38 – Optical microscope images of the C-ring after 400 hours of exposure*

Based on the BSE images shown in Figure 39, the non-salted and $CaSO_4$ coated specimens did not undergo a significant amount of corrosion attack and cracks were not detected after 400 hours of exposure. Nevertheless, based on the EDS map in Figure 42, an inner scale of approximately 0.8 µm rich in Al and Cr, O and S formed on the $CaSO_4$ salted specimen. Given that this specimen was not characterised with SXRD, it is challenging to identify what phases formed in the inner scale. Nevertheless, possible phases present in the inner scale may be a mix of a transition type $Al_2O_3$ and CrS.

The specimen salted with $Na_2SO_4$ formed a slightly thicker inner scale than the $CaSO_4$ salted specimen, measuring approximately ~1.8 µm. This is based on a single measurement on one BSE image. The inner scale was also rich in Al, Cr, O and S (presumably a transition type $Al_2O_3$ and CrS may also be present in the inner scale). In addition, traces of NiO were formed within the $Na_2SO_4$ deposit.

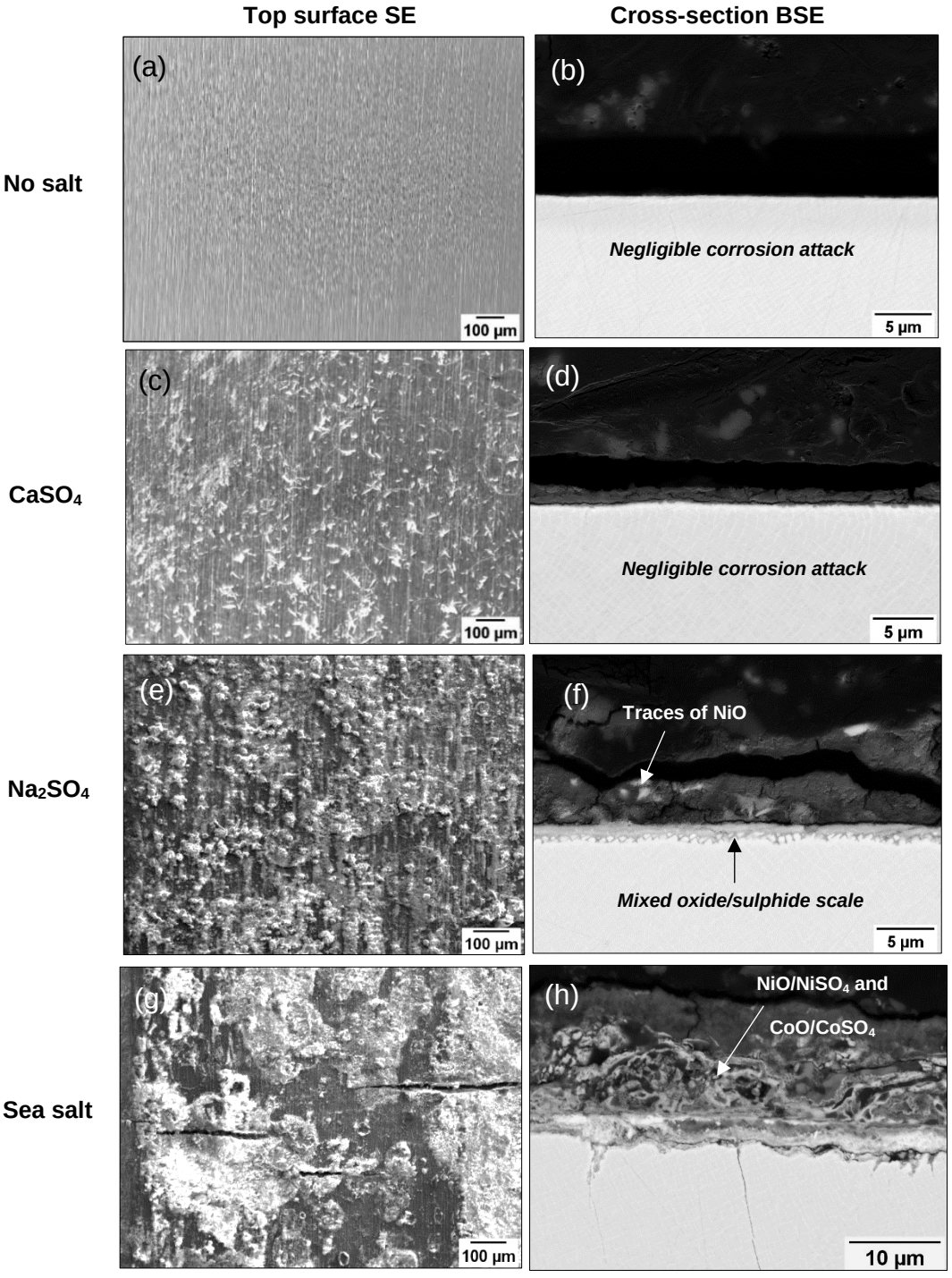


*Figure 39 - Plan view and cross sectional view images of the C-rings after 400 hours of exposure*

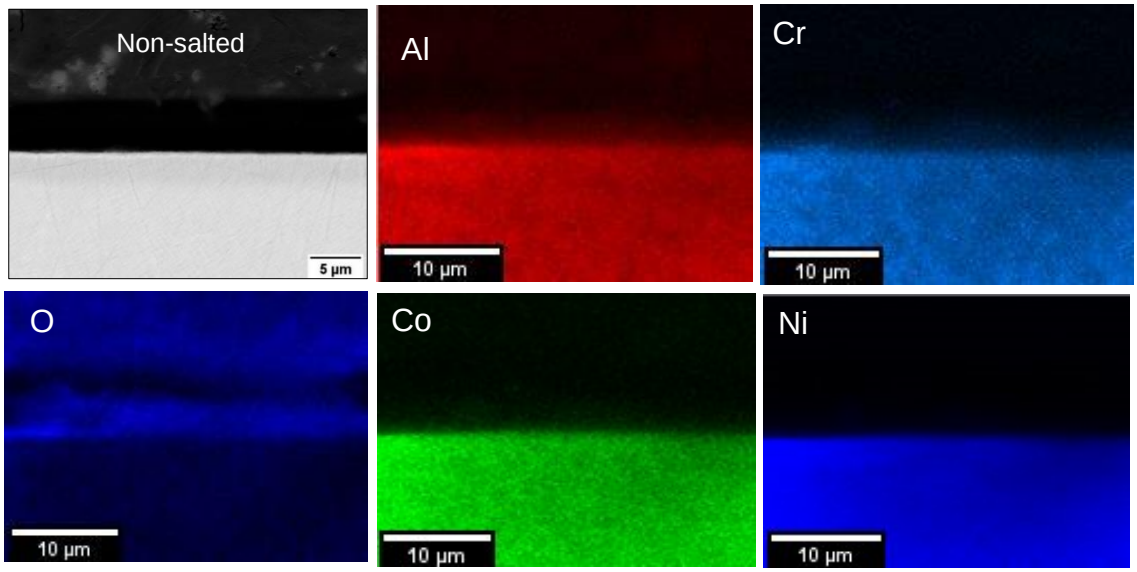


*Figure 40 - Cross-sectional EDS map of non-salted C-ring exposed to 400 hours*

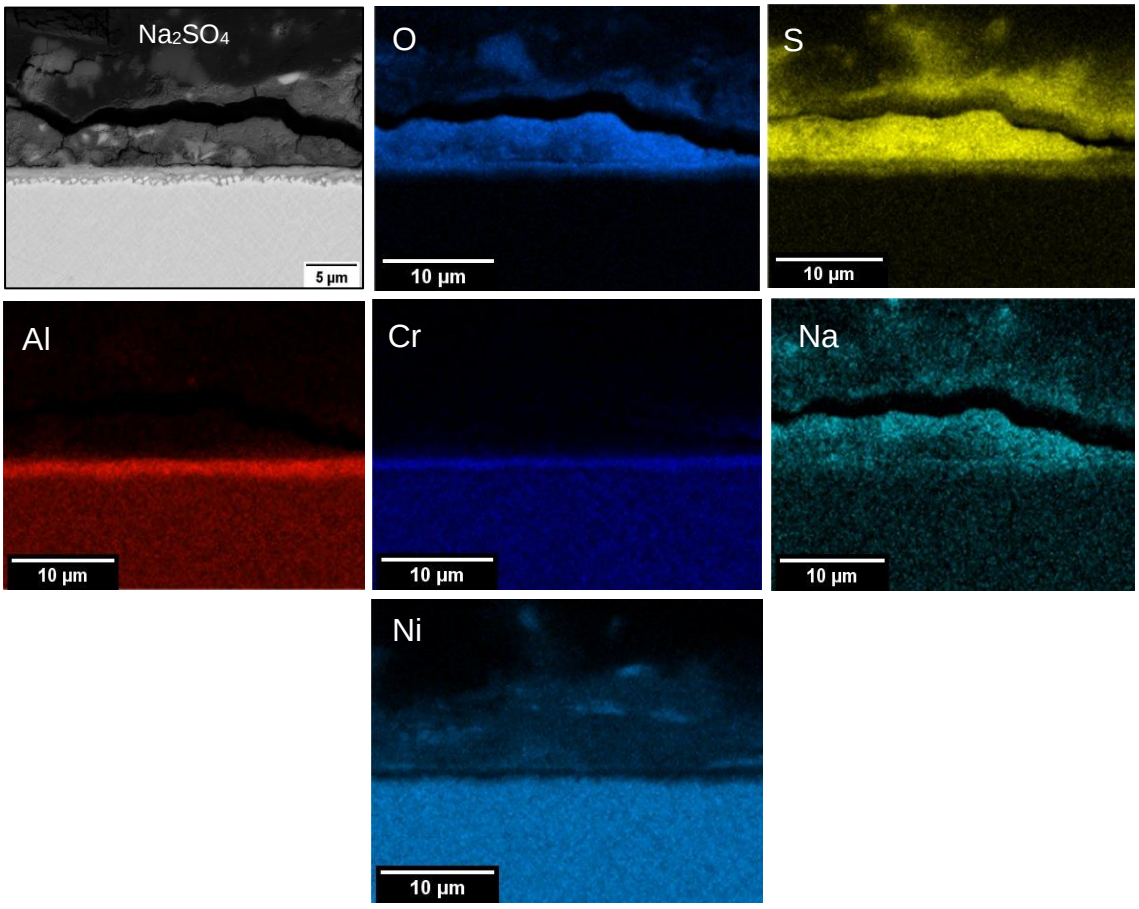


*Figure 41 - Cross-sectional EDS map of C-ring salted with $Na_2SO_4$ salt exposed to 400 hours*

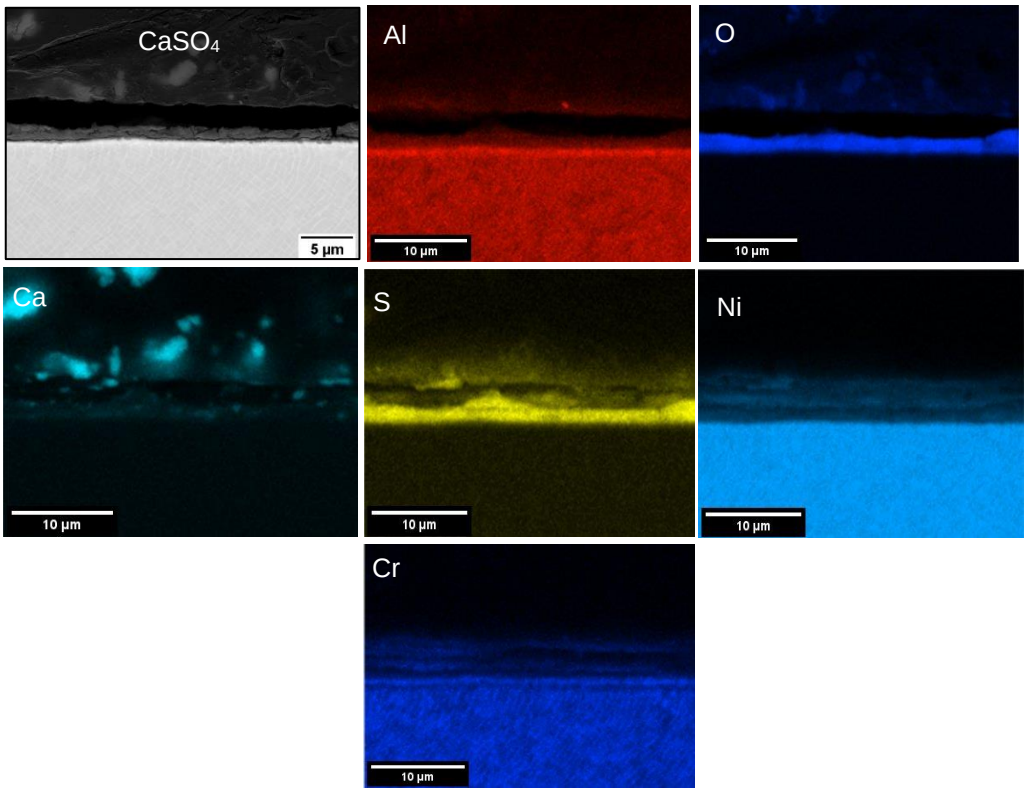


*Figure 42 - Cross-sectional EDS map of C-ring salted with $CaSO_4$ salt exposed to 400 hours*

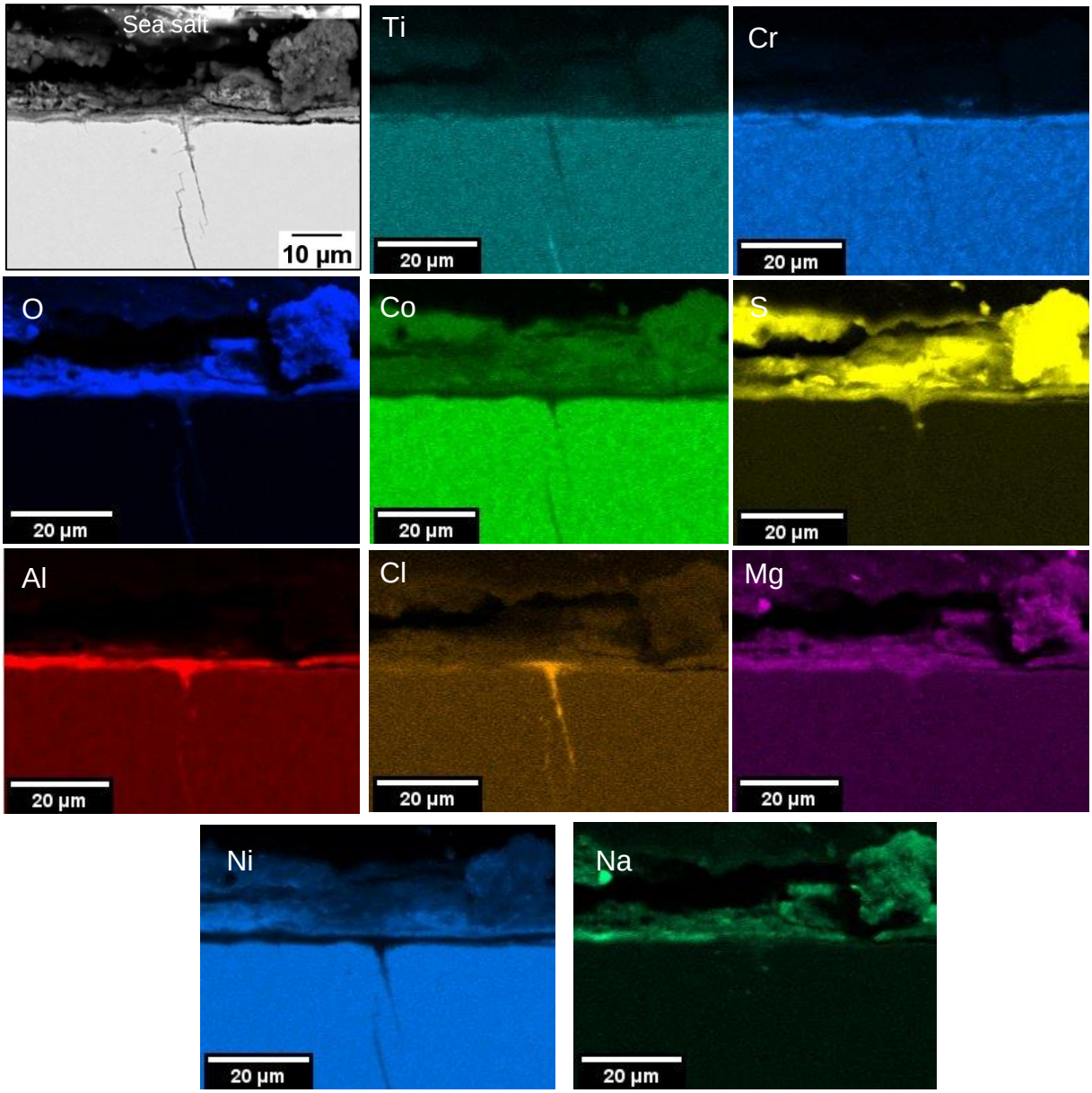


*Figure 43 – Cross-sectional EDS map of C-ring salted with sea salt exposed to 400 hours*

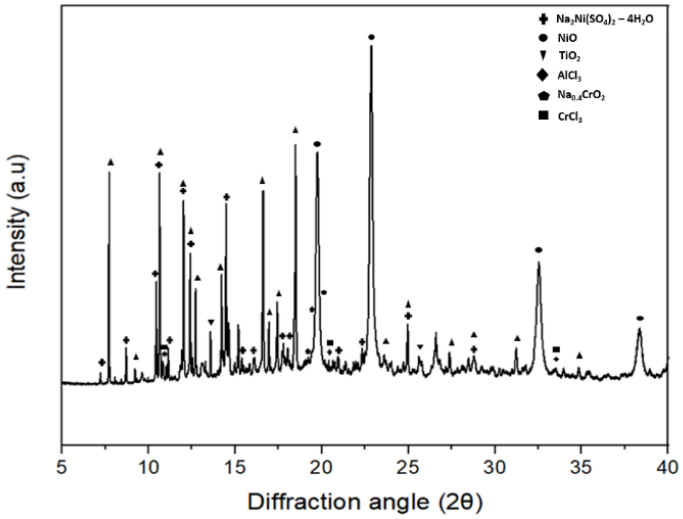


*Figure 44 – SXRD of C-ring salted with sea salt exposed to 400 hours*

The thickness of the external scale (~12 µm) and internal scale (~3.5 µm) formed on the specimen salted with sea salt is significantly higher than the other tested salts. Figure 45 shows cracks extending up to 1.3 mm deep into the substrate. The cracks with highest crack depth occurred slightly deviated from the apex (towards the C-ring hole), which agrees well with the highest stress region in the FEA model (for a kappa angle of 20°) shown in Figure 33. The scale formed was highly porous, less adherent to the alloy and showed a higher tendency to spall during cooling.

Based on the SXRD characterisation and the EDS map in Figure 43 and Figure 44 a mixture of $Al_2O_3$ and $AlCl_3$ formed in the innermost region of the scale, below a mixed $Cr_2O_3$ and $CrCl_3$/$CrCl_2$ scale. High concentrations of NiO, CoO and potentially $NiSO_4$ and $CoSO_4$ were present within the deposit. A nickel, cobalt and chromium depletion layer formed just below the alloy's surface, as shown in the EDS map in Figure 43. Figure 43 also shows two cracks, rich in Al, Ti and Cl.

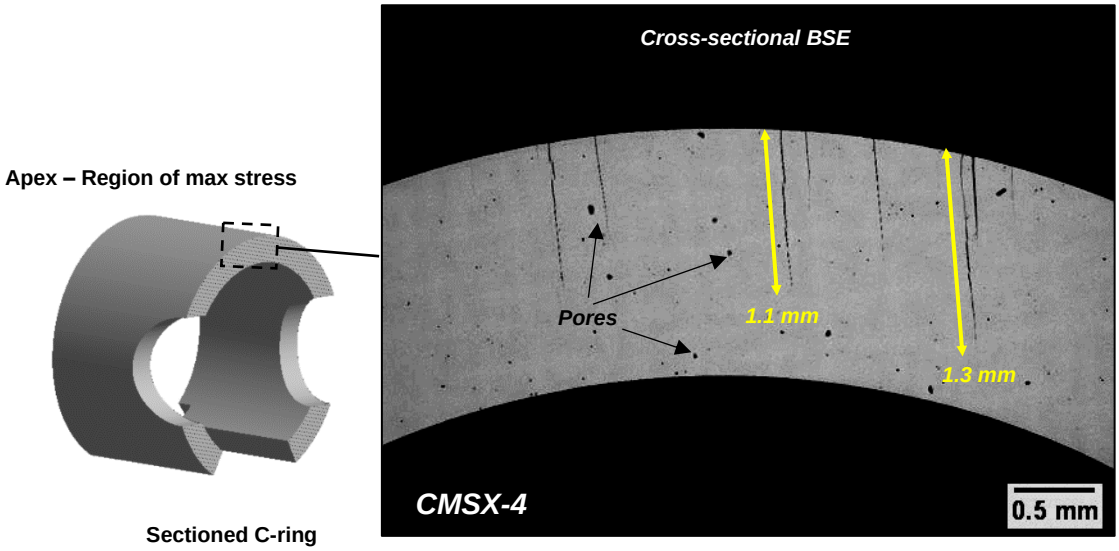


*Figure 45 - Crack depth in C-ring salted with sea salt after 400 hours of exposure*

## 4.4 Discussion

### 4.4.1 Non salted and $CaSO_4$ salted specimens

The non-salted specimen showed negligible internal attack with little external oxide formation. This can be explained given the low kinetics of oxidation [3] and sulphidation rates expected at these moderate temperatures. The thickness of the inner and external scale observed in this test is below 500 nm. This is somewhat less than the thickness of the scale observed by Evangelou [20], who performed tests in air on CMSX-4 at 550°C. In unstressed conditions, Evangelou observed approximately 500 nm of gamma prime attack and 500 nm of external oxide was formed, after 640 hours of exposure. A similar observation was made by Evangelou when an external stress of 780 MPa was applied. The observed effect of slightly reduced attack in 50 ppm $SO_2$ – air in our test, compared to the reported air exposures by Evangelou could be attributed to the strong adsorption of $SO_2/SO_3$ on active sites of the sample's surface, consequently hampering the formation of oxygen ions. As a result, the kinetics of oxidation was reduced, a consequence of the limited adsorption of oxygen-bearing species, which is in line with observations by Jardnas et al. [128].

Similar to the non-salted specimen, $CaSO_4$ treated CMSX-4 also did not undergo significant corrosion attack. From a thermodynamic point of view, this can be understood as the melting point of $CaSO_4$ is 1460°C, well above the test temperature. Based on the SEM/EDS assessment, a mixed oxide/sulphide formed in the inner scale and Ni and Cr are present within the deposit, so it is thought that reactions of $CaSO_4$ with the alloy or the scale may have occurred. Nevertheless, these reactions of $CaSO_4$ with the scale or the alloy have not led to any form of aggressive attack on the alloy.

### 4.4.2 $Na_2SO_4$

The $Na_2SO_4$ salted specimen didn't show accelerated attack, but the extent of attack was noticeably higher than for the $CaSO_4$ and non-salted specimens ( an inner scale of 1.8 µm in the $Na_2SO_4$ salted specimen compared to 0.8 µm for the $CaSO_4$ salted specimen). From a thermodynamic point of view, $Na_2SO_4$ remained in the solid phase at 550°C as the test temperature is below the melting of the eutectic $Na_2SO_4$-$NiSO_4$ (mp 671°C). This eutectic formation is typically reported to be responsible for Type II hot corrosion. Therefore, as the deposit is solid, the typical accelerated corrosion rates observed in type II hot corrosion are not expected to occur at these intermediate temperatures.

However, a mixed oxide/sulphide layer was formed in the innermost region of the scale, plus some small traces of NiO formed within the deposit on top of the oxide. A nickel depleted layer was observed to form in the alloy near surface, which suggests that accelerated outward diffusion of Ni has occurred. To some extent, this corrosion morphology looks similar to that observed by Kistler et al. [127] in previous hot corrosion studies performed at 550°C, on PWA 1484 (even though there is a significant difference in exposure time and salt concentration applied). A comparison of the scale morphology between that observed by Kissler et al. [127] and the one observed in this thesis is shown in Figure 46. A key difference in our test is an insignificant concentration of NiO was formed within the deposit, but a ~1.8 µm thick mixed sulphide/oxide was formed under the deposit. That small concentration of NiO formed within the $Na_2SO_4$ deposit may have

potentially occurred as a result of the solid-state hot corrosion mechanism proposed by Kistler et al. [127].

*Table 11 – Comparison of testing parameters used at the University of Pittsburgh and Cranfield University*

| University of Pittsburgh | Cranfield university |
|---|---|
| PWA 1484 | CMSX-4 |
| 550°C | 550°C |
| 10 ppm $SO_2$ - air | 50 ppm $SO_2$ - air |
| 6 hours | 400 hours |
| 2.5 mg/cm$^2$ $Na_2SO_4$ | 0.48 mg/cm$^2$ total $Na_2SO_4$ |

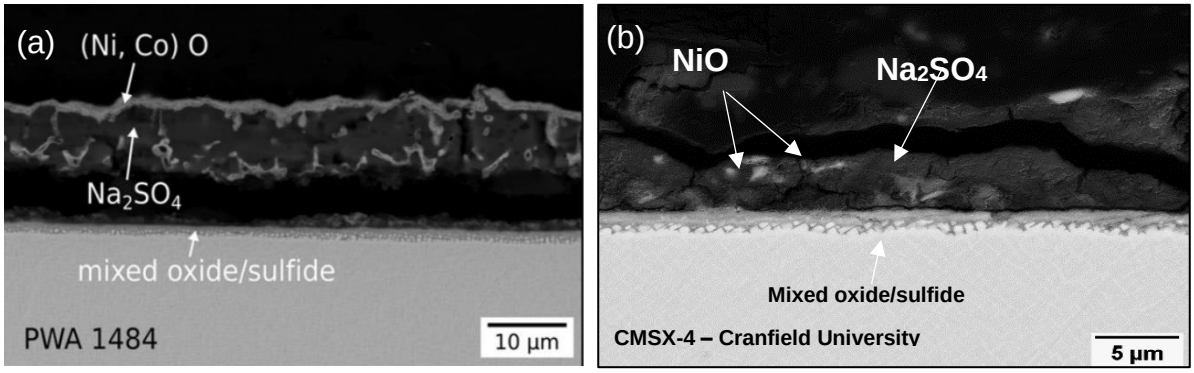


*Figure 46 – Comparison of $Na_2SO_4$ attack in (a) Pittsburgh University and (b) Cranfield University*

According to the solid-state mechanism, a nanocrystalline $Na_2Ni_2SO_5$ identified phase formed due to the reaction shown below and may have potentially led to rapid outward diffusion in Ni, which is responsible for the accelerated oxidation of Ni. The $Na_2Ni_2SO_5$ phase is reported to be a metastable phase, and its decomposition results in NiO and $Na_2SO_4$.

$$2Ni^{2+} + 4e^- + Na_2SO_4(s) + SO_3(g) \rightarrow Na_2Ni_2SO_5(s) + SO_2(g) \quad \text{Equation 44}$$

Additionally, Brooking et al. [101] investigated the effect of 80/20 mol% $Na_2SO_4/K_2SO_4$ salt attack on CMSX-4 in a sulphur-containing environment, under a sustained load and observed cracks in the substrate. However, in his study a

gaseous atmosphere of 300 pm $SO_2$ in air and 5 µg/cm$^2$/h salt load was used as opposed to the 50 ppm $SO_2$ – air and 1.2 µg/cm$^2$/h used in this study. The higher $SO_2$ concentrations in the study by Brooking et al. [101] may reflect more accurately the typical service conditions in industrial gas turbines compare to aero gas turbines. Nevertheless, this highlights the significant aggressiveness of 80/20 mol% $Na_2SO_4$/$K_2SO_4$ and also the potential effect of higher $SO_2$ concentration. Although it is outside the scope of this thesis, an interesting study that could be undertaken would be to determine what the critical concentration of $SO_2$ is required to accelerate the corrosion rates and initiate cracking with the 80/20 mol% $Na_2SO_4$/$K_2SO_4$ salt mix. Nevertheless, the $SO_2$ concentration in the lower shank region of a turbine blade is not likely to be as high as 300 ppm. This is the case because the lower shank is below the platform and is only fed with cooling air for the blade internals. So, the cooling air will contain inlet contaminants but will not contain anything from the combustion environment (which is the main source of sulphur). Ultimately, for the 50 ppm $SO_2$ concentration used in this study, it is thought that $Na_2SO_4$ does not play a significant role in the near surface weakening of the alloy in a 400-hour exposure. However, it would be interesting for future work to test if cracks initiate at exposure times longer than 400 hours using $Na_2SO_4$.

### 4.4.3 Sea salt salted specimen

The specimen salted with sea salt showed accelerated corrosion attack and cracks up to 1.03 mm deep in the highest stress region after 400 hours of exposure. The EDS maps showed accelerated oxidation of Ni, Co, Al, Ti and Cr as well as the presence of chlorine at the alloy/scale interface. Another observation from the EDS map and XRD analysis is that the alkali chlorides (NaCl, $MgCl_2$, KCl and $CaCl_2$) previously salted onto the specimen were present as sulphate and $Na_2CrO_4$ was also identified. Based on the evidence of these reactions, interactions of the salt with the sulphur-containing atmospheres and the scale must have occurred.

A phase stability diagram is a plot of thermodynamically stable phases formed by three reactants as a function of the two-gas atmosphere composition. The phase

stability diagrams shown in Figure 47, shows the most stable phases likely to form when an alkali metal is exposed to different partial pressures of a $SO_3$ – $O_2$ gas mixtures (with a constant partial pressure of $Cl_2$ of $10^{-5}$ atm). Based on those diagrams, the red mark represents the current test conditions at the scale/gas interface and shows that alkali salts are more stable as a sulphate than a chloride.

Also, although the test was conducted in 50 ppm $SO_2$ – air, there are traces of moisture present in the gas atmosphere and salt inclusions. This has been further discussed in the hot salt stress corrosion cracking (HSSCC) [83] section of the literature review, where the source of moisture when undertaking tests with NaCl salt in Ti-alloys can come from water crystallisation within NaCl salt, occluded in the oxide scale or from atmospheric moisture. Given the small amount of moisture, the sulphation of NaCl can also release HCl, as will be shown in Table 12.

Figure 48 shows thermodynamic equilibrium calculations (calculated using FactSage 8.1) that were performed to estimate the relative concentration of $Cl_2$ and HCl gas released in the sulphation process of NaCl at different concentrations of $H_2O$. The gas bottles used in this test contain a maximum concentration of 1 ppm $H_2O$ and based on the results, a concentration of 1 ppm $H_2O$ in the gas atmosphere can lead to similar mole concentrations of HCl and $Cl_2$ being formed. It has to be considered that, there will also be some $H_2O$ crystallisation in the salt, and this will eventually increase the amount of HCl that is formed relative to the amount of $Cl_2$ that is formed.

The change in Gibbs free energy formation of the sulphation reactions with and without $H_2O$ are shown in the Table 12. The reactions can occur whether NaCl is in the solid phase or in the gas phase, however reactions with NaCl in the gas phase are significantly more thermodynamically stable (vapour pressure of NaCl is $2.7 \times 10^{-7}$ atm at 550°C calculated using FactSage 8.1).

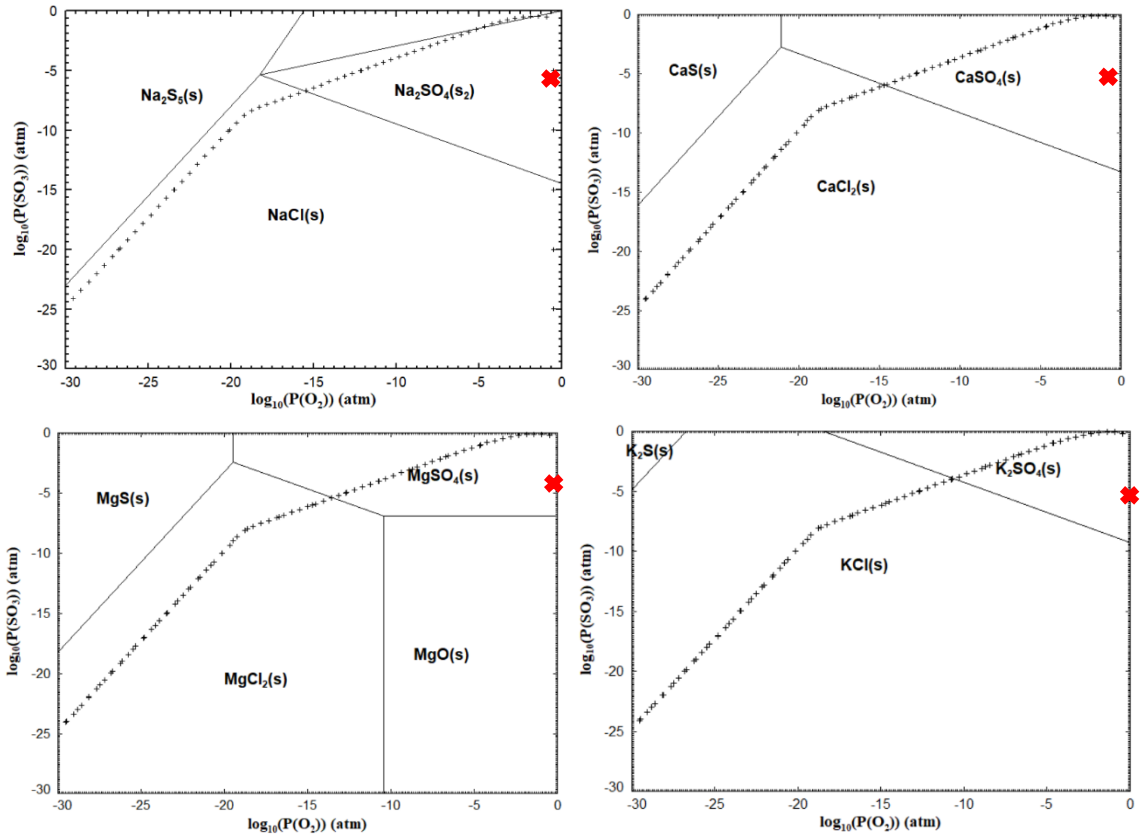


*Figure 47 – Predominance diagram of alkali metals at 550°C (FactSage 8.1)*

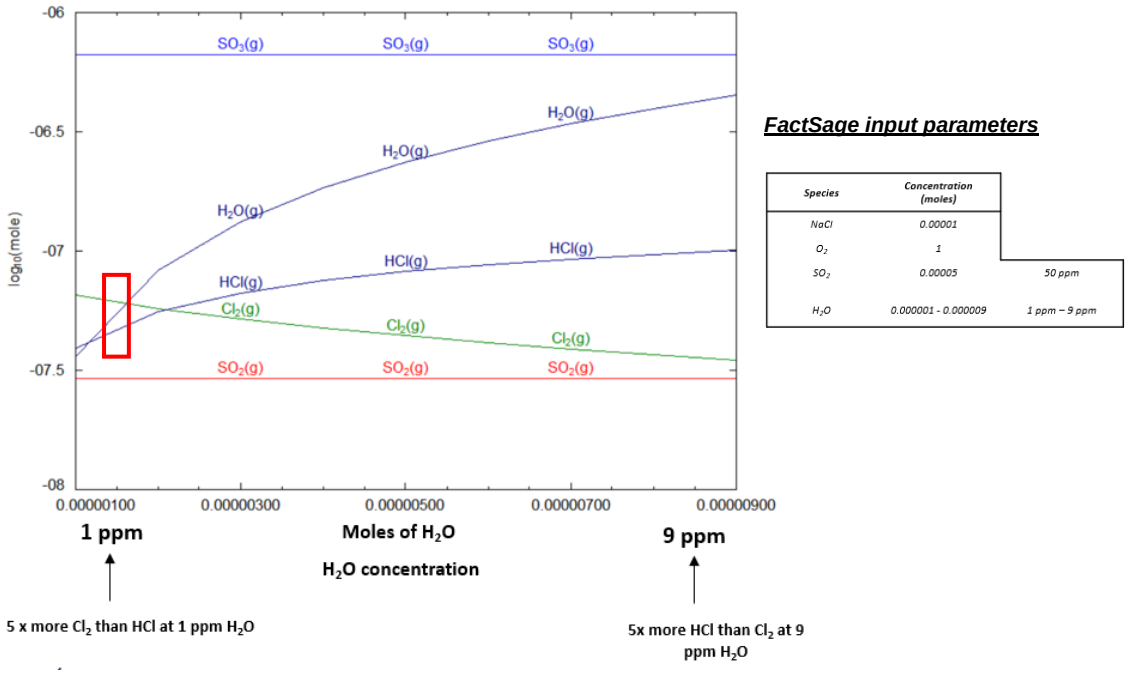


*Figure 48 – FactSage 8.1 thermochemistry equilibrium calculations to predict the mole concentration of gaseous phases formed as a function of $H_2O$ concentration.in ppm by volume (FactSage 8.1)*

*Table 12 – Change in Gibbs free energy of alkali chloride sulphation reaction (FactSage 8.1)*

| Equation | $\Delta G_{550°C}$ (J) |
|---|---|
| $2NaCl\,(g) + SO_2(\mathrm{g}) + O_2(\mathrm{g}) = Na_2SO_4(\mathrm{s}) + Cl_2(g)$ | -302252.8 |
| $2MgCl(g) + 2SO_2(\mathrm{g}) + 2O_2(\mathrm{g}) = 2\mathrm{Mg}SO_4(\mathrm{s}) + Cl_2(s)$ | -1092258.0 |
| $2KCl(g) + SO_2(\mathrm{g}) + O_2(\mathrm{g}) = K_2SO_4(\mathrm{s}) + Cl_2(g)$ | -285200.2 |
| $2CaCl(g) + 2SO_2(\mathrm{g}) + 2O_2(\mathrm{g}) = 2Ca_2SO_4(\mathrm{s}) + Cl_2(g)$ | -1291081.7 |

| Equation | $\Delta G_{500°C}$ (J) |
|---|---|
| $2NaCl(g) + SO_2(\mathrm{g}) + 0.5O_2(\mathrm{g}) + H_2O(g) = Na_2SO_4(\mathrm{s}) + 2HCl$ | -299202.2 |
| $2MgCl(g) + 2SO_2(\mathrm{g}) + 1.5O_2(\mathrm{g}) + H_2O(g) = 2MgSO_4(\mathrm{s}) + 2HCl(g)$ | -1089207.4 |
| $2KCl(g) + SO_2(\mathrm{g}) + 0.5O_2(\mathrm{g}) + H_2O(g) = K_2SO_4(\mathrm{s}) + 2HCl(g)$ | -282149.7 |
| $2CaCl(g) + 2SO_2(\mathrm{g}) + 1.5H_2O(g) = 2Ca_2SO_4(\mathrm{s}) + 2HCl(g)$ | -1288031.2 |

The formed sulphates (e.g. $Na_2SO_4$ and $MgSO_4$) are not likely to accelerate significantly the rate of corrosion attack at these moderate temperatures, but the HCl and $Cl_2$ formed in the sulphation reactions of alkali chlorides, can lead to a form of aggressive attack known an active oxidation mechanism [49]. The first stage of this form of attack is the diffusion of both HCl and $Cl_2$ through the scale (potentially through pores and defects in the scale) due to favourable gradients of vapour pressure. During the formation of corrosion products, a commensurate gradient of oxygen forms from the gas/scale interface to the alloy/scale interface. At the alloy/scale interface, there is a low partial pressure of $O_2$, which favours the formation of volatile metal chlorides due to the reaction of $Cl_2$ and HCl with alloying elements (this can be inferred from the predominance diagrams in Figure 49).

Based on the EDS map in Figure 43, $AlCl_3$, $CrCl_3$, $NiCl_2$, $CoCl_2$ and $TiCl_4$ are metal chlorides that may have formed. The change in Gibbs free energy of formation of these metal chloride reactions (calculated using FactSage 8.1) is shown in Table 13. Table 13 also highlights that, the reactions of alloying elements with HCl releases $H_2$. The implications of releasing $H_2$ at the scale/alloy interface is important as its dissociation into nascent hydrogen on the alloy surface and injection into the material may lead to hydrogen embrittlement. This will be discussed in the chapter 5.

The vapour pressure of the metal chlorides formed is also highlighted in Table 13. Based on previous reports in the field of fireside corrosion, a vapour pressure of $10^{-5}$ atm is considered significant enough to cause enhanced metal loss [49]. According to that critical vapour pressure, most metal chlorides that formed in this test, except $CrCl_3$, will vaporise away. Due to the high vapour pressure of metal

chlorides, once formed they diffuse outwards towards the gas/deposit interface and react with oxygen or $H_2O$ to form porous oxides. The reoxidation of metal chlorides releases HCl and $Cl_2$ again according to Table 14, which diffuse to the alloy/scale interface to repeat the chlorination and oxidation process.

*Table 13 - Change in Gibbs free energy of metal chloride formation (FactSage 8.1)*

| Metal chloride reaction | ΔG (J) at 550°C | Vapour pressure (atm) at 550°C | Metal chloride reaction | ΔG (J) at 550°C | Vapour pressure (atm) at 550°C |
|---|---|---|---|---|---|
| $2Al + 3Cl_2 = 2AlCl_3$ | -1087209 | $4.9x10^{-1}$ | $2Al + 6\mathrm{HCl} = 2AlCl_3 + 3H_2$ | -489448.6 | $4.9x10^{-1}$ |
| $2Ti + 3Cl_2 = 2TiCl_3$ | -1084320.3 | $1.8x10^{-3}$ | $2Ti + 6\mathrm{HCl} = 2TiCl_3 + 3H_2$ | -486559.5 | $1.8x10^{-3}$ |
| $Ti + 2Cl_2 = TiCl_4$ | -663694.9 | 1 | $2Ti + 8\mathrm{HCl} = 2TiCl_4 + 4H_2$ | -530375.5 | 1 |
| $2Cr + 3Cl_2 = 2CrCl_3$ | -713632.1 | $7.1x10^{-6}$ | $2Cr + 6\mathrm{HCl} = 2CrCl_3 + 3H_2$ | -115871.3 | $7.1x10^{-6}$ |
| $Ni + Cl_2 = NiCl_2$ | -181396 | $1.9x10^{-5}$ | $2Ni + 4\mathrm{HCl} = 2NiCl_2 + 2H_2$ | +35715.1 | $1.9x10^{-5}$ |
| $Co + Cl_2 = CoCl_2$ | -200133 | $3.7x10^{-5}$ | $2Co + 4\mathrm{HCl} = 2CoCl_2 + 2H_2$ | -1758.8 | $3.7x10^{-5}$ |
| $Co + 1.5\ Cl_2 = CoCl_3$ | -138669 | $1.2x10^{-4}$ | $2Co + 6\mathrm{HCl} = 2CoCl_3 + 3H_2$ | +320422.8 | $1.2x10^{-4}$ |

*Table 14 – Gibbs free energy change of metal chloride oxidation at 550°C (FactSage 8.1)*

| Metal chloride reaction | ΔG (J) at 550°C | Metal chloride reaction | ΔG (J) at 550°C |
|---|---|---|---|
| $NiCl_2 + 0.5\ O_2 = NiO + Cl_2$ | -57846.2 | $NiCl_2 + H_2O = NiO + 2\mathrm{HCl}$ | -54795.6 |
| $NiCl_2 + SO_2 + O_2 = NiSO_4 + Cl_2$ | -159724.4 | $NiCl_2 + H_2O + SO_2 + 0.5O_2 = NiSO_4 + 2\mathrm{HCl}$ | -156673.9 |
| $CoCl_2 + 0.5\ O_2 = CoO + Cl_2$ | -45372.6 | $CoCl_2 + H_2O = CoO + 2HCl$ | -42322.1 |
| $CoCl_2 + SO_2 + O_2 = \mathrm{Co}SO_4 + Cl_2$ | -166188.1 | $CoCl_2 + H_2O + SO_2 + 0.5O_2 = \mathrm{Co}SO_4 + 2\mathrm{HCl}$ | -163137.5 |
| $AlCl_3 + 0.75\ O_2 = 0.5\ Al_2O_3 + 1.5\ Cl_2$ | -165260.2 | $2AlCl_3 + 3\ H_2O = \ Al_2O_3 + 6\ \mathrm{HCl}$ | -321368.7 |
| $TiCl_3 + O_2 = TiO_2 + 1.5\ Cl_2$ | -295054.2 | $2TiCl_3 + 0.5O_2 + 3H_2O = 2TiO_2 + 6HCl$ | -494784.8 |
| $TiCl_4 + O_2 = TiO_2 + 2\ Cl_2$ | -130433.4 | $2TiCl_4 + 4H_2O = 2TiO_2 + 8HCl$ | -248664.7 |
| $CrCl_3 + 0.75\ O_2 = 0.5\ Cr_2O_3 + 1.5\ Cl_2$ | -98752.8 | $2CrCl_3 + 3H_2O = Cr_2O_3 + 6HCl$ | -188354.1 |

The predominance diagrams in Figure 49 show at which partial pressures of $O_2$ and $Cl_2$ the metal chlorides are formed and at which partial pressures they reoxidise. Based on these diagrams, $NiCl_2$ and $CoCl_2$ will need to encounter sufficiently higher $pO_2$ to be converted to the corresponding metal oxides, compared to $AlCl_3$, $CrCl_3$ and $TiCl_4$. Therefore, $NiCl_2$ and $CoCl_2$ reoxidise close to the deposit/gas interface, whereas $AlCl_3$, $CrCl_3$ and $TiCl_4$ oxidise near the

alloy/scale interface, which agrees well with the layers of oxides observed in Figure 43.

This mechanism of metal chloride formation, vaporisation and reoxidation involves gaseous transport, which is faster than the solid-state diffusion associated with the growth of a protective oxide scale, and may explain the accelerated oxidation rate observed in this test [11].

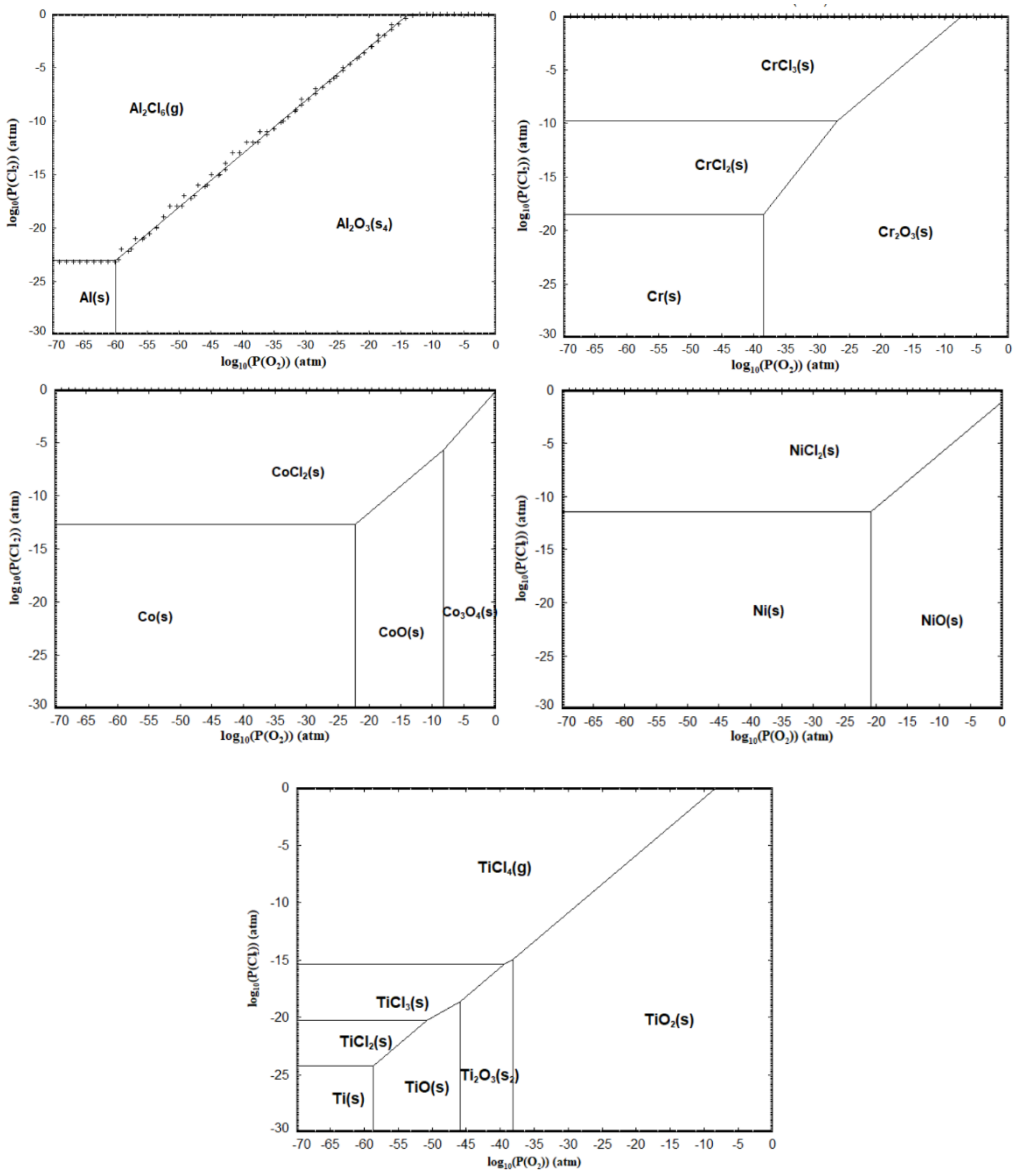


*Figure 49 – Predominance diagrams of metal chlorides at 550°C (FactSage 8.1)*

The active oxidation mechanism explains the accelerated corrosion attack caused by sea salt. The mechanism of crack formation is still under investigation,

but the depletion of alloy elements in the near surface, and the release of $H_2$ at the scale/alloy interface are important factors that may contribute to the initiation of cracks [129][130]. These potential embrittlement mechanisms will be further discussed in chapter 5.

## 4.5 Conclusions

In this chapter, the effect of no salt, $Na_2SO_4$, $CaSO_4$ and sea salt on the stress corrosion cracking behaviour of CMSX-4 in a 50 ppm $SO_2$ – air environment at 550°C has been discussed. The results showed that a non-salted specimen and a $CaSO_4$ salted specimen do not cause significant accelerated corrosion attack at these moderate temperatures and negligible near surface embrittlement occurred in 400 hours of exposure. $Na_2SO_4$ showed slightly more accelerated corrosion attack, with a corrosion morphology in line with the solid-state hot corrosion mechanism proposed by Kistler et al. [127]. However, no cracks were detected after 400 hours of exposure. It is thought that at the very low salt concentrations used and a 50 ppm $SO_2$ – air environment, $Na_2SO_4$ does not cause near surface weakening of the alloy within a 400-hour time exposure period, although some corrosion attack of the surface is observed.

Sea salt showed accelerated corrosion attack and cracks penetrating up to 1.3 mm deep into the substrate. Based on the observed results, it is implied that the sulphation of alkali chlorides and reactions of NaCl with the oxide scale released corrosive gases, such as HCl and $Cl_2$. The release of HCl and $Cl_2$ leads to an accelerated corrosion attack due to the formation, vaporisation and reoxidation of metal chlorides. There are other potential mechanisms of accelerated corrosion attack that may have occurred, such as the formation of low melting point eutectics; however, this needs to be further studied. The mechanism of crack formation is still under investigation but based on the observed results and literature on HSSCC the formation of $H_2$ at the scale/alloy interface, further injection of H into the alloy, and the dealloying of alloy elements in the near surface are potential factors that may contribute to the initiation of cracks.

# 5 Examining the effect of NaCl on the mechanisms of crack initiation at moderate temperatures

## 5.1 Introduction

The previous chapter highlighted that an external stress, sea salt and a 50 ppm $SO_2$ – air gaseous environment caused accelerated corrosion attack in CMSX-4 when exposed to a sulphur-containing environment at 550°C. The characterisation results observed showed reactions between the alkali chlorides with the oxide scale and with $SO_2/SO_3$ from the gaseous environment. Both of these mechanisms released HCl and $Cl_2$, depending on the amount of water vapour present. These results suggested the onset of an active oxidation mechanism, involving combined chlorination and oxidation mechanisms, which accelerated corrosion rates.

This chapter aims to elucidate the mechanisms of the early stages of attack and its transition to the proposed mechanism of crack initiation. To investigate this, only NaCl salt was used throughout this chapter. NaCl is the constituent with highest weight percent in sea salt and, by simplifying the salt it was possible to study the early stages of corrosion attack and the mechanisms of crack formation. Investigation of the following aspects has given a fundamental understanding of the corrosion mechanism, permitting a hypothesis regarding the mechanisms of embrittlement to be developed.

- Time resolved studies were undertaken to investigate the corrosion/oxidation process in the initial stages of the exposure in a 50 ppm $SO_2$ – air environment at 550°C.
- The effect of $SO_2/SO_3$ on the corrosion and crack initiation mechanism has been investigated by undertaking exposures in air only.
- Determination of how stress leads to an accelerated corrosion process.
    - Any changes in scale composition induced by the presence of stress?
    - Any scale damage produced by mechanical loads?

- Determination whether this crack initiation mechanism operates at 450°C.
- Ultimately, postulated mechanisms of crack initiation are discussed.

## 5.2 Methodology

C-ring specimens were used to study the stress corrosion mechanisms. The method for applying the stress and salting has been described in section 3. The salt flux was 1.2 µg/cm$^2$/hr, corresponding to 0.18 mg of salt in a 50-hour exposure period. The kappa angle of the specimens used throughout this study varied from 32.5 to 40°. This variation in kappa angle between samples is due the fact that the kappa angle cannot be controlled during the casting of the bars; nevertheless, the differences in stress between the samples did not exceed 27 MPa. At these kappa angles, the maximum stress along the C-ring is slightly below the apex of the specimen. For illustration purposes, the stress distribution for the 36° kappa angle specimens is Figure 50.

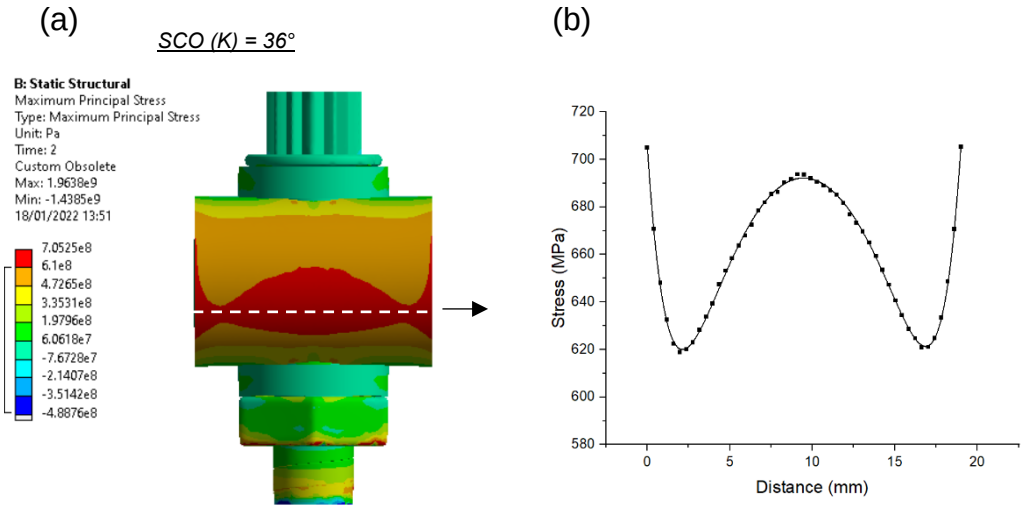


*Figure 50 – (a) Stress distribution of a C-ring with a kappa angle of 36° and with an applied displacement of 0.44 mm, (b) Stress distribution along the high stress region (along the white dashed line)*

As highlighted in Table 15, a furnace with the capability of rapid heating was used for the low exposure times (1 min, 5 min, 10 min, 15 min). One sample was exposed for 1 minute, 5 minutes and 10 minutes to detect at which exposure time cracks formed. The rest of the exposure times shown in Table 15 are from separate samples.

The reason for using this rig was that it ramps up the temperature from 22°C - 550°C in approximately 3-4 minutes. Prior to these exposures, the $SO_2$ containing gas supply was left to stabilise for 15 minutes, and then the temperature was raised.

The apex and lower edges of the C-ring were salted to investigate the effect of high stress and low stress on the thickness of the scale formed (as shown in Figure 51).

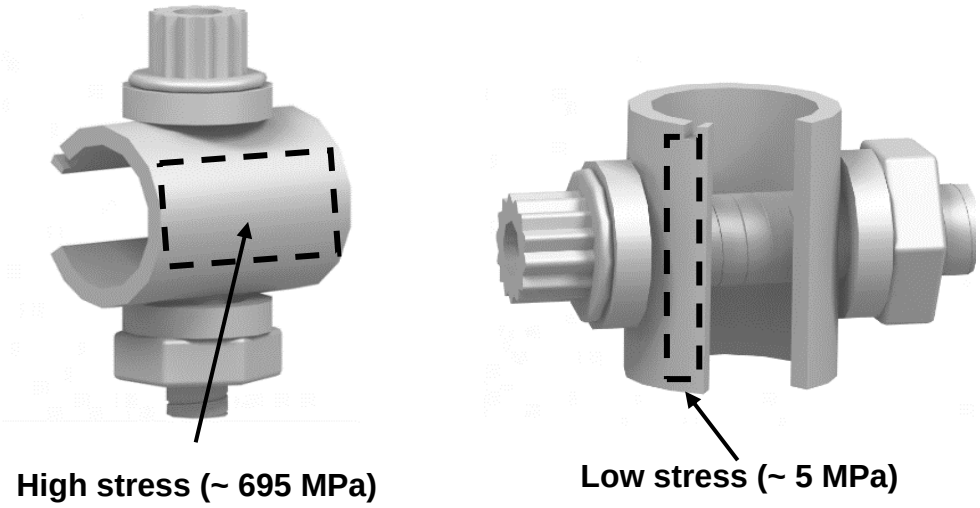


*Figure 51 – Salted regions of the C-ring to compare the effect of high stress and low stress on corrosion behaviour*

*Table 15 – Testing parameter used in C-ring specimens*

| Alloy | Exposure time | Displacement (mm) | Stress at apex (MPa) | Kappa angle (°) | Gas atmosphere | Test temperature (°C) | Equipment |
|---|---|---|---|---|---|---|---|
| CMSX-4 – same | 1 min | 0.44 | 694 | 36 | 50 ppm $SO_2$ - Air | 550 | PD |
| CMSX-4 – same | 5 min | - | 694 | 36 | 50 ppm $SO_2$ - Air | 550 | PD |
| CMSX-4 - same | 10 min | - | 694 | 36 | 50 ppm $SO_2$ - Air | 550 | PD |
| CMSX-4 | 15 min | 0.44 | 694 | 36 | 50 ppm $SO_2$ - Air | 550 | PD |
| CMSX-4 | 2 hours | 0.44 | 694 | 36 | 50 ppm $SO_2$ - Air | 550 | Horizontal furnace |
| CMSX-4 | 50 hours | 0.44 | 679 | 40 | 50 ppm $SO_2$ - Air | 550 | Horizontal furnace |
| CMSX-4 | 400 hours | 0.44 | 679 | 40 | 50 ppm $SO_2$ - Air | 550 | Horizontal furnace |
| CMSX-4 | 50 hours | 0.44 | 705 | 32.5 | 50 ppm $SO_2$ - Air | 450 | Horizontal furnace |
| CMSX-4 | 50 hours | 0.44 | 705 | 32.5 | Air | 550 | Horizontal furnace |

## 5.3 Results

### 5.3.1 CMSX-4 C-ring with NaCl deposit in a 50 ppm $SO_2$ – Air environment

Figure 52 shows top surface optical images of the C-rings after different exposure times. The stress bar on the left-hand side shows the calculated stress across the middle of the C-ring going from the top washer to the bottom washer.

The locations where cracks were visibly observed on the optical microscope have been labelled with a cross mark. ImageJ was used to zoom into regions of interest within the optical image. It was anticipated that some thin cracks may not have been identified but this method was able to give an overall idea of crack initiation locations within the C-ring at different exposure times.

Based on the cross marks, highlighted in Figure 52, no detectable cracks were observed after 5 minutes of exposure, but several cracks were observed after 10 minutes of exposure in the highly stressed region of the C-ring. With an increase in exposure time, cracks started initiating in regions of lower stress as shown in the 15 minute and 2-hour exposed specimens. After 2 hours cracks initiated in regions where the stress magnitude was approximately 480 MPa and this was the threshold critical stress to initiate cracks within a 50-hour period.

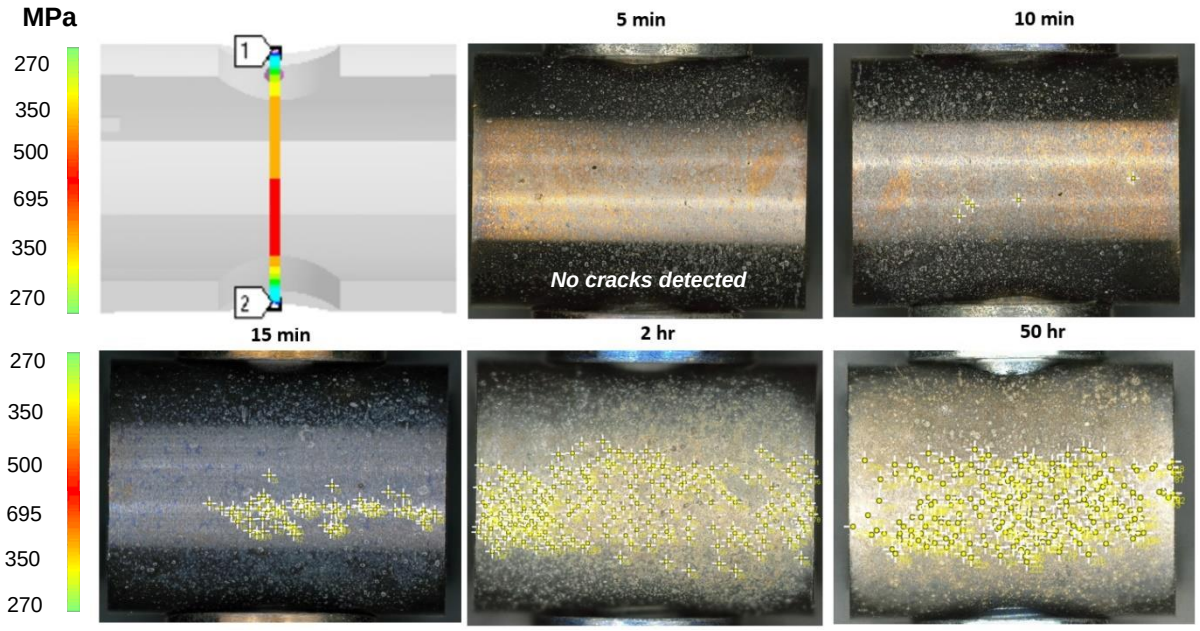


*Figure 52 – Optical microscope images of the salted C-ring after different exposure times*

Figure 53 shows top surface SEM images of the C-ring before the exposure and after 1 min, 5 min and 10 min of exposure in the high-stressed region. The regions were salt was applied, showed a halo region surrounding the salt ridge. Regions of high salt density formed a larger halo surrounding the ridges and crack coalescence is commonly observed in these regions. Figure 53 (c) and Figure 54 shows dark spots appearing on the outline of the halo, and associate with Cr and Cl, but these spots were only present in certain regions of the C-ring's surface.

The EDS maps in Figure 54 show a mix of $Na_2SO_4$ and NaCl within the salt ridge and the halo surrounding it after 10 minutes of exposure. It is thought that as the NaCl salt diffuses along the surface it reacts with the sulphur-containing gas to form $Na_2SO_4$ and, as a result of the reaction, HCl and $Cl_2$ gas are released as shown in the reactions from Table 12.

The cracks typically initiate below the ridge of the salt particle and propagate in a direction perpendicular to the stress field. As observed and reported by Chevrot [83], the oxygen activity is reduced below the NaCl salt ridge, while the $H_2O$ activity was increased in this region. Hence, when metal chlorides diffuse outwards, they are likely to react with $H_2O$, releasing HCl. Ultimately, below the

salt ridge is an area where large amounts of hydrogen are likely to be injected into the alloy in a rapid manner, potentially causing embrittlement. Interestingly, no cracks in CMSX-4 are observed to initiate within the halo (they are only observed to form below the ridge of the salt), so it is thought that the amount of H injected into the alloy is not sufficient to cause cracking, with the amount injected in a rapid manner not as significant as below the ridge. Cracks that initiate below a salt ridge and near the edge of the halo, arrested at the outer boundary of the halo as shown in Figure 55.

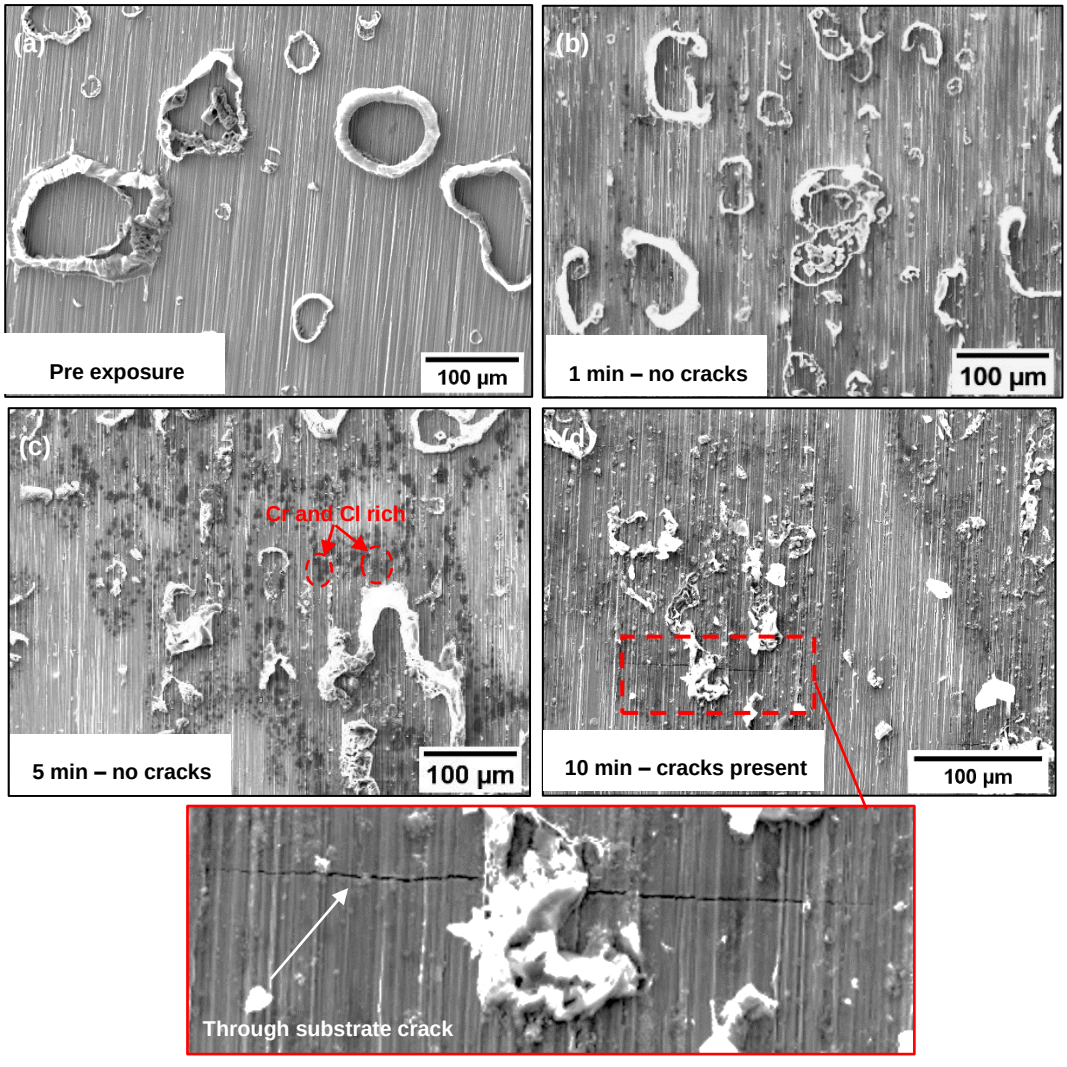


*Figure 53 - SE images of the top surface of salted C-ring in the high stressed region exposed for (a) pre-exposure (b) 1 minute, (c) 5 minutes and (d) 10 minutes in 50 ppm $SO_2$ and (e) through substrate crack*

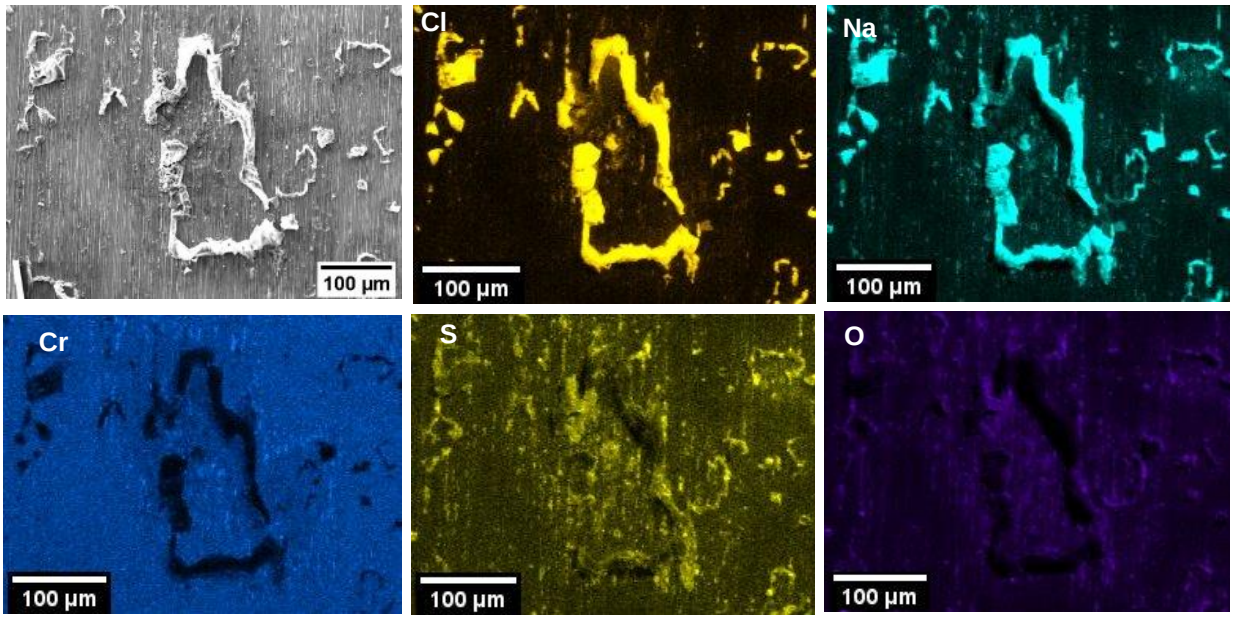


*Figure 54 - EDS map of the high stressed region of salted C-ring exposed for 10 minutes in 50 ppm $SO_2$*

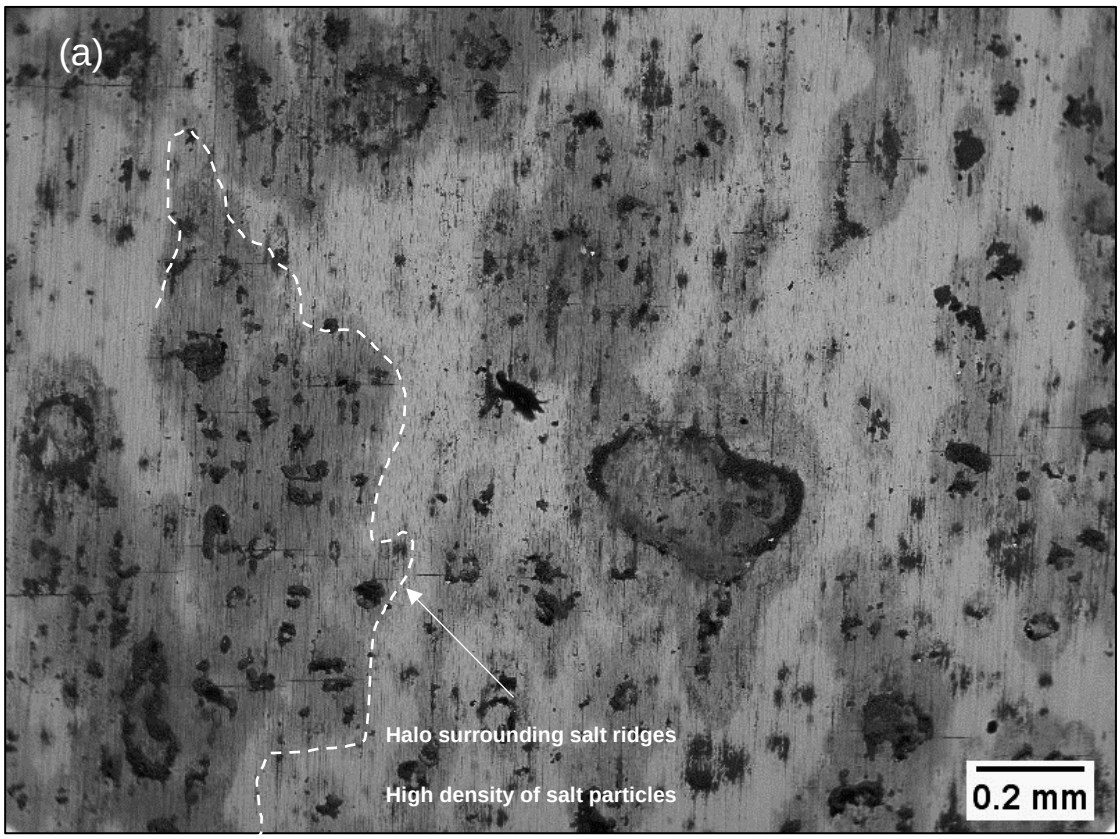


Part of Fig 54

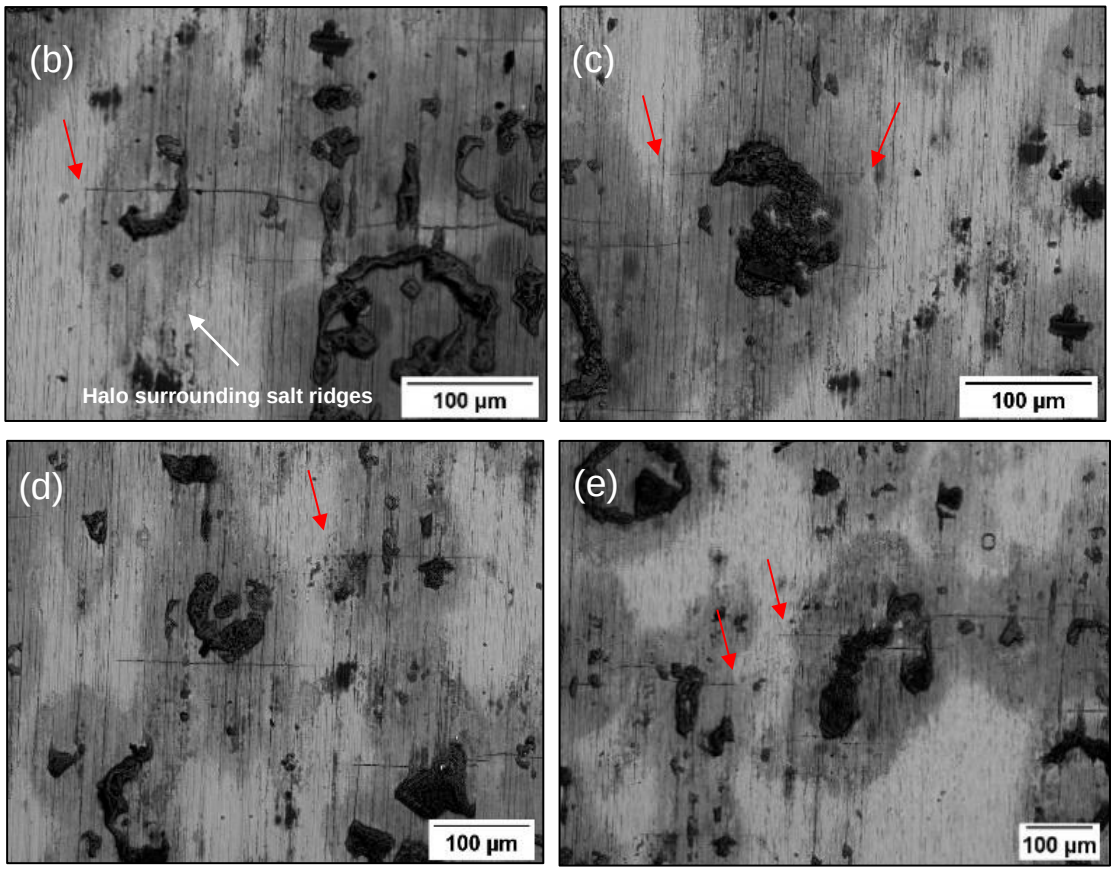


*Figure 55 – BSE images of the top surface of salted C-ring exposed for 15 minutes in 50 ppm $SO_2$*

After 2 hours of exposure, lamellas were extracted across the ridge of a salt particle to study the chemistry of the near surface and morphology of the oxide scale formed, as shown in Figure 56.

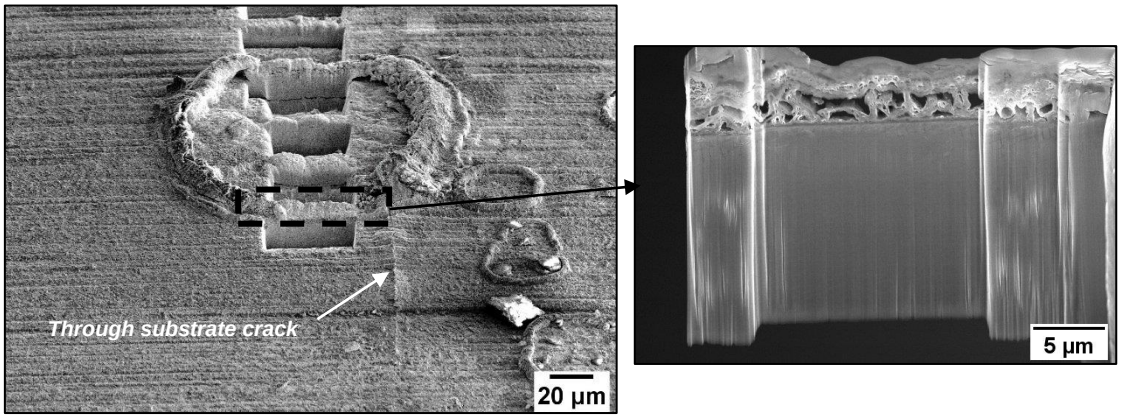


*Figure 56 – Lamella extraction through the ridge of a salt particle*

Figure 57 and Figure 58 shows the TEM image of the prepared lamella. The d spacing of the selective area diffraction pattern within the deposit matched with NiO. Cl, S and O preferentially attacked the gamma matrix, which extends approximately 1 micron into the surface after 2 hours of exposure. Within the deposit, there is an association of Na with S and not with Cl, so it is thought that after 2 hours of exposure most of the NaCl that was initially deposited has reacted with the sulphur-containing environment to form $Na_2SO_4$. Ni and Co are depleted from both the γ and the γ' and are present as a porous oxide and, potentially as $NiSO_4$ and $CoSO_4$ within the deposit. The presence of $NiSO_4$ and $CoSO_4$ within the deposit can be understood based on their stabilities at the $p(SO_2)$ and $p(O_2)$ present at the salt/gas interface (which will be further illustrated in the predominance diagrams of Figure 73). In the near surface, Al associates with Cl and O along the gamma channels. Chromium and titanium are also depleted from the gamma channels and are present as an oxide at the alloy/scale interface, as shown in Figure 58.

The EDS map shows that Ni, Co, Al, Cr, Ti and Ta are involved in this active oxidation mechanism, where the attack by $Cl_2$ and HCl lead to the outward diffusion of these elements as metal chlorides. Due to their high vapour pressure (as shown in Figure 12), it is thought that the outward diffusion is by gaseous transport.

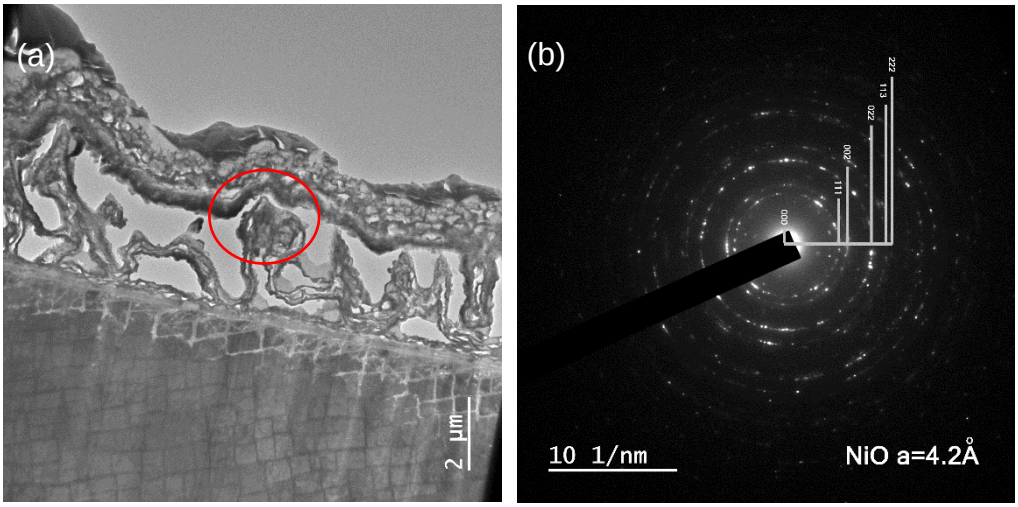


*Figure 57 – (a) TEM image of cross-section through salt particle and (b) selective area diffraction pattern of the deposit.*

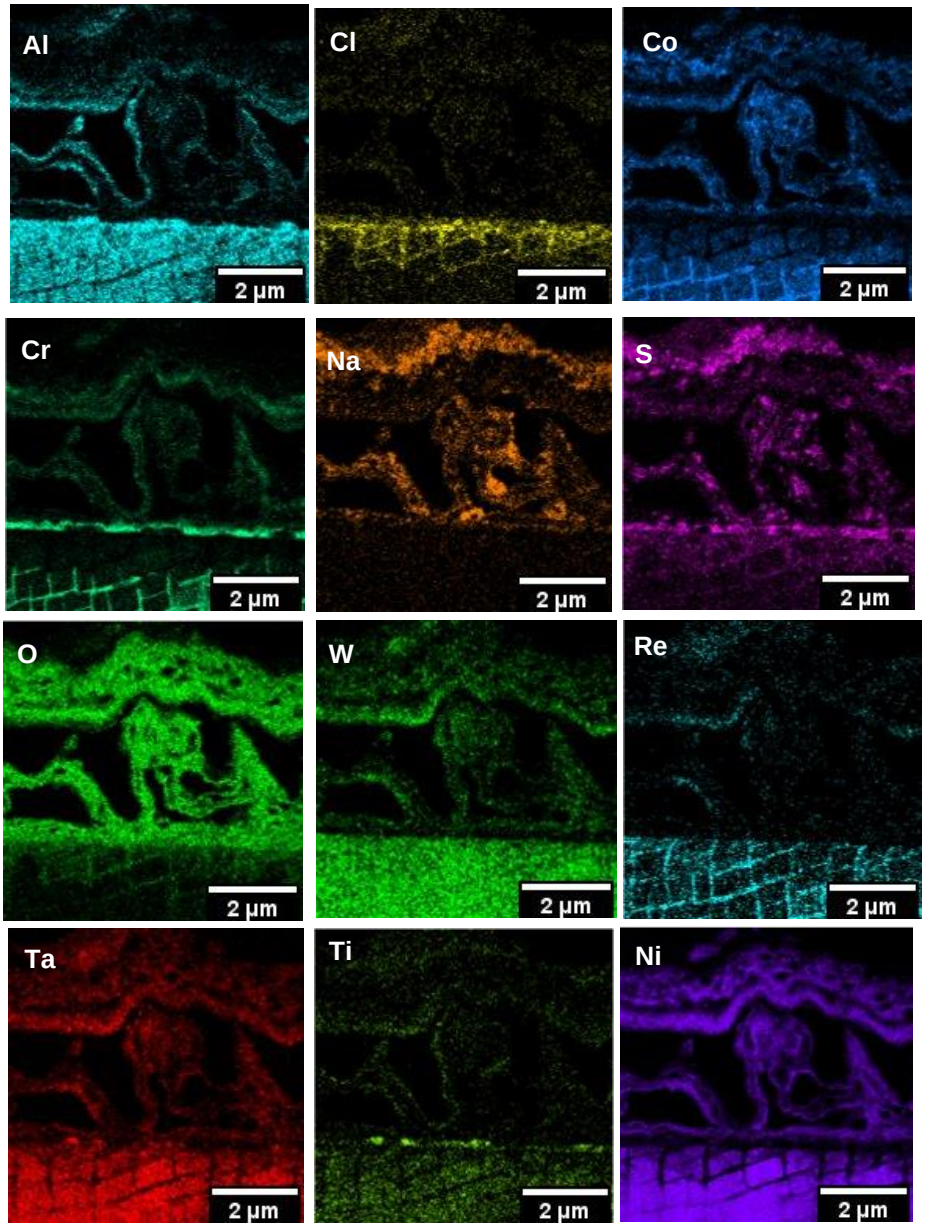


*Figure 58 – TEM elemental map of C-ring exposed for 2 hours in a 50 ppm $SO_2$ – air gaseous atmosphere at 550°C*

Further examinations of the near surface at higher magnifications showed an arrangement of layered structures formed in an orthogonal array. These features were mainly observed in the γ matrix (as shown in Figure 59), but, in some instances, were also present in the γ' phase. Based on the EDS map in Figure 60, these arrays are rich in W and S (likely to be $WS_2$ based on phase stability diagrams that will be shown in Figure 73). Overall, it seems that during the initial stages of the corrosion process, the gamma matrix is being preferentially

attacked. HCl is reacting with elements, such as Ni, Co, Al, Ti and Cr forming volatile metal chlorides, which are then diffusing outwards and oxidising, forming porous oxides. The predominance diagrams in Figure 73 provides the partial pressures of $O_2$ in which metal chlorides oxidise, and they show that $AlCl_3$, $TiCl_4$ and $CrCl_3$ oxidise near the alloy/scale interface and that $NiCl_2$ and $CoCl_2$ oxidise near the deposit/gas interface. W, however, is preferentially attacked by sulphur.

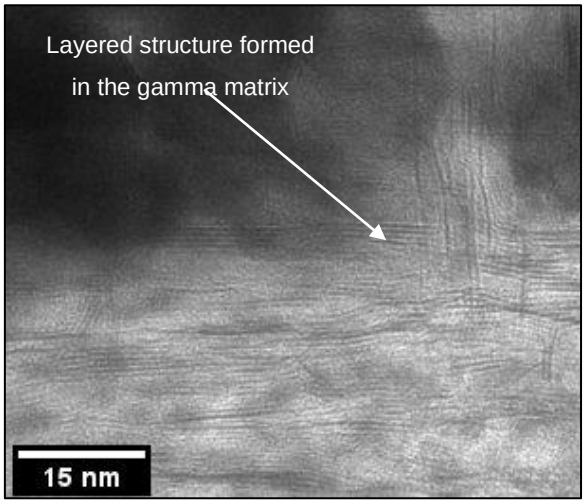


*Figure 59 – Layered structure formed in the near surface of CMSX-4 after 2 hours of exposure in a 50 ppm $SO_2$ – air environment.*

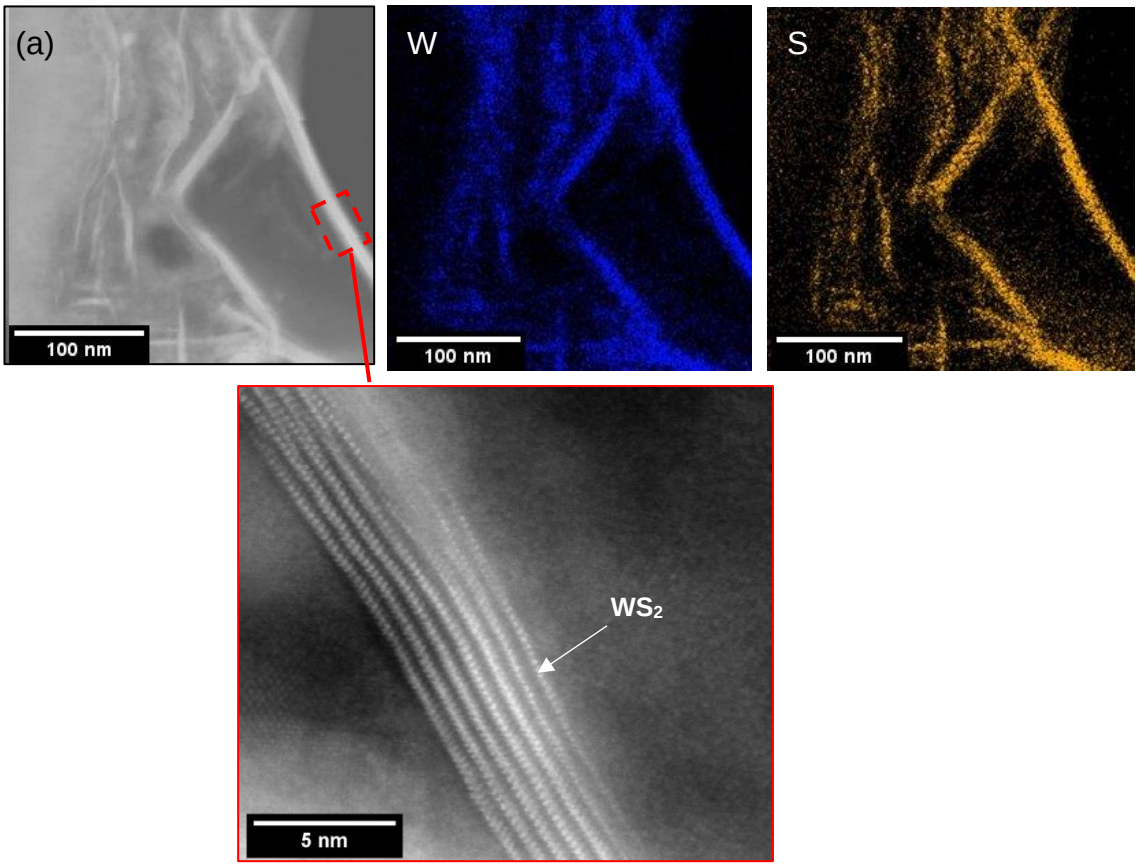


*Figure 60 – High resolution STEM image showing (a) EDS map of the layered structures formed and (b) atomic resolution image of the W and S rich layered structure*

### 5.3.2 Observations at 50 hours of exposure

Figure 61 shows secondary electron images of the apex region of the C-ring after 50 hours of exposure and illustrates that the halo surrounding the salt particles has developed a porous scale morphology, whereas regions further away have a denser morphology. Spallation typically occurs in regions where salt was applied. The porous scale and spallation sites that form may act as fast diffusion paths for the ingress of S, O and Cl, potentially increasing the rate of corrosion attack in local regions where salt was deposited.

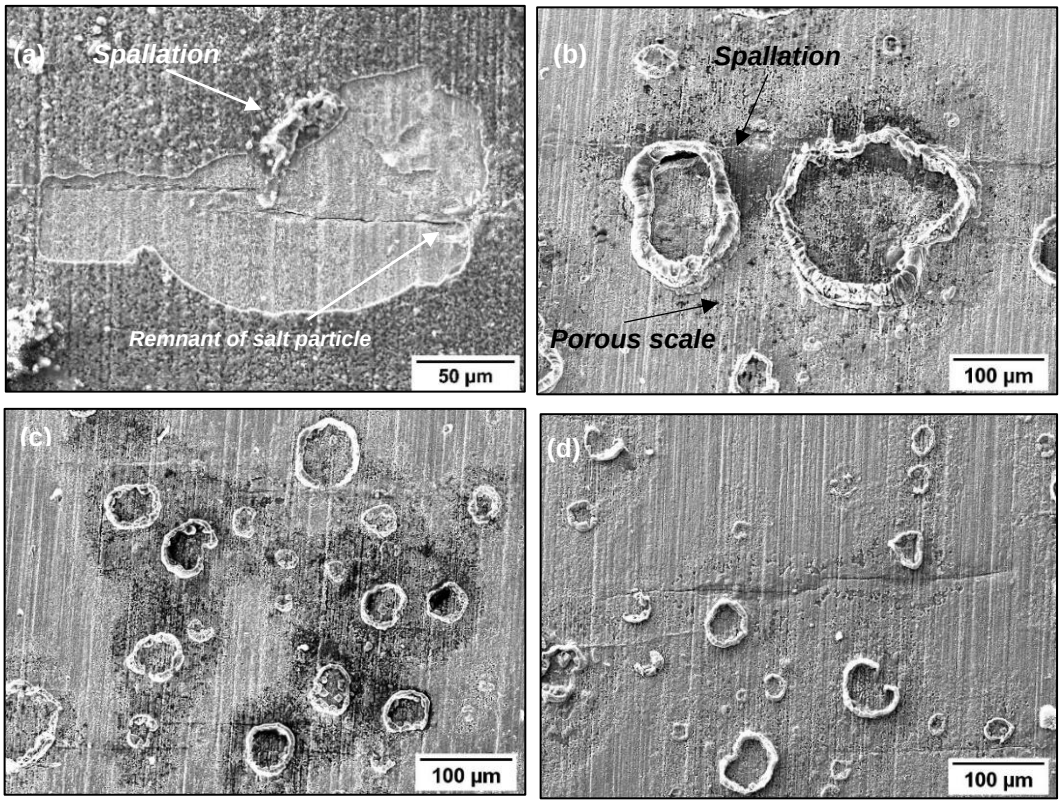


*Figure 61 - SE images of the top surface of salted C-ring exposed for 50 hours in 50 ppm $SO_2$*

Based on the EDS maps and the XRD analysis shown in Figure 62 and Figure 63, within the salt deposit an external scale rich in NiO, $NiSO_4$, CoO and $CoSO_4$ was observed along with $Na_2SO_4$ salt. The inner scale was rich in Cl, Al, Cr, Ti and a subsurface region depleted of Ni and Co was observed. A region of approximately 3 µm of internal attack was observed, where both the γ and the γ' phases are attacked. Overall, the corrosion attack was highly localised within the halo region surrounding each salt ridge.

As described in the previous chapter, it is thought that the sulphation of NaCl leads to the release and inward diffusion of both HCl and $Cl_2$. As chlorine reaches the alloy/scale interface the formation of metal chlorides occurs given the low partial pressures of oxygen in that region. Within the halo (and away from the salt ridge), the formation and outward diffusion of $NiCl_2$ and $CoCl_2$ leave holes in the scale, as similarly reported in [131], and this explains the porous morphology of the scale surrounding the salt ridge. Regions away from the halo formed more protective oxide and did not show concentrations of NiO, CoO or metal chloride

formation at the alloy/scale interface. This highlights that the attack is highly localised around the halo region where NaCl salt was deposited.

Figure 62 and Figure 63 also show evidence of Al, Ti and Cr chlorination in regions where cracks are present. The potential effects of this on the crack propagation will be further discussed in the next section.

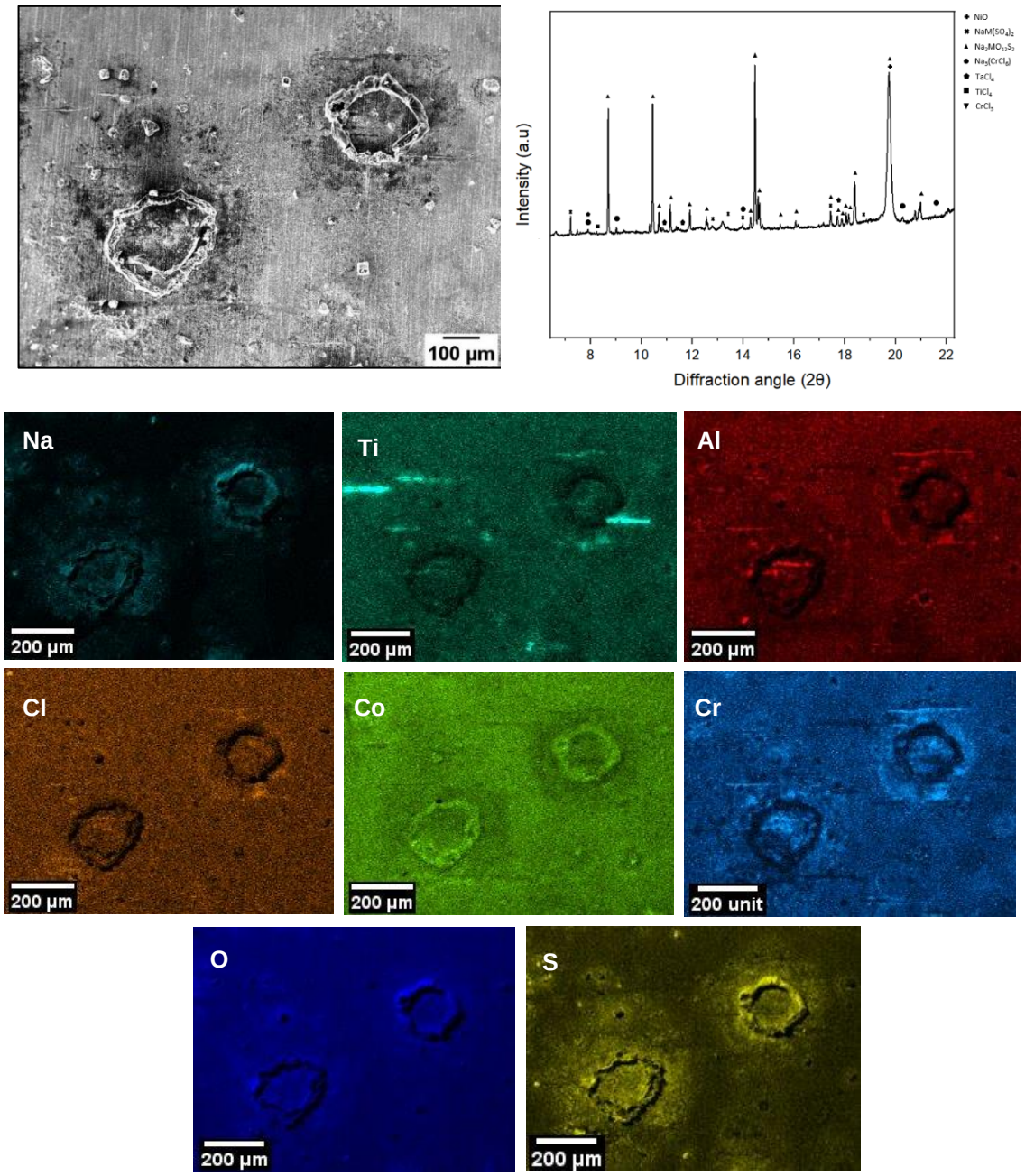


*Figure 62 – EDS map of the top surface of salted C-ring exposed for 50 hours in 50 ppm $SO_2$ - Air*

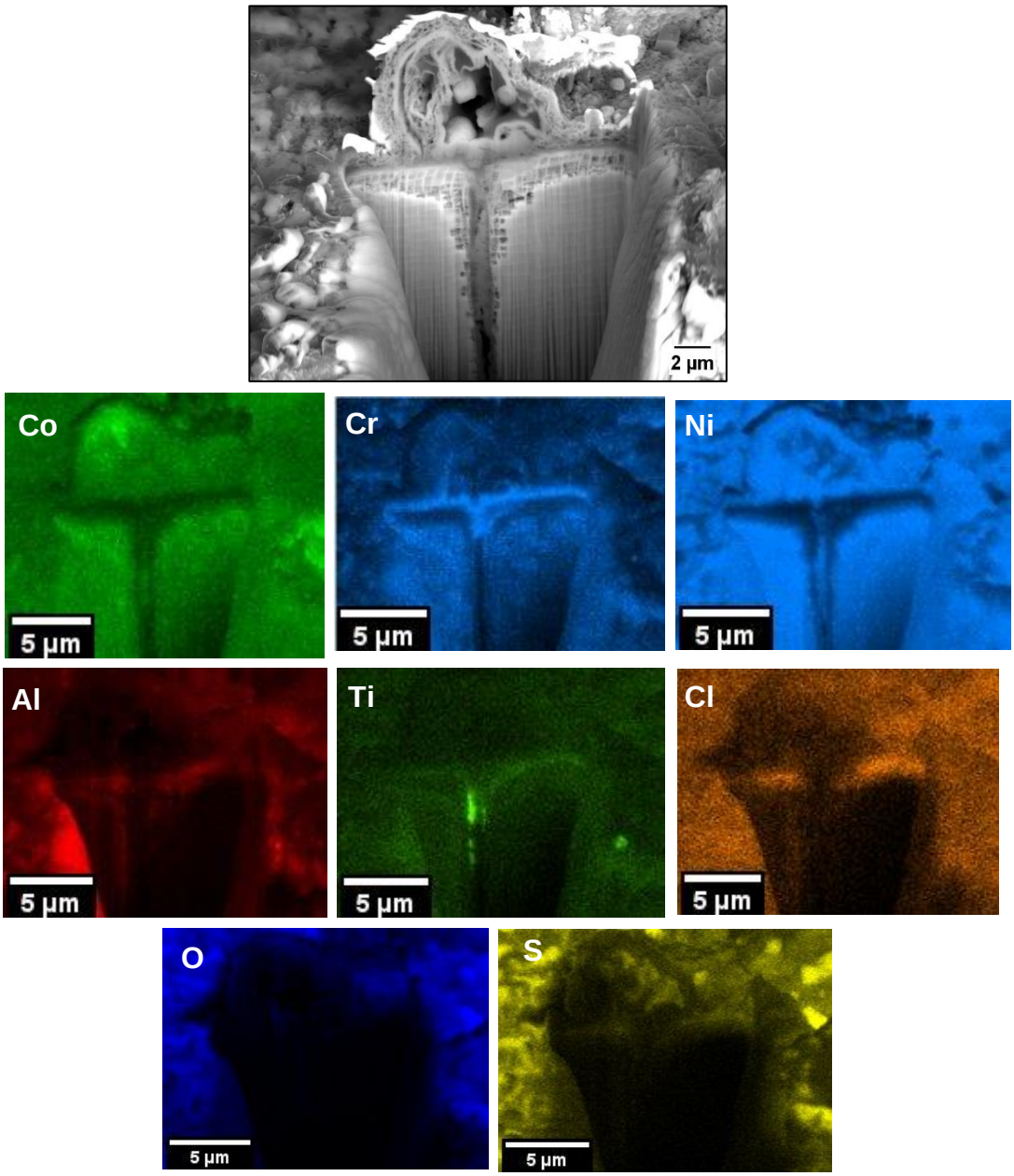


*Figure 63 – EDS map of cross-section through a NaCl salt deposit after 50 hours of exposure*

### 5.3.3 Effects of stress on scale thickness

To examine the effect of stress on the corrosion attack of the alloy, the external and internal thickness of the scale was compared in the apex region of the C-ring (high stress ~ 679 MPa) and the edge region of the C-ring (low stress ~ 10 MPa). Figure 64 shows that the thickness of both, the external and internal scale in stressed and unstressed conditions is not significantly different. No difference in scale composition was observed in both regions and they both showed

tendencies to spall and crack. Therefore, it is thought that stresses below the elastic limit do not lead to an accelerated rate of corrosion attack.

Similar observations were reported by Evangelou [3], in which oxidation tests in air were carried out on CMSX-4 in stressed and unstressed conditions at 550°C. Evangelou observed that the thickness of the scale formed when the applied stress was in the elastic regime was comparable to the thickness of the sample in unloaded conditions. However, when sufficient load to induce plastic deformation was applied, an increase in scale thickness was observed compared to the unloaded sample. It was postulated that defects resulting from the induced plastic deformation provide open routes for enhanced oxygen diffusion into the substrate material. For instance, cracking, increased dislocation densities and slip band formation near the surface act as very fast diffusion paths and may have enhanced the outward diffusion of elements and the ingress of oxygen. Also, the fact that sufficient load to induce plastic deformation in the substrate may lead to the brittle failure of the oxide scale, which further enhances the extent of corrosion attack. Nevertheless, the stress level applied in this thesis is insufficient to induce plastic deformation, so enhanced corrosion attack is not observed in the highly stressed region compared to the low stressed region. Although it is outside the scope of this work, future testing could study the effect of external loads sufficient to induce plastic deformation on the resulting thickness of the scale compared to an unloaded sample.

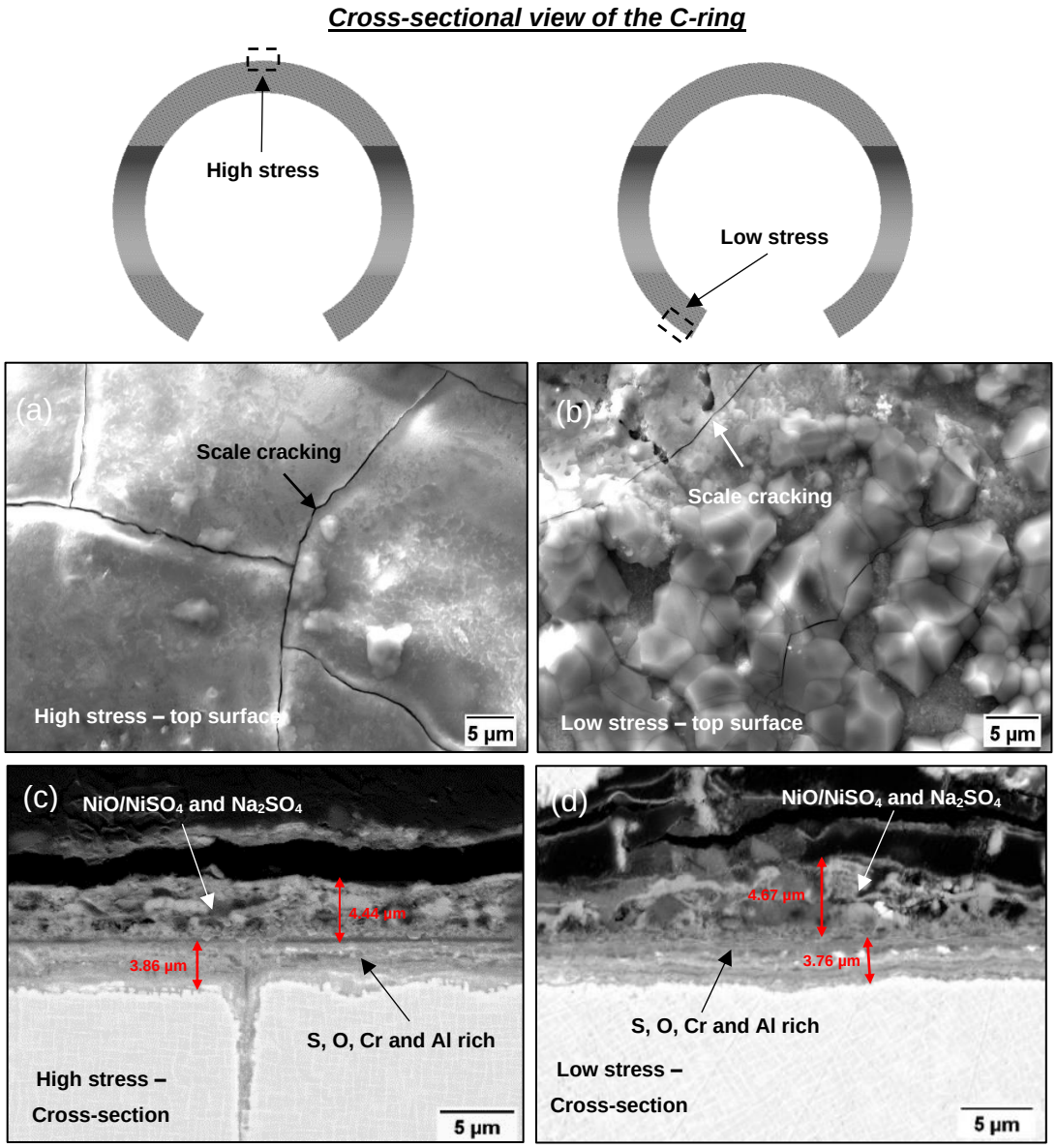


*Figure 64 – Top surface and cross-sectional BSE images of C-ring exposed for 400 hours (a) top surface high stress region, (b) top surface low stress region, (c) cross-section high stress region, (d) cross-section low stress region*

### 5.3.4 Crack depth measurements

For crack depth measurements, three C-ring specimens (exposed for 15 min, 2 hours and 50 hours) were sectioned through the central region of the apex. SEM was used to measure the location of cracks with respect to the apex and their corresponding depth. The location of the cracks on the outer surface of the sectioned C-ring was correlated to their corresponding location in the FEA model

to assign a stress level. The specimens have a secondary crystallographic orientation between 35 and 40°, hence there is no significant difference in stress level around the circumference of the C-ring between the different specimens (as highlighted in Table 15.

Figure 65 shows that between 450 and 550 MPa there are a few cracks that penetrate up to 50 µm into the alloy. However, beyond the threshold stress 550-600 MPa the crack depth significantly increases.

Figure 65 also highlights that there is no significant difference in maximum crack depth between the 2 hour and the 50-hour exposed specimen (in both cases the maximum crack depth is approximately 250 µm). This suggests that most of the initiation and crack growth in a sustained load regime occurs within the first two hours. There are two theories that may explain this observation. On one hand, it is interesting to note that, according to the EDS map in Figure 58, most of the NaCl had reacted to form $Na_2SO_4$ after two hours of exposure, which is not as corrosive and also supresses further formation of $Cl_2$ and HCl. One could argue that HCl could still be formed due to the oxidation of metal chlorides in a cyclic loop. However, some of this HCl may diffuse away from the gas atmosphere, so with time this will not lead to further injection of H into the alloy. Nevertheless, whether the suppression of $Cl_2$ and HCl formation, and therefore the set of reactions that lead to rapid injection of H, is the reason why crack propagation is significantly reduced after 2 hours of exposure is an aspect which should be further studied.

On the other hand, it may also be argued that the load or stress drops off after 2 hours, due to the presence of multiple cracks, and hence, crack propagation is significantly reduced after 2 hours of exposure due to this stress drop (and the crack depth does not increase further than approximately 250 µm within one salt cycle). However, in chapter 4, it was shown that the sample salted with sea salt (which had eight resalts applied) had cracks up to 1.3 mm in depth. This may suggest that resalting leads to further crack propagation and that the “stress drop off” is not significant enough to reduce this crack propagation when salt is

reapplied. Potentially, cracks may grow in “parabolic” jumps when salt is applied. Nevertheless, further work is needed to support this statement.

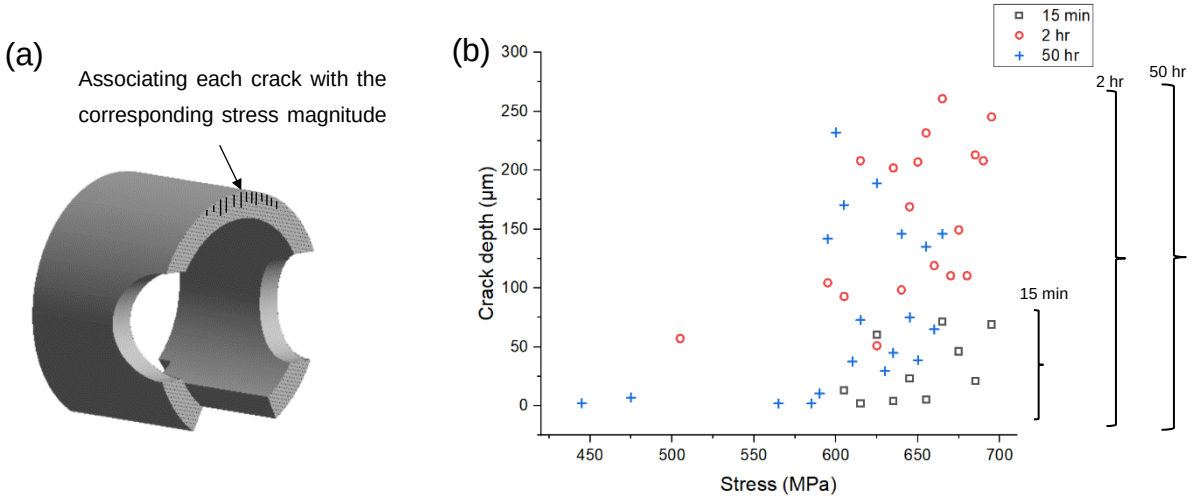


*Figure 65 – Crack depth vs stress at different exposure times*

### 5.3.5 Effect of air exposure at 550°C on stress corrosion cracking of CMSX-4

To separate the effect of sulphur, a test in air was undertaken. Figure 66 shows a CMSX-4 C-ring specimen exposed for a 50-hour period with a NaCl deposit in air on the left and one in 50ppm $SO_2$ – air on the right-hand side. After the 50-hour air exposure, an optical and SEM assessment showed no visible cracks.

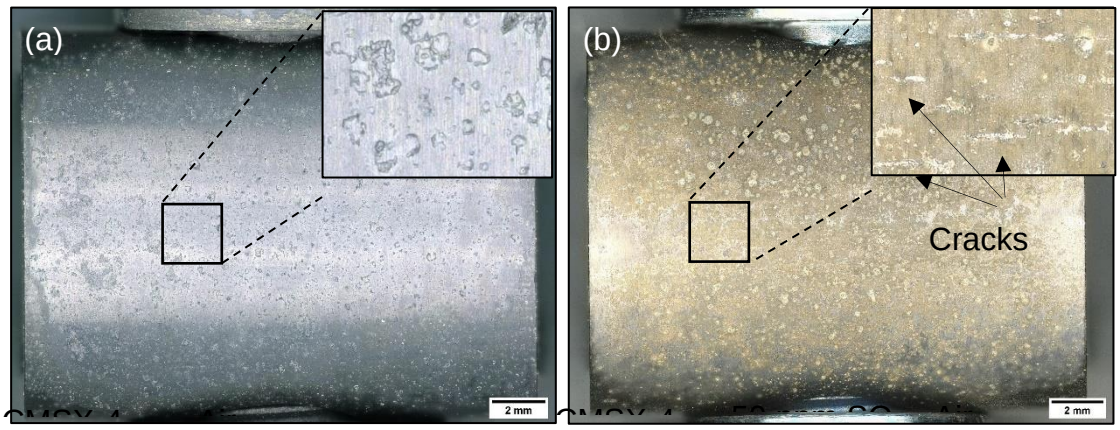


*Figure 66 – Optical image of salted C-ring exposed for 50 hours in (a) Air, and (b) 50 ppm $SO_2$ - Air*

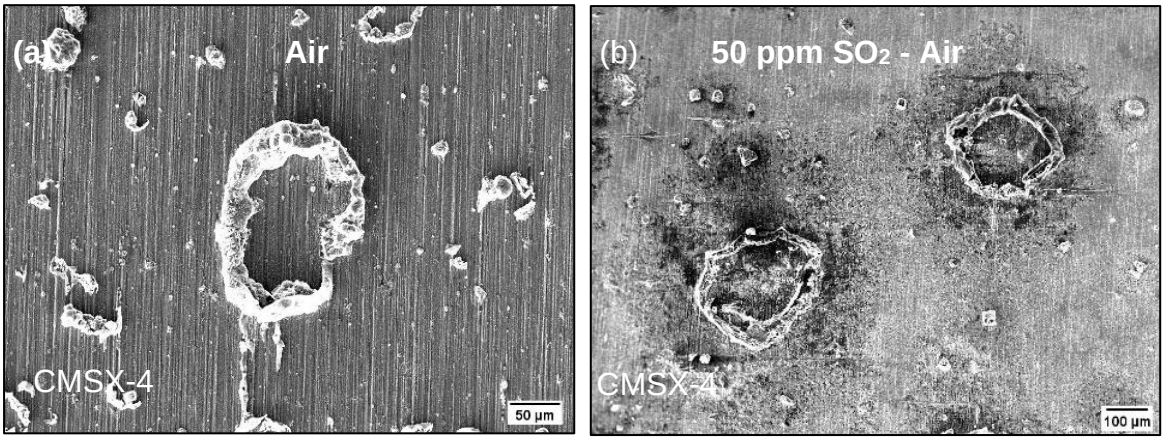


*Figure 67 – SE image of salted C-ring exposed for 50 hours in (a) Air, and (b) 50 ppm $SO_2$ - Air*

Based on Figure 68 and Figure 69, no significant outward transport of alloy elements is observed in air. However, after unloading and storing the specimens in a desiccator for several days significant spallation was observed. The lateral transport of the salt, and the porous scale microstructure observed in the sulphur containing environment is not present in the test undertaken in air. Also, no evidence of chlorination in regions away from the salt ridge is observed

Based on the EDS map in Figure 68 and Figure 69, CoO and NiO formed within the salt deposit. Chlorine and sodium are relatively absent (which is further confirmed by the cross-sectional analysis).

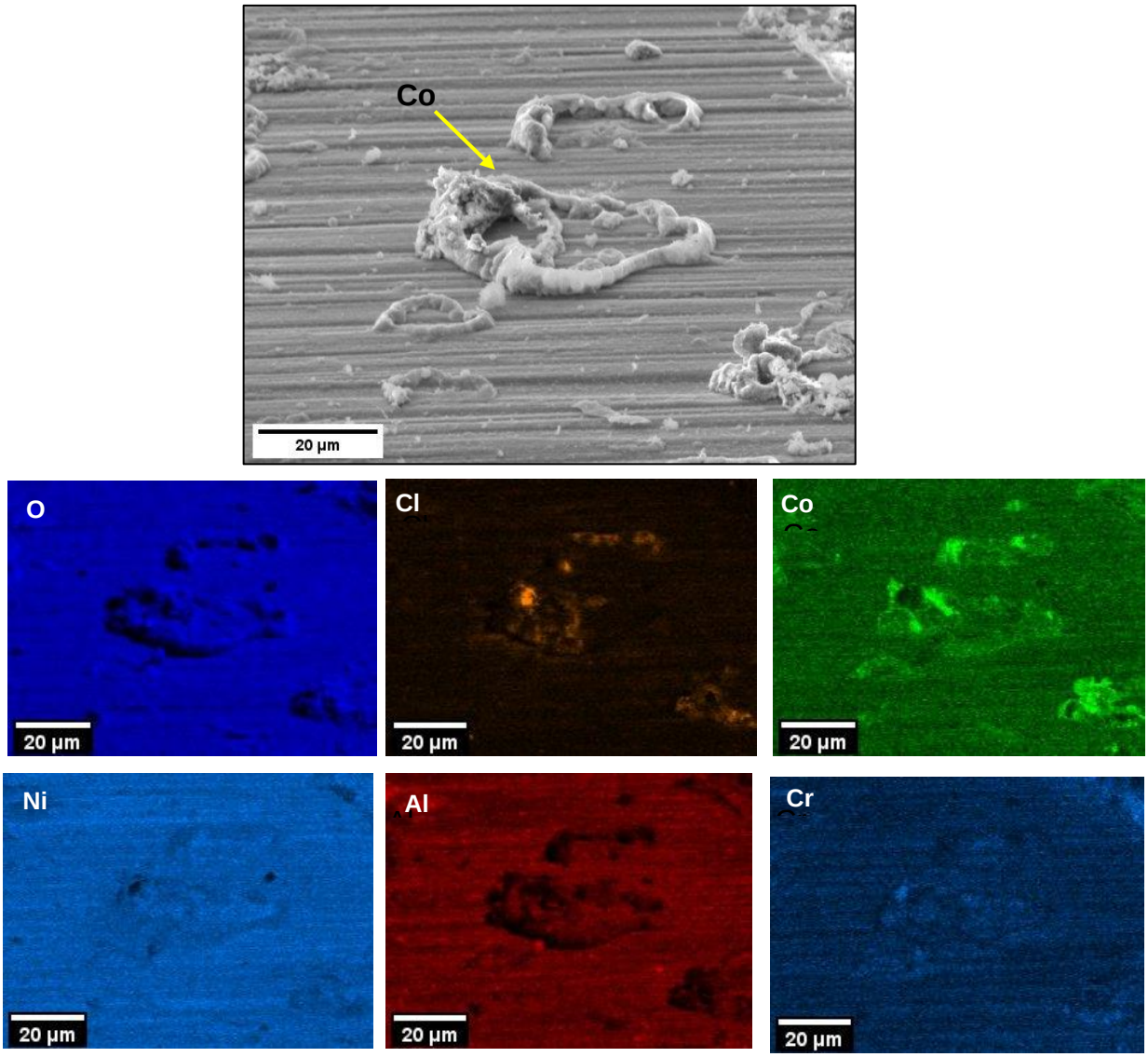


*Figure 68 - EDS map of the top surface of salted C-ring exposed in air for 50 hours*

Figure 69 shows a strong association of Co with some the salt ridges. Also, nodule type particles formed adjacent to the salt ridges, and according to the EDS map in Figure 69, it suggests the formation of $Na_2CrO_4$. These features where not observed in the sulphur-containing environment, so it is thought that the sulphation of NaCl occur in preference to reactions of NaCl with the oxide scale. Even if we do form $Na_2CrO_4$ in the sulphur-containing environment, it would then readily react with $SO_2$ or $SO_3$ to form $Na_2SO_4$ and $Cr_2O_3$ as suggested in [132].

The EDS map in Figure 68 shows very low concentrations of Na and Cl within the ridge of the salt. Given the high vapour pressure of NaCl at this temperature

(fugacity of 2.17 x $10^{-7}$ atm based on FactSage 8.1 calculations), a significant amount of salt may have vaporised away.

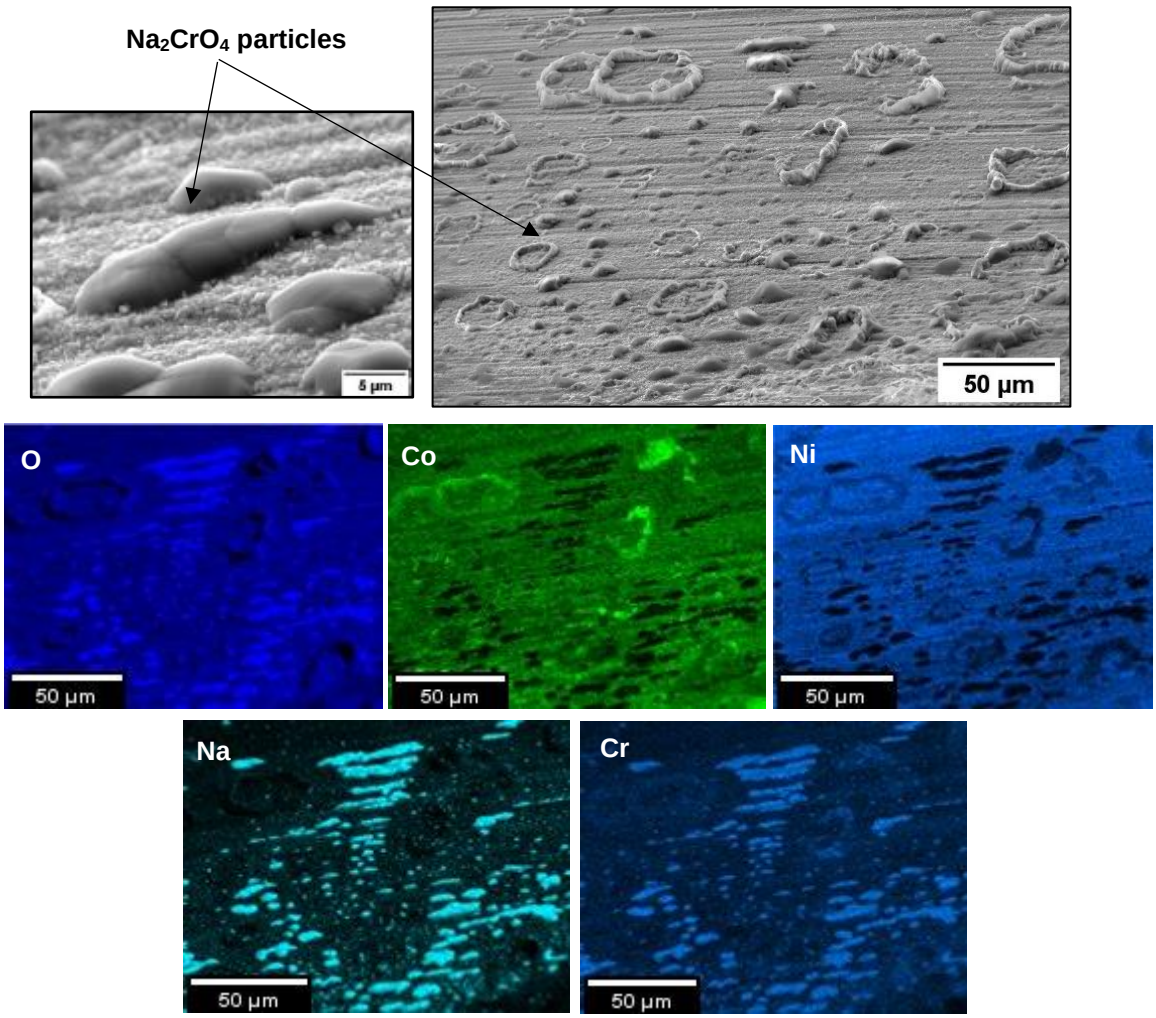


*Figure 69 – Top surface EDS map of C-ring exposed in air for 50 hours*

As shown in Figure 70, sites of scale spallation showed faceted particles rich in Na, Re and O. Other particles showed the presence of Na, W and O. These particles were only present in spallation sites and not observed in other regions.

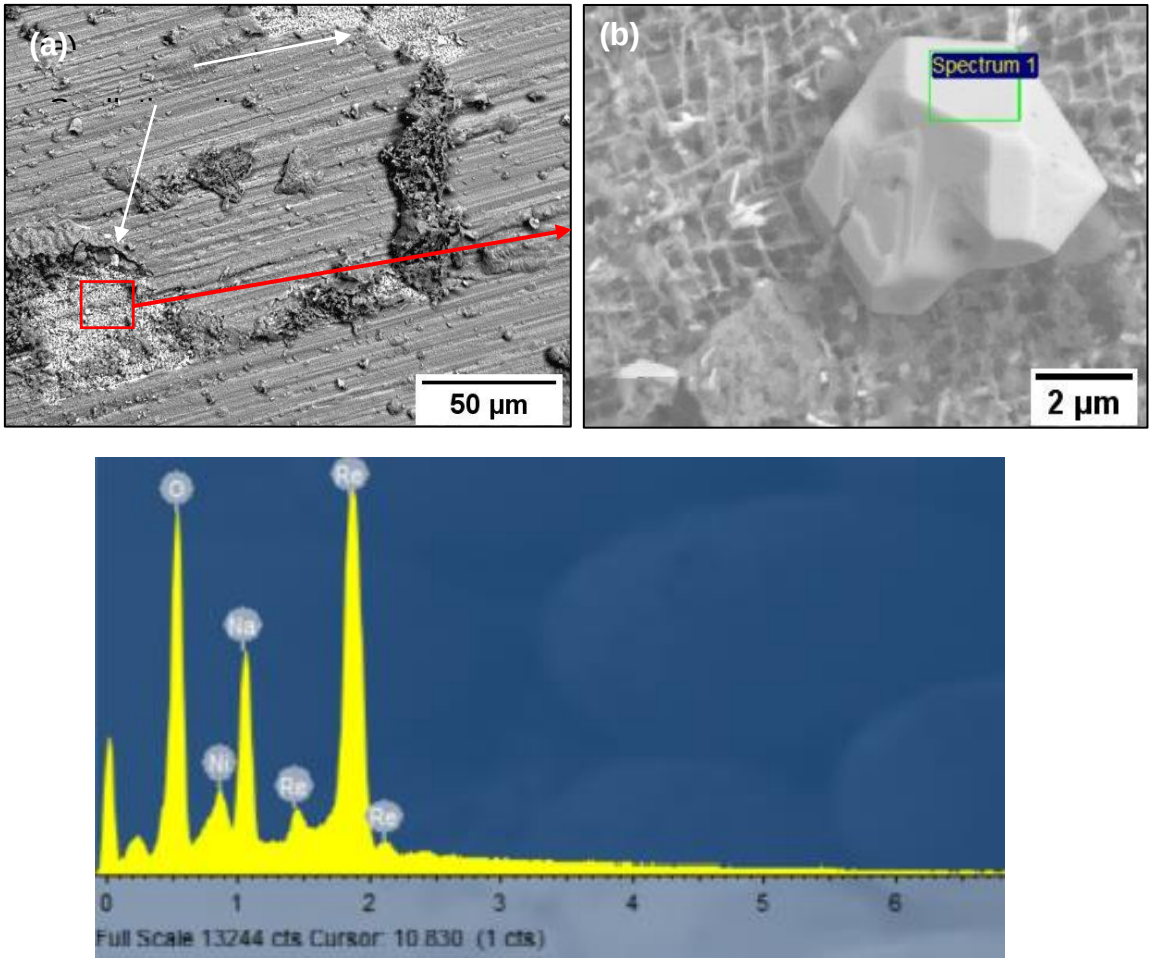


*Figure 70 – (a) Top surface SE image of C-ring exposed in air for 50 hours, (b) Na and Re rich particle present in palation site.*

Figure 71 shows a cross section across one of the salt particles. One micron of internal attack and negligible amounts of chlorine are present at the alloy/scale interface. It is thought that the partial pressure of $Cl_2$ at the alloy/scale interface did not reach the critical level to chlorinate Al, Ti, Cr and Re. This suggests that negligible chlorination of alloy elements has occurred.

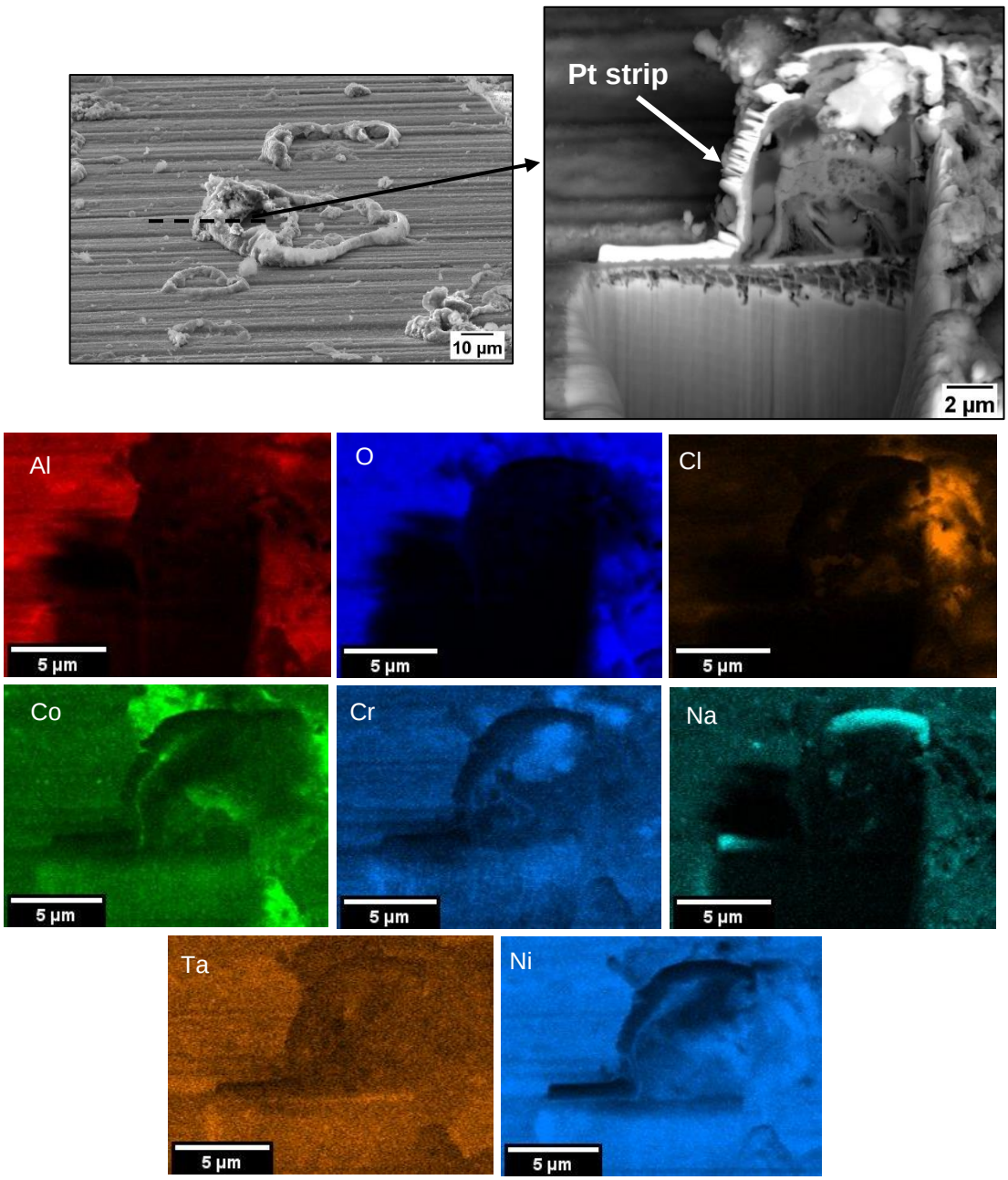


*Figure 71 – Cross-sectional EDS map of C-ring salted with NaCl and exposed in air for 50 hours*

### 5.3.6 Testing at 450°C

Figure 72 shows an EDS map of a C-ring's apex region after being exposed to a 50 ppm $SO_2$ – air environment at 450°C with NaCl salt. Some association of Na and S can be appreciated, indicating that some NaCl particles have reacted with $SO_2/SO_3$ to form $Na_2SO_4$.

For a specimen tested at 450°C, see Figure 72, FIB milling was carried out below one of the salt particles confirming the presence of a crack, which was in a region of maximum stress. Similarly, to the 550°C, NaCl diffused laterally on the surface from the location it was initially deposited in, and sulphated in the process, eventually. Compared to the amount of corrosion attack, and lower stresses needed to crack at 550°C, the extent of corrosion attack and embrittlement is significantly reduced at 450°C. Some chlorination still occurs, and evidence of Co chlorination may be observed in Figure 72. However, reduced temperature likely leads to lower rates of sulphation, lower diffusion rates of $Cl_2$ and HCl through the scale, lower reaction kinetics of metal chloride formation. Potentially, this may reduce the rate in which H would be injected into the alloy. Consequently, this may explain the lesser extent of cracking observed.

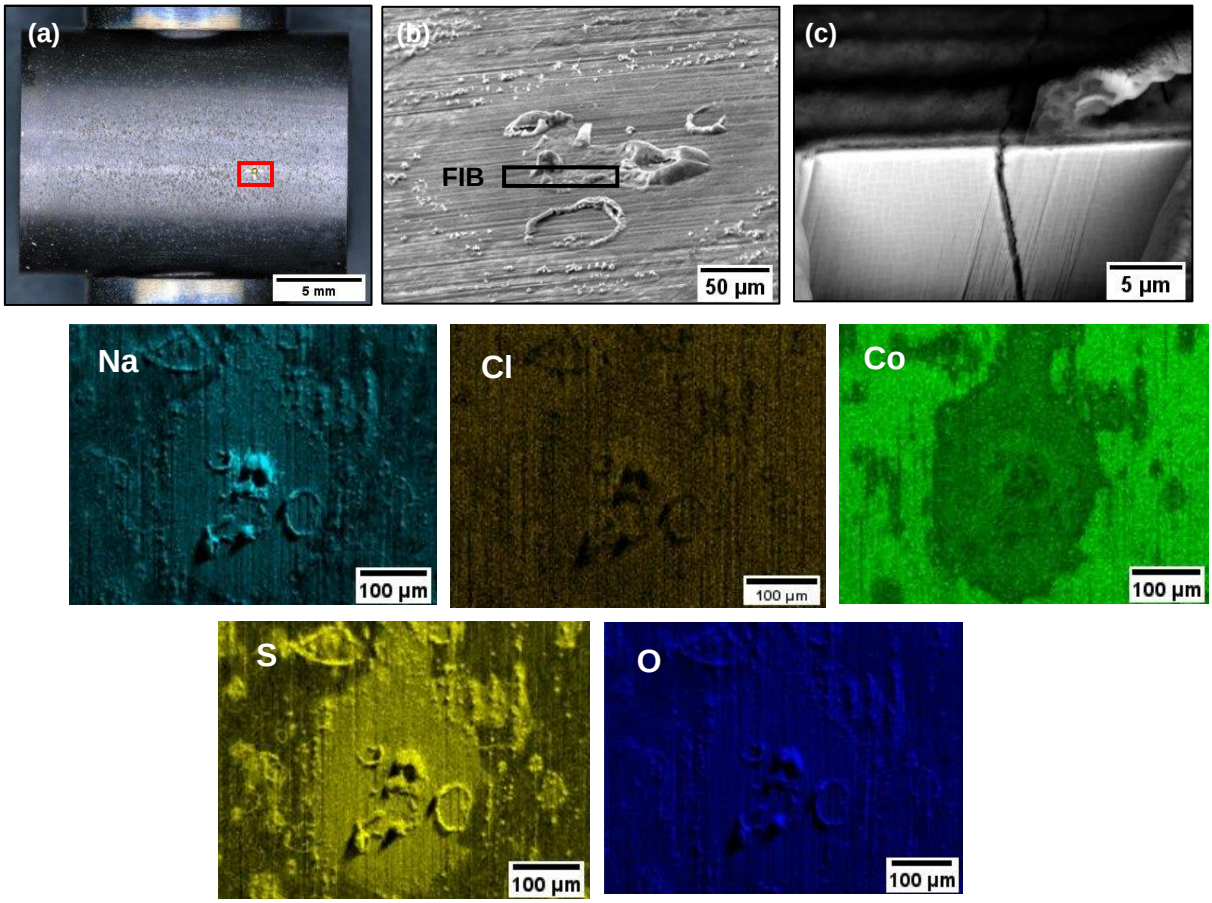


*Figure 72 –Cross-sectional EDS map (of the apex region) of C-ring salted with NaCl and exposed in 50 ppm $SO_2$ – air at 450°C for 50 hours*

## 5.4 Discussion

### 5.4.1 Effect of NaCl on the stress corrosion cracking in a 50 ppm $SO_2$ + Air

This section has shown that the synergistic effect of stress, NaCl deposits and a 50 ppm $SO_2$ – air gaseous atmosphere cause cracks to initiate on CMSX-4 at exposure times as low as 10 minutes. As the exposure time increases, cracks initiate in regions of lower stress until a critical threshold stress between 400 - 500 MPa is reached within 2 hours of exposure.

In the initial stages of the exposure, lateral transport of NaCl across the alloy surface occurs and its simultaneous sulphation, which releases HCl and $Cl_2$ gas. These gases, together with $O_2$ and $SO_2/SO_3$ from the gas atmosphere, diffuse through the scale to the scale/alloy interface. Evidence from the TEM analysis of a C-ring exposed for 2 hours (Figure 58) showed sulphur, oxygen and chlorine attacking the γ in the initial stages of the exposure. The reason of the preferential attack of the gamma matrix of O, S and Cl and the diffusion path is not well understood. But it is thought that, due to the applied stress, dislocations gather at the γ/γ' interface, leading to an increase in vacancies. The vacancies and channels formed due to the dislocations act as fast diffusion paths for the ingress of oxygen, sulphur and chlorine-containing species. Figure 58 shows that, after 2 hours of exposure, the corrosion attack consists of a complex interplay of sulphidation, oxidation and chlorination. Also, the predominance diagram in Figure 73 shows that metal chlorides and metal sulphides are formed at low partial pressures of $O_2$; which suggests that an oxide scale must be formed in the very initial stages of the exposure. The oxide scale then provides the low partial pressures of $O_2$ required at the scale/alloy interface for metal chlorides and metal sulphides to form.

The preferential phases formed can be best described using predominance diagrams. Based on the depletion of Ni, Co, Cr and Ti from the gamma phase and its accelerated oxidation within the deposit or at the scale/alloy interface after two hours of exposure (Figure 58), it is thought that active oxidation occurs,

leading to the chlorination of the various alloying elements and their oxidation at the alloy/scale interface of scale/gas interface. Therefore, an initial starting point for this modelling work has been focused on the predominance diagrams, highlighting the partial pressures of $SO_2$ and $O_2$ likely to be present in the subsurface ($p(SO_2) = 10^{-20}$ atm and $p(O_2) = 10^{-30}$ atm) and a constant $p(Cl_2) = 10^{-10}$ atm. In these conditions, $NiCl_2$, $CrCl_2$, $CoCl_2$, $TiCl_4$, $Al_2Cl_6$, $Al_2O_3$, $WS_2$ and Re are likely to be the most stable phases. Eventually, $NiCl_2$, $CrCl_3$ and $CoCl_2$ will diffuse outwards and reoxidise leaving the gamma phase depleted of these elements. Similarly, $TiCl_4$ and $AlCl_3$ will diffuse outwards and reoxidise leaving the gamma depleted of these elements.

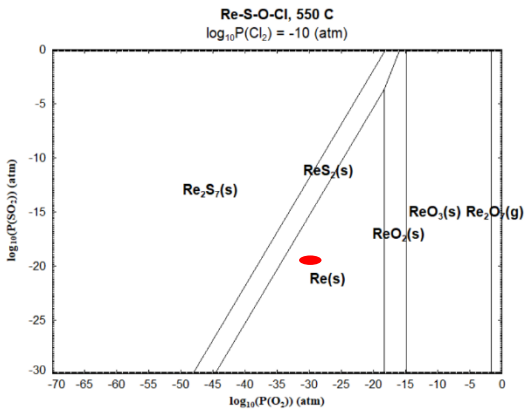
Re-S-O-Cl, 550 C
log10P(Cl2) = -10 (atm)
Re2S7(s)
ReS2(s)
ReO3(s)
Re2O7(g)
ReO2(s)
Re(s)
log10(P(SO2)) (atm)
log10(P(O2)) (atm)

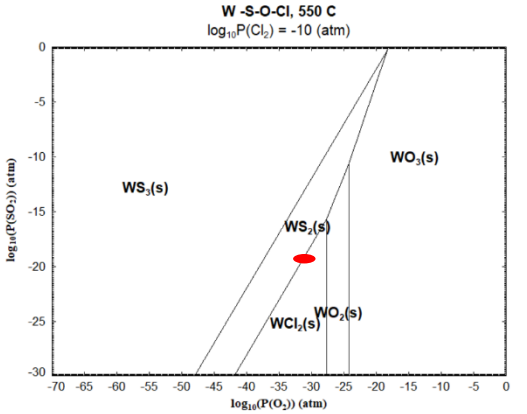
W -S-O-Cl, 550 C
log10P(Cl2) = -10 (atm)
WS3(s)
WO3(s)
WS2(s)
WCl2(s)
WO2(s)
log10(P(SO2)) (atm)
log10(P(O2)) (atm)

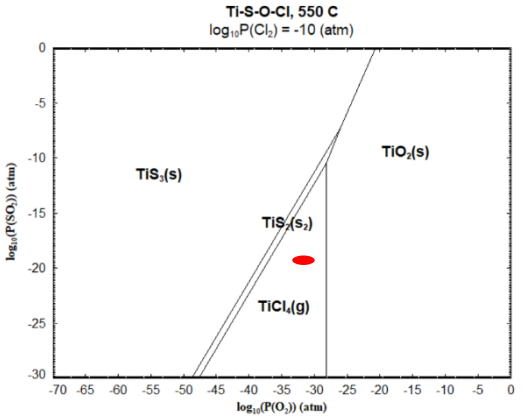
Ti-S-O-Cl, 550 C
log10P(Cl2) = -10 (atm)
TiS3(s)
TiO2(s)
TiS2(s2)
TiCl4(g)
log10(P(SO2)) (atm)
log10(P(O2)) (atm)

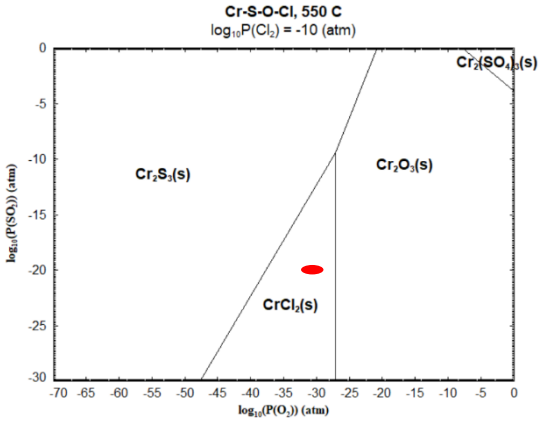
Cr-S-O-Cl, 550 C
log10P(Cl2) = -10 (atm)
Cr2(SO4)3(s)
Cr2S3(s)
Cr2O3(s)
CrCl2(s)
log10(P(SO2)) (atm)
log10(P(O2)) (atm)

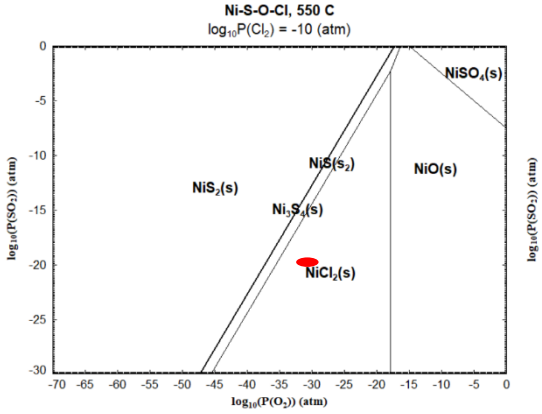
Ni-S-O-Cl, 550 C
log10P(Cl2) = -10 (atm)
NiSO4(s)
NiS2(s)
NiS(s2)
NiO(s)
Ni3S4(s)
NiCl2(s)
log10(P(SO2)) (atm)
log10(P(O2)) (atm)

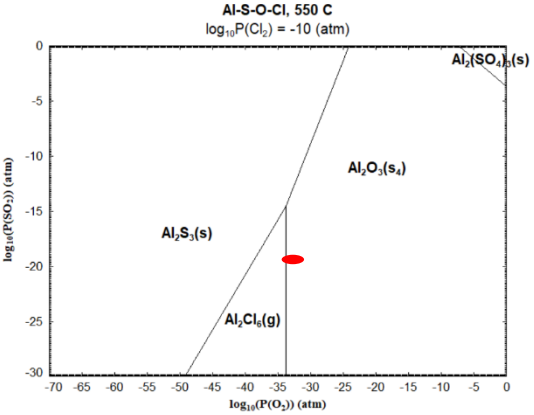
Al-S-O-Cl, 550 C
log10P(Cl2) = -10 (atm)
Al2(SO4)3(s)
Al2O3(s4)
Al2S3(s)
Al2Cl6(g)
log10(P(SO2)) (atm)
log10(P(O2)) (atm)

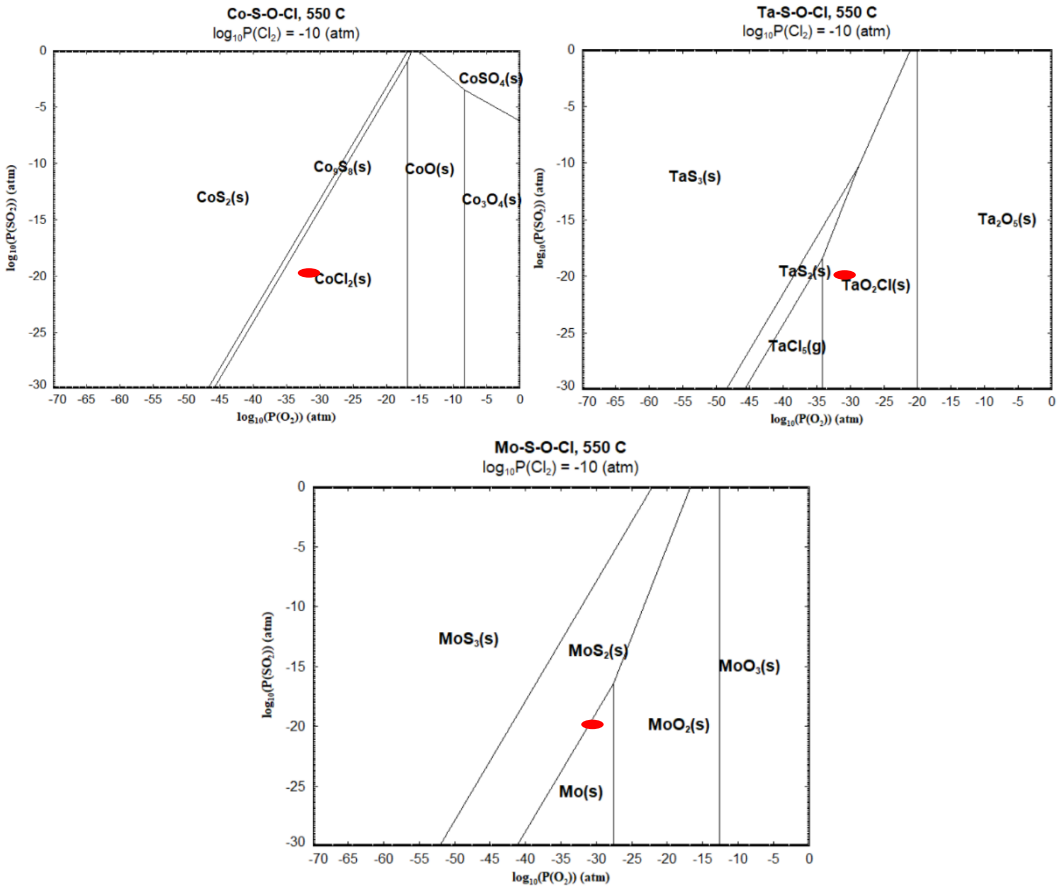


*Figure 73 – Phase stability diagram of $log_{10}(P(SO_2))$ vs $log_{10}(P(O_2))$ at a constant $P(Cl_2) = 10^{-10}$ atm*

The XRD and EDS analysis after 50 hours of exposure in Figure 62 substantiate the formation of $AlCl_3$, $TiCl_4$, $CrCl_3$, $NiCl_2$ and $CoCl_2$. As $NiCl_2$ and $CoCl_2$ oxidise at high $PO_2$, they reoxidise within the salt deposit and $AlCl_3$, $CrCl_3$ and $TiCl_4$ oxidises near the scale/alloy interface. The $NiCl_2$ and $CoCl_2$ that formed below the halo region, diffuse outwards leaving holes in the scale, therefore a porous scale is observed in the halo region after 50 hours of exposure.

The mechanism responsible for the lateral transport of the salt is still not well understood, but may have occurred due to surface diffusion, gas diffusion or as a result of a low melting point eutectic forming. A mechanism that would support the formation of a low melting point eutectic, would initiate with NaCl reacting with $SO_2/SO_3$ to form $Na_2SO_4$ and releasing HCl and $Cl_2$. The HCl and $Cl_2$ diffuses to the alloy/scale interface and forms $AlCl_3$, $CrCl_3/CrCl_2$ and $TiCl_4$. As metal chlorides, such as $CrCl_3$, form they reacts with excess NaCl on the surface to form a low melting point NaCl-$CrCl_3$ (mp. 544-593°C). Other potential low melting

point eutectic involving metal chlorides and excess NaCl are shown in Figure 74. The liquid formed will spread laterally on the surface and the $Cl^-$ in the melt can react with alloy elements to produce the metal chlorides. Eventually, if a molten chloride phase is formed, this may accelerate the rate of corrosion attack, as chemical reactions in a liquid phase may be faster than in solid-solid reactions [49].

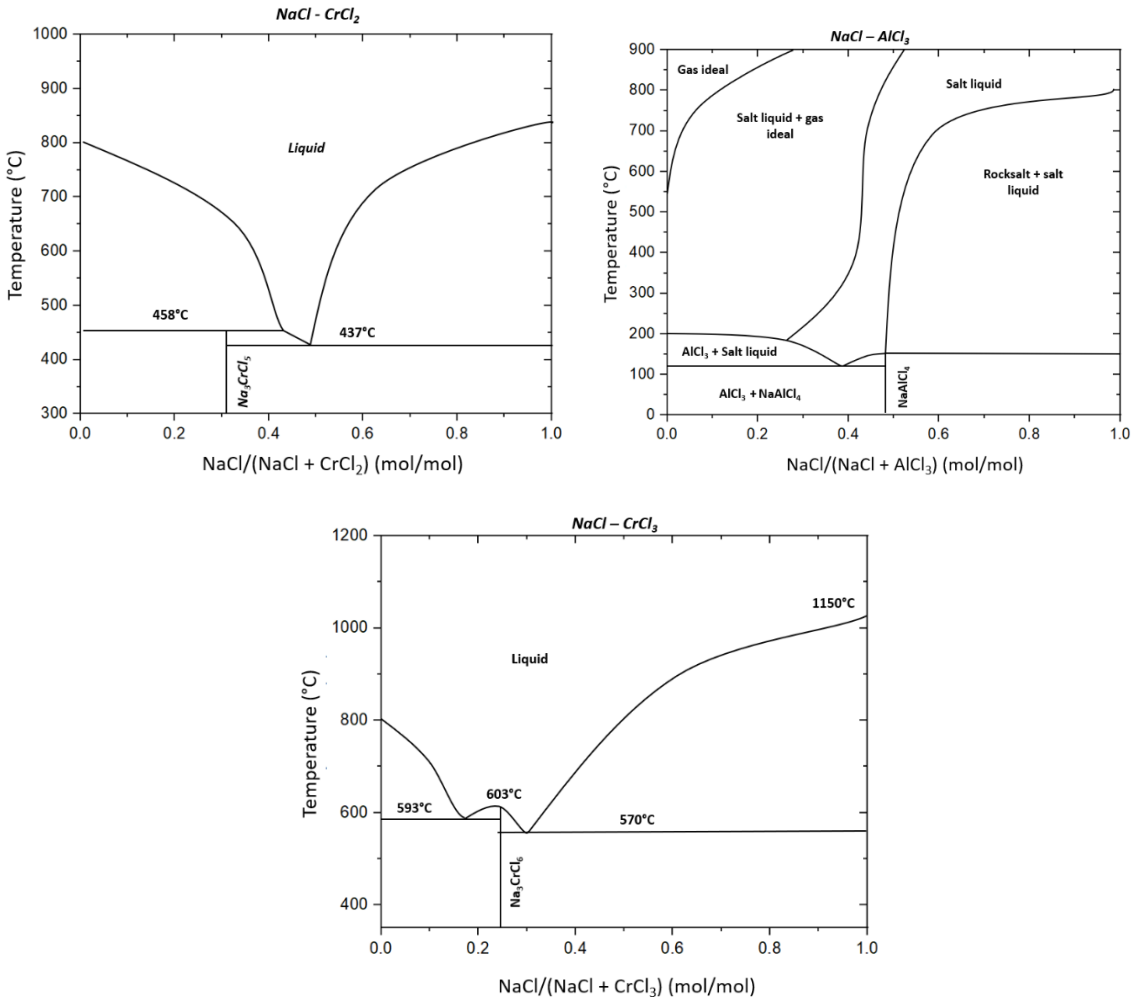


*Figure 74 – Phase diagrams of NaCl – $CrCl_3$, NaCl – $CrCl_2$* [133] *and NaCl – $AlCl_3$ (FactSage 8.1)*

Given that the X-ray diffraction in Figure 62 shows the formation of $Na_3CrCl_6$, this indicates an interaction of NaCl - $CrCl_3$, where a low melting point eutectic may have formed. However, based on the phase diagram in Figure 74, the melting point of this compound is 570°C, which is slightly above this test's temperature. Other low melting point eutectic may have formed, such as the ones resulting from the interaction of NaCl – $CrCl_2$ and NaCl – $AlCl_3$, which have low melting

point eutectic temperatures of 437°C and 130°C respectively, and within the test temperature tested in this thesis.

It is worth noting that the EDS map of the specimen exposed for 2 hours (Figure 58) shows that the NaCl salt has almost fully reacted with sulphur to form $Na_2SO_4$, as there is no association of Na with Cl, but there is a strong association of Na with S. Therefore, this suggests that most of the HCl and $Cl_2$, according to Table 12, has been released within the first 2 hours of exposure. As will be further discussed in section 5.6.1, if the formation of HCl and $Cl_2$ is supressed after two hours of exposure, the formation of metal chlorides and consequently the release of $H_2$ at the alloy/scale interface may also be supressed. In summary, this implies that the formation of the embrittling species, suggested to be hydrogen, is supressed after two hours of exposure and, therefore the environmental assisted crack growth is also supressed.

## 5.5 Exposure in air

Ni and Co rich oxides are observed within the salt ridge and negligible chlorination of Cr, Al, Ti and Re is observed. As indicated by the predominance diagrams in Figure 49 and Table 16, nickel and cobalt chloride require lower partial pressures of chlorine gas to form compared to other alloy elements (e.g. Al, Cr and Ti), if we were to assume partial pressures of $O_2$ at the alloy/scale interface between $10^{-10}$ – $10^{-30}$ atm as an initial starting point. Given the observation that only $NiCl_2$ and $CoCl_2$ form in the air exposure, it is suggested that the partial pressure of $Cl_2$ at the alloy/scale interface in the air exposure is significantly reduced compared to that found in the sulphur-containing gas exposures. Consequently, this lower partial pressure of $Cl_2$ present at the alloy/scale interface in the air exposure is above that required to form $NiCl_2$ and $CoCl_2$, but below that required to chlorinate Al, Cr, Re and Ti. So, in air, the only elements involved in the outward transport via volatile molecular species are Ni and Co.

As reported by Okoro et al. [134], the in-deposit sulphation of KCl can produce six orders of magnitude higher partial pressures of $Cl_2$ at the scale/alloy interface than that resulting from $K_2CrO_4$ formation. Although this paper did not provide an

explanation as to why this low partial pressure of $Cl_2$ occurs, one possible reason that may explain this observation is due to the lower kinetics of reaction of KCl with Cr or $Cr_2O_3$, which would release $Cl_2$ at a slower rate compared to the kinetics of reaction of KCl with $SO_2$ and $H_2O$. The interpretation by Okoro translates well to the observations in this thesis.

Once nickel chloride and cobalt chloride forms, they will diffuse outwards and oxidise when they reach higher partial pressures of oxygen near the gas/scale interface. This would explain the high concentration of nickel and cobalt oxide within the salt particles.

*Table 16 – Minimum $P(Cl_2)$ required to form metal chlorides at $P(O_2)$ of $10^{-20}$ (FactSage 8.1)*

| **Metal chloride** | **$AlCl_3$** | **$ReCl_3$** | **$CrCl_3$** | **$TiCl_4$** | **$CoCl_2$** | **$NiCl_2$** |
|---|---|---|---|---|---|---|
| $P(Cl_2)$ | $10^{-3}$ | $10^{-3}$ | $10^{-6}$ | $10^{-6}$ | $10^{-11}$ | $10^{-11}$ |

A key observation from the air exposure is that $Na_2CrO_4$ particles nucleate away from where the NaCl particles were initially deposited. For $Na_2CrO_4$ to form, it is postulated that NaCl reacts with Cr from the alloy to form $Na_2CrO_4$. Table 17 shows that reactions of NaCl with Cr, Re and W can occur when NaCl is in the solid phase or in the gas phase. However, based on the change in Gibbs free energy calculations, the reactions with NaCl in the gas phase are more stable.

The melting point of NaCl is 801°C and $Na_2CrO_4$ melts at 761°C. However, as $Na_2CrO_4$ particles are formed they may react with excess NaCl and lead to the formation of a lower melting point eutectic.

*Table 17 – Change in Gibbs free energy of reactions of NaCl with alloy elements*

| **Reactions** | **ΔG (J)** |
|---|---|
| $\mathrm{NaCl}\ (g) + 0.5\mathrm{Cr} + 0.75O_2 + 0.5H_2\mathrm{O} \rightarrow 0.5Na_2CrO_4 + \mathrm{HCl}$ | -292232.6 |
| $\mathrm{NaCl}\ (g) + \mathrm{Re} + 0.5H_2\mathrm{O} + 1.75O_2 \rightarrow \mathrm{Na}ReO_4 + \mathrm{HCl}$ | -526381.4 |

$$Interaction\ of\ 60\%\ Na_2CrO_4 - 40\%\ NaCl$$
$$\rightarrow Molten\ phase\ with\ low\ m.p\ eutectic$$

As highlighted in the phase diagram from Figure 76, the minimum melting point in the NaCl-$Na_2CrO_4$ system is 557°C (slightly above the test temperature). The curvature of the top and bottom parts of the C-ring would encourage that downward spread of the molten phase from the region where it is formed, as observed in Figure 75.

Based on the XRD assessment, evidence of sodium chromate formation was also observed in the sulphur containing environment, but it was not as significant as in the air exposure. As discussed in section 5.3.5, $Na_2CrO_4$ may have formed but the presence of $SO_2/SO_3$ has led it to the formation of $Na_2SO_4$ afterwards. This has been explored similarly in [132].

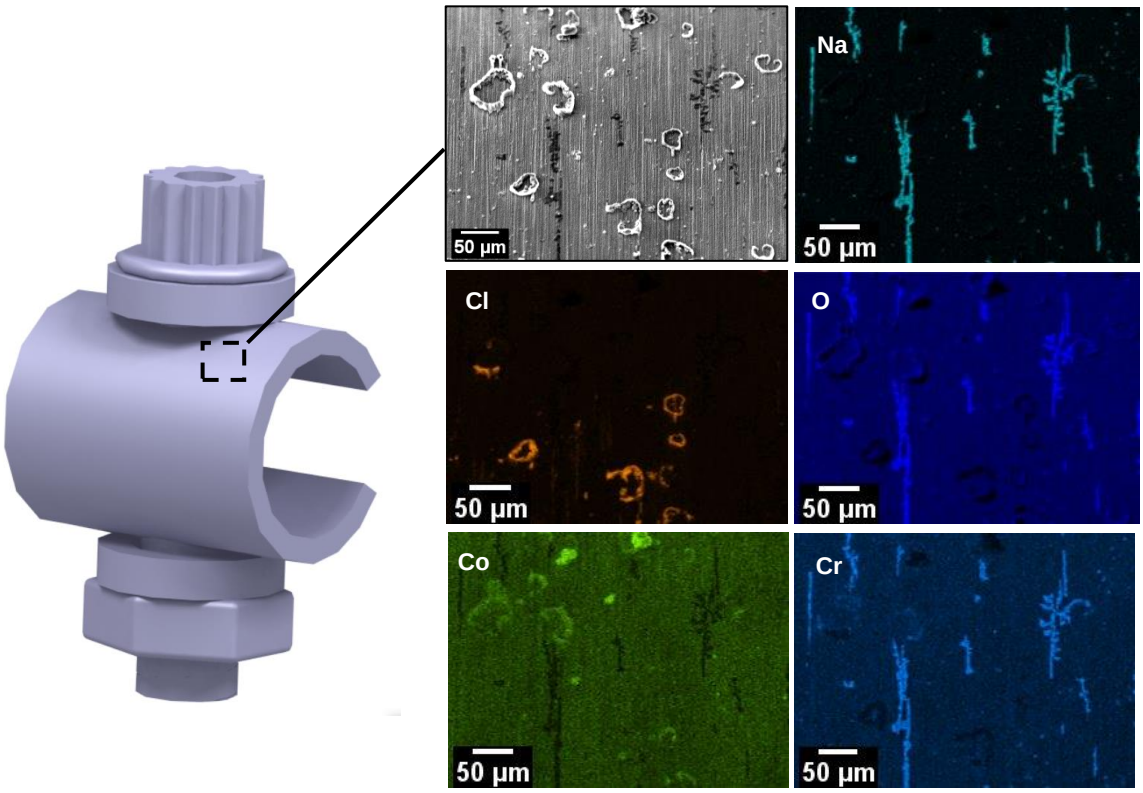


*Figure 75 – EDS map of potential molten eutectic NaCl – $Na_2CrO_4$ formed on CMSX-4 C-ring exposed in air at 550°C for 50 hours*

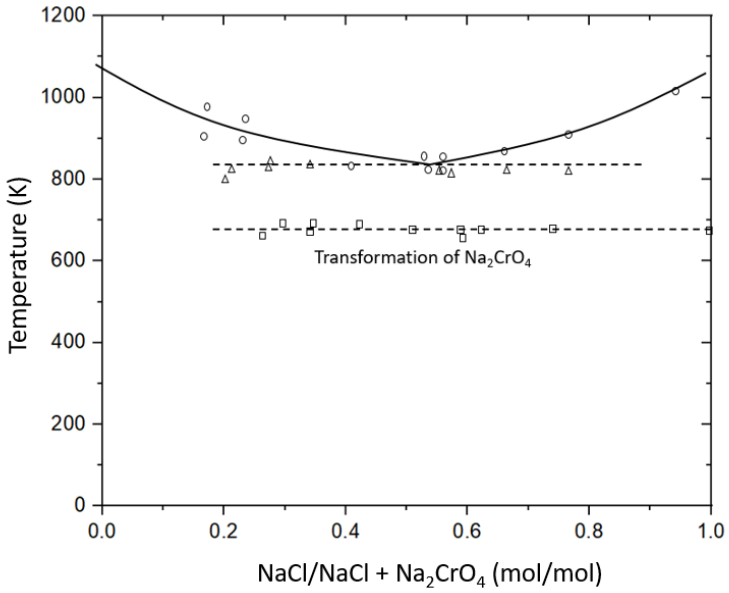


*Figure 76 – Phase diagram of NaCl – $Na_2CrO_4$* [135]

As reported by Okoro et al. [134], the concentration of $SO_2/SO_3$ plays an important role in the corrosion behaviour when KCl is condensed on a metallic surface, and based on the experimental results observed in this thesis, we seem to find a similar behaviour with NaCl. Although Grabke et al. [136] suggest that intra deposit sulphation of KCl lead to higher corrosion rates when a $SO_2/SO_3$ concentration of 250 – 1000 ppm was used compared to air exposures, it has also been reported by Paneru et al. [137] that much higher concentrations of $SO_2/SO_3$ (15000 ppm) reduces corrosion rates as it preferentially sulphates alkali chlorides in the deposit/gas interface, reducing the generation of HCl close to the alloy/scale interface. So, the $SO_2/SO_3$ concentration plays a role on the preferential sites of NaCl sulphation within the deposit which, in turn, plays a role on the partial pressures of $Cl_2$ at the scale/alloy interface, and therefore on corrosion rates. In summary, the accelerated corrosion rates observed in this study at the low concentrations of 50 ppm $SO_2$ tested agree well with the results from Grabke et al. [136].

It is worth noting that in previous work undertaken in hot salt stress corrosion cracking of Ti-alloys (where NaCl salt causes cracks to form in Ti-alloys when exposed to air up to temperatures of 500°C) [83], it was observed that pure Ti is immune to hot salt stress corrosion cracking caused by NaCl, but adding Al made

it susceptible to cracking through hydrogen embrittlement. They also observed that the higher the Al concentration in the alloy [83] , the more significant was the life reduction. Further work led to the conclusion that the reaction of HCl with Al to form $AlCl_3$ leads to hydrogen embrittlement, but the reaction of HCl with Ti to form $TiCl_4$ does not, which explained the susceptibility of Ti-alloys to HSSCC. So clearly, there are specific elements that, when chlorinated, make the alloy susceptible to hydrogen embrittlement. An explanation of why the chlorination of Al leads to hydrogen embrittlement was not provided, but it was proposed that the highly negative Gibbs free energy change of $AlCl_3$ formation is important in releasing high concentrations of hydrogen in a short amount of time (which is a prerequisite to inject hydrogen rapidly into the alloy before it diffuses away at 500°C). Ultimately, a similar effect may be observed in this study, where the presence of $SO_2/SO_3$ leads to the chlorination of Al, Cr and Ti, whereas the chlorination reactions of Al, Cr and Ti are not observed in the air exposure. So, in air, even though the reactions of HCl with Ni and Co occurs, these reactions may not be powerful enough, and the low concentrations of hydrogen that could be injected into the material would be insufficient to cause cracking. To further support this claim, it would be interesting to study the kinetics of reactions of Al with HCl, as this would dictate the rate at which $H_2$ is being released at the alloy/scale interface.

## 5.6 Tests performed at 450°C

Further tests undertaken at 450°C show that NaCl also initiates cracks in the first 50 hours of exposure at this temperature. Diffusion of NaCl is again observed but no significant chlorination is observed. Here, only the chlorination of Co within the salt ridge is evident, and only, the highly stressed region (700 – 800 MPa) shows crack formation.

### 5.6.1 Postulated mechanisms

There are two hypotheses proposed for the mechanism of crack formation in the alloy at 450°C and 550°C.

***Hypothesis 1***

The first possible mechanism of near surface weakening is based on hydrogen embrittlement, it is of similar character to the mechanisms observed in hot salt stress corrosion cracking of Ti alloys with the mechanism divided into different stages.

*Stage 1*

Within the first 5 minutes of exposure, NaCl undergoes surface diffusion and during this process reacts with $SO_2$/$SO_3$ and traces of $H_2O$ that are present in the atmosphere or present as inclusions in the salt. The sulphation reaction of NaCl leads to the formation of HCl as well as $Cl_2$, according to the expression below.

$$2NaCl(g) + SO_2(g) + 0.5O_2(g) + H_2O(g) = Na_2SO_4(s) + 2HCl(g)$$

$$2NaCl\ (g) + SO_2(\mathrm{g}) + O_2(\mathrm{g}) = Na_2SO_4(\mathrm{s}) + Cl_2(g)$$

*Stage 2*

Some of the $Cl_2$ and HCl formed will be lost to the atmosphere, and some will diffuse inwards. Ultimately, the mechanism of $Cl_2$ and HCl diffusion through the scale is not well understood and should be further explored. Once a scale has formed in the early stages of the exposure, a low partial pressure of $O_2$ is formed at the alloy/scale interface. As shown in the predominance diagrams of Figure 73, the low partial pressure of $O_2$ at the alloy/scale interface leads to the reaction of HCl and $Cl_2$ with Al, Cr, Ni, Co, Ti to form their corresponding volatile metal chlorides and release $H_2$ at the alloy/scale interface. In previous studies on Ti-alloys [83], it was reported that the reaction of HCl and alloy elements forms nascent hydrogen, but based on FactSage 8.1 calculations, these reactions are not thermodynamically favourable. Instead, it is suggested that $H_2$ is produced according to the expressions in the right-hand side of Table 18.

*Table 18 - Change in Gibbs free energy of metal chloride formation from FactSage 8.1*

| Metal chloride reaction | ΔG (J) at 550°C | Vapour pressure (atm) at 550°C | Metal chloride reaction | ΔG (J) at 550°C | Vapour pressure (atm) at 550°C |
|---|---|---|---|---|---|
| $2Al + 3Cl_2 = 2AlCl_3$ | -1087209 | $AlCl_3$ = 0.497 | $2Al + 6HCl = 2AlCl_3 + 3H_2$ | -489448.6 | $AlCl_3$ = 0.497 |
| $2Ti + 3Cl_2 = 2TiCl_3$ | -1084320.3 | $TiCl_3$ = 0.00184 | $2Ti + 6HCl = 2TiCl_3 + 3H_2$ | -486559.5 | $TiCl_3$ = 0.00184 |
| $Ti + 2Cl_2 = TiCl_4$ | -663694.9 | $TiCl_4$ = 1 | $2Ti + 8HCl = 2TiCl_4 + 4H_2$ | -530375.5 | $TiCl_4$ = 1 |
| $2Cr + 3Cl_2 = 2CrCl_3$ | -713632.1 | $CrCl_3$ = 7.1E-6 | $2Cr + 6HCl = 2CrCl_3 + 3H_2$ | -115871.3 | $CrCl_3$ = 7.1E-6 |
| $Ni + Cl_2 = NiCl_2$ | -181396 | $NiCl_2$ = 1.9E-5 | $2Ni + 4HCl = 2NiCl_2 + 2H_2$ | +35715.1 | $NiCl_2$ = 1.9E-5 |
| $Co + Cl_2 = CoCl_2$ | -200133 | $CoCl_2$ = 3.75E-5 | $2Co + 4HCl = 2CoCl_2 + 2H_2$ | -1758.8 | $CoCl_2$ = 3.75E-5 |
| $Co + 1.5\ Cl_2 = CoCl_3$ | -138669 | $CoCl_3$ = 1.26E-4 | $2Co + 6HCl = 2CoCl_3 + 3H_2$ | +320422.8 | $CoCl_3$ = 1.26E-4 |

*Stage 3*

$H_2$ is adsorbed on the alloy surface and dissociates to form nascent hydrogen, which is then injected into the material. This dissociative mechanism of $H_2$ into atomic H has been investigated previously at high temperatures and gas pressures and has proven to be thermodynamically feasible [138]. When H is injected into the alloy and the solubility limit of hydrogen is reached, cracking will occur. The manner in which nascent hydrogen embrittles is still to be investigated. For titanium alloys, it is as titanium hydrides [83], but this mechanism is not proven for nickel-based superalloys. Previously reported mechanisms, such as hydrogen induced decohesion, formation of brittle metal hydrides or hydrogen induced localised plasticity are potential mechanisms, which should be further investigated in nickel-based superalloys. In addition, the depletion of alloying elements (or dealloying, which is a common mechanism of stress corrosion cracking [116]) from the near surface due to the chlorine-assisted mechanism may have also played a role in reducing the mechanical properties of the alloy, but this needs further evidence, potentially through nanomechanical testing.

In parallel to the above reactions, the metal chlorides that formed diffuse outwards through defects in the oxide scale. Below the salt ridge the activity of oxygen is reduced, and the activity of $H_2O$ is increased as reported by Chevrot [83]. So, metal chlorides react with $H_2O$ to form porous metal oxides, releasing HCl again, as shown in Table 19. Some of the HCl is lost to the atmosphere and

some diffuses inwards through the oxide to repeat the process described in stage 2, causing further injection of H into the alloy.

*Table 19 - Gibbs free energy change of metal chloride oxidation at 550°C from FactSage 8.1*

| Metal chloride reaction | ΔG (J) at 550°C |
|---|---|
| $NiCl_2 + 0.5\ O_2 = NiO + Cl_2$ | -57846.2 |
| $NiCl_2 + SO_2 + O_2 = NiSO_4 + Cl_2$ | -159724.4 |
| $CoCl_2 + 0.5\ O_2 = CoO + Cl_2$ | -45372.6 |
| $CoCl_2 + SO_2 + 0.5O_2 = \mathrm{Co}SO_4 + Cl_2$ | -166188.1 |
| $AlCl_3 + 0.75\ O_2 = 0.5\ Al_2O_3 + 1.5\ Cl_2$ | -165260.2 |
| $TiCl_3 + O_2 = TiO_2 + 1.5\ Cl_2$ | -295054.2 |
| $TiCl_4 + O_2 = TiO_2 + 2\ Cl_2$ | -130433.4 |
| $CrCl_3 + 0.75\ O_2 = 0.5\ Cr_2O_3 + 1.5\ Cl_2$ | -98752.8 |

| Metal chloride reaction | ΔG (J) at 550°C |
|---|---|
| $NiCl_2 + H_2\mathrm{O} = NiO + 2\mathrm{HCl}$ | -54795.6 |
| $NiCl_2 + H_2\mathrm{O} + SO_2 + 0.5O_2 = NiSO_4 + 2\mathrm{HCl}$ | -156673.9 |
| $CoCl_2 + H_2\mathrm{O} = CoO + 2HCl$ | -42322.1 |
| $CoCl_2 + H_2\mathrm{O} + SO_2 + 0.5O_2 = \mathrm{Co}SO_4 + 2\mathrm{HCl}$ | -163137.5 |
| $2AlCl_3 + 3\ H_2\mathrm{O} = Al_2O_3 + 6\ \mathrm{HCl}$ | -321368.7 |
| $2TiCl_3 + 0.5O_2 + 3H_2\mathrm{O} = 2TiO_2 + 6HCl$ | -494784.8 |
| $2TiCl_4 + 4H_2\mathrm{O} = 2TiO_2 + 8HCl$ | -248664.7 |
| $2CrCl_3 + 3H_2\mathrm{O} = Cr_2O_3 + 6HCl$ | -188354.1 |

According to Chevrot [83], at temperatures of 500°C, high concentrations of H must be injected into the material in a short amount of time to cause embrittlement (as hydrogen can diffuse away rapidly at these high temperatures), and this was mainly achieved by the reactions of HCl with Al to form $AlCl_3$. For the case of CMSX-4, it is thought that this rapid injection of high concentrations of hydrogen is achieved in the presence of NaCl in a 50 ppm $SO_2$ – air environment, given that it triggers the formation of $AlCl_3$, but not in the presence NaCl and air only, as the partial pressure of $Cl_2$ at the alloy/scale interface in the “air” exposure is insufficient to form $AlCl_3$. As mentioned in the literature review, the concentration of $SO_2/SO_3$ plays a key role in the kinetics of sulphation. So, further work could include reducing the concentration of $SO_2/SO_3$ to determine what the minimum level is to cause cracking.

No cracks were observed to initiate within the halo away from the salt ridge. A possible explanation is that insufficient hydrogen is rapidly injected in these regions to cause cracking. However, the fact that cracks arrest at the boundary of the halo suggest that these regions play a role on the extent of propagation of the cracks.

*Stage 4*

Once cracks form, they act as fast diffusion paths for $SO_2/SO_3$, $O_2$ and HCl ingress. HCl can react with alloy elements (i.e., Al, Ti and Cr as evidenced by Figure 62). Potentially, these reactions can further inject high concentrations of H ahead of the crack tip, leading to embrittlement and crack propagation and also provide a mechanism for the transport of chlorides deeper into the alloy, exacerbating the crack growth.

Based on the EDS map in Figure 58, after two hours of exposure there are insignificant amounts of NaCl remaining on the surface, as it has reacted with the gas atmosphere to form $Na_2SO_4$. Therefore, there is no further formation of $Cl_2$ and HCl, so hydrogen is no chlorination reactions no longer occur. Consequently, the $H_2$ that is released in the chlorination reactions no longer occurs; therefore, hydrogen is no longer injected into the material. This suppression of H injection in a rapid manner, causes the crack growth to become negligible after longer than two hours of exposure.

As further experimental evidence that confirms the rapid consumption of NaCl, the concentrations of NaCl and $Na_2SO_4$ after two hours can be measured using ion chromatography. Nevertheless, the work of Karlsson et al. [132] further corroborated this rapid consumption of NaCl, as they observed that after 1 hour, 89% of KCl particles were sulphated to form $K_2SO_4$. These tests were undertaken in 5% $O_2$, 40% $H_2O$, 300 ppm $SO_2$ and KCl, so clearly a different salt and a much higher concentration of $SO_2$ than the one used in this test. But given the observation in this study that NaCl has almost reacted to form $Na_2SO_4$ in the first two hours of the test, and the results from Karlsson [132] it is thought that the kinetics of sulphation of NaCl in the current test does not differ significantly from Karlsson et al. [132].

From the TEM work undertaken, no evidence of brittle hydrides was observed in the near surface or at the crack tip. Further work in identifying evidence of

hydrogen induced decohesion or enhanced plasticity due to hydrogen is required to gain insight into the mechanism that operates.

In air, even though $Cl_2$ and HCl is still formed due to reaction of NaCl with Cr and Re, these reactions are not sufficiently powerful and the negligible amounts of hydrogen which are injected in the material are insufficient to cause cracking. So, although hydrogen is injected in the alloy, it can diffuse away from the near surface before sufficient levels to cause the initiation of cracks.

***Hypothesis 2***

The second hypothesis is based on embrittlement due to $Cl^-$ ions. There is less evidence in terms of literature and experimental findings in this project to support this mechanism. But nevertheless, it is worth considering until it can be disproved. Again, this mechanism is divided into different stages.

*Stage 1*

The sulphation of NaCl releases HCl and $Cl_2$, which reacts with Cr, Al, Ti, and Co to form their corresponding metal chlorides.

*Stage 2*

The metal chlorides $AlCl_3$, $CrCl_3$ and $CrCl_2$ react with excess NaCl on the surface and leads to the formation of low melting point eutectic NaCl-$AlCl_3$, NaCl-$CrCl_3$ or NaCl-$CrCl_2$. The phase diagrams in Figure 74 shows the eutectic composition corresponding to the lowest melting point and suggests that they may occur in the temperatures tested in this study. This is further complemented by the EDS and XRD observations.

*Stage 3*

The formation of a chloride melt generates $Cl^-$ electronegative ions [139], which diffuse rapidly through grain boundaries of the scale and adsorb in appropriate defect sites in the near surface of the alloy. Once absorbed, it reduces the cohesive strength of metal-metal bonds, leading to the nucleation of cracks. The effect of chloride ions in embrittling Ti-alloys in HSSCC has been previously

postulated by Logan et al. [87]. However, there is limited evidence to support this claim.

Apart from the work undertaken by Logan et al. [87], it has previously been suggested that chloride ions are embrittling by reducing the bond strength between alloy elements (analogous to liquid metal embrittlement). This is based on Ab initio calculations, which suggest that the absorption of chloride ions and H in (001) cleavage planes [140], cause a reduction in fracture roughness or surface energy/cohesive forces by 48%. Eventually, if the concentrated normal stress applied to a low surface-energy cleavage plane exceed its reduced critical cleavage stress, cleavage plane rupture occurs and a fresh microcrack nucleates. Thus, a cleavage-dissolution stress corrosion cracking mechanism can be proposed.

Given that cracking has been observed to occur at temperatures as low as 450°C in this thesis, low melting point eutectics at this test temperature should be present. A melt of NaCl-$AlCl_3$ may occur in the current study, as its melting point (approximately 120°C according to Figure 74) is below 450°C; therefore, the potential role of $Cl^-$ in the embrittlement of CMSX-4 in the presence of chloride melts should be further investigated.

## 5.7 Conclusion

The conclusions of this chapter are summarised in the following bullet points.

- In the presence of 50 ppm $SO_2$ – air, it has been shown that there is a time dependency regarding the stress required to initiate cracks, where cracks initiate within 10 minutes at the highest stress region of the C-ring (~695 MPa) and takes 2 hours to observe cracks at lower stresses (~480 MPa). Longer than 2-hour exposure times do not lead to a reduction of stress required to initiate cracks. So, it is thought that threshold stress level in this NaCl assisted cracking mechanism is between 450 and 500 MPa.
- Cracks propagate rapidly within the first two hours of exposure, and negligible growth occurs after 2 hours. If the hydrogen embrittlement mechanism holds, it is thought that the negligible crack growth after 2

hours occurs due to the depletion of NaCl (which has sulphated to form $Na_2SO_4$), which in turn supresses the formation of HCl and injection of hydrogen into the alloy after approximately 2 hours of exposure.

- TEM analysis shows depletion of Ni, Co, Al, Cr, Ti, W and Ta from the near surface, which shows which elements are involved in the chlorination reaction. The mechanism of embrittlement is not well understood; however, mechanisms of embrittlement have been suggested, and further work is required to support them. The mechanisms of embrittlement may be due to hydrogen embrittlement and/or $Cl^-$.
- The effect of an external stress seems to be negligible on the scale thickness in these tests, but it does play a significant role on crack initiation and propagation.
- Cracks initiate at 450°C only at high stress locations. At these low temperatures the kinetics of sulphation, diffusion of HCl and $Cl_2$ through the oxide scale and the kinetics of metal chlorination are significantly reduced. So, if H is the embrittling source, it is thought that the reduction in kinetics of metal chloride formation may ultimately reduce the rate at which hydrogen is injected into the alloy.
- When CMSX-4 is salted with NaCl and exposed in air for 50 hours, no cracks are observed, and the thickness of the scale is significantly lower than that observed in the sulphur-containing environment. It is postulated that the effect of $SO_2/SO_3$ is critical to produce high partial pressures of $Cl_2$ at the scale/alloy interface, which promotes the formation of $AlCl_3$, $TiCl_4$ and $CrCl_3$. Chevrot [83] argues that the reaction of HCl with Al in Ti-alloy, is a way of rapidly releasing hydrogen at the alloy/scale interface and cause embrittlement. A similar effect may be observed in this study, where exposures with $SO_2/SO_3$ and NaCl lead to the chlorination of Al, Ti, Cr, Ni and Co, but exposures in air only leads to the chlorination of Ni and Co. In other words, the specific elements that are involved in the chlorination reactions dictates whether hydrogen embrittlement is observed.

# 6 Summary discussion

In the first section of this thesis, the role of a non-salted sample, a $Na_2SO_4$ salted sample and sea salt salted sample on the corrosion and crack initiation behaviour of CMSX-4 under an applied stress has been investigated. The non-salted sample did not undergo significant amount of corrosion given that the kinetics of oxidation and sulphidation at these moderate temperatures is relatively slow. Similarly, $Na_2SO_4$ also doesn't show significant degradation. From a thermodynamic point of view, this makes sense given that it is well below its melting point and also below the $NiSO_4$-$Na_2SO_4$ eutectic, typically responsible for Type II hot corrosion

There are several studies published involved in studying the effect of $Na_2SO_4$ and 80%/20% $Na_2SO_4$ – $K_2SO_4$ on the corrosion and crack initiation behaviour of nickel-based superalloys. On one hand, the work undertaken by Brooking et al. [101] proved that 80/20% $Na_2SO_4$ – $K_2SO_4$ can cause cracking in an air-300 ppm $SO_2$ environment. Based on finding sodium at the crack tip, an electrochemical mechanism was proposed to explain the observations leading to crack initiation and environmentally assisted short crack growth.

On the other hand, it has been reported by Kistler et al. [127] that $Na_2SO_4$ can cause enhanced outward nickel diffusion due to a solid-state mechanism. However, potentially due to the low concentration of salt applied in this test, no significant concentrations of NiO were observed within the deposit but, a mixed oxide/sulphide in the innermost region of the scale is observed. Even though enhanced attack was observed in the $Na_2SO_4$ salted specimen than on the $CaSO_4$ and non-salted specimen, the corrosion behaviour was not significant, and cracks were not detected.

It is evident that sea salt showed more accelerated corrosion attack than $Na_2SO_4$ and $CaSO_4$ salted specimens and that cracks are formed. Three observations were that the scale thickness was significantly greater than for the other specimens, the alkali metal chlorides had reacted with $SO_2$/$SO_3$ to form their corresponding sulphates and the chlorine was associated strongly with Al, Ti and

Cr at the oxide/alloy interface. This is consistent with the intra deposit sulphation typically observed in fireside corrosion, where the sulphation of alkali chlorides and the release of HCl and $Cl_2$ leads to the formation, vaporisation, and oxidation of metal chlorides.

Further testing using only NaCl showed that sulphur is required to significantly increase the amount of corrosion attack and for cracks to initiate at the very early stages of the exposure. It is thought that the partial pressures of $Cl_2$ present at the scale/alloy interface when testing in a sulphur-containing environment is significantly higher than when tests are undertaken in air only. The high partial pressures of $Cl_2$ at the alloy/scale interface in the presence of a sulphur-containing environment is what leads to the chlorination of elements such as Al, Ti and Cr (as well as Ni and Co but these elements require lower partial pressures of $Cl_2$ to form) and potentially may also increase the chlorination kinetics.

The effect of having small traces of moisture retained in the salt or in the atmosphere is worth studying further, as it may lead to the formation of HCl. Due to the reaction of HCl with alloying elements (particularly Al), high concentrations of $H_2$ may form at the alloy/scale interface, which may be the trigger for hydrogen embrittlement. It would be interesting to test the susceptibility of other nickel-based single crystal superalloys to the effects of NaCl and a sulphur-containing environment, such as CMSX-10 and TMS138-A. Eventually, the hydrogen embrittlement mechanism proposed is in this study suggests that the reaction of HCl with Al plays a key role in the initiation of cracks. Given that CMSX-10 and TMS138-A have similar concentrations of Al (5.7 wt% for CMSX-10 [141] and 5.9 wt% for TMS138A [142] to CMSX-4 (5.6 wt%), they would show a susceptibility to the mechanism (if hydrogen was the embrittling species). Testing other material systems with lower concentrations of Al would also help in understanding the role of this element in the stress corrosion cracking mechanism proposed in this study.

In addition, the presence of NaCl and a sulphur-containing environment leads to porous scales with low adherence and, therefore, they are non-protective. It has been observed that accelerated sulphidation occurs in these conditions.

Therefore, an additional role of NaCl in a sulphur-containing environment is to breakdown the scale in the early stages of the exposure, that leads to the inward diffusion of $SO_2/SO_3$, leading to sulphidation. It is still unclear what the role of metal sulphides ($WS_2$) is in the mechanism of crack initiation, but metal sulphides such as $WS_2$ and $ReS_2$ are extremely brittle, and previous work has shown that the crack in these metal sulphides proceed by the decohesion of Re-S or W-S bond [143]. The fact that Brooking et al. [101] found that 80/20 $Na_2SO_4/K_2SO_4$ lead to crack formation in CMSX-4, where no chlorides were present, may suggest that S plays some role in the mechanism of crack formation. The low melting point eutectic of the $Na_2SO_4/K_2SO_4$ system is 831°C (above the test temperature in this study), but the $NiSO_4$ – $Na_2SO_4$ – $K_2SO_4$ system might have a lower melting point of approximately 596°C (close to 550°C), according to differential thermal analysis (DTA) measurements undertaken by Wang et al. [144]. Therefore, a potential role of the 80/20 $Na_2SO_4/K_2SO_4$ may be to form a low melting point eutectic, that ultimately, leads to the breakdown of the protective scale, and accelerated oxidation and sulphidation. So, ultimately, the role of the salts may be to breakdown the protective oxide that forms in the initial stages of the exposure, which allows the inward diffusion of $SO_2/SO_3$ to form metal sulphides. Further work should be undertaken to prove the role of S on crack formation.

# 7 Conclusions

- No salt and $CaSO_4$ do not cause accelerated corrosion attack in CMSX-4 when exposed in a 50 ppm $SO_2$ – air environment at 550°C and cracks do not form in 400 hours of exposure when an external stress of 700 MPa is applied.
- $Na_2SO_4$ showed a more accelerated attack in CMSX-4 than $CaSO_4$ and the non-salted sample. The corrosion morphology is akin to that observed in the proposed solid-state mechanism at 550°C. In the gaseous atmosphere 50 ppm $SO_2$ – air gaseous at 550°, it is thought that $Na_2SO_4$ does not play an important role in crack formation in 400 hours of exposure when an external stress of 700 MPa is applied. However, for future work, longer exposure times should be tested to investigate the role of $Na_2SO_4$ on crack initiation.
- Sea salt is the most aggressive salt in terms of corrosion attack of CMSX-4 in a 50 ppm $SO_2$ – air environment at 550°C. The chlorination and oxidation of Ni, Co, Ti, Cr and Al was observed, which may have led to the accelerated corrosion rates.
- Further testing with only NaCl salt (which represents approximately 75 wt% of sea salt) showed that both $SO_2/SO_3$ and stress are required to form cracks within 10 minutes of the exposure. Based on the EDS maps, it is proposed that the presence of $SO_2/SO_3$ leads to the rapid formation of $Na_2SO_4$ and, therefore, the release of HCl and $Cl_2$. The rapid release of HCl and $Cl_2$ then creates high partial pressures of $Cl_2$ at the alloy/scale interface that are required to chlorinate elements such as Al, Ti and Cr.
- The scales observed in the presence of NaCl and $SO_2/SO_3$ are porous and tend to spall, which may have led to the inward diffusion of oxygen and sulphur, and therefore, accelerated oxidation and sulphidation.
- As reported by Chevrot [83], the reactions of HCl with Al in Ti-alloys is important in releasing large amounts of hydrogen at the scale/alloy interface in a short amount of time, leading to hydrogen embrittlement. Potentially, a similar mechanism may be observed in this study with Ni-

based superalloys. However, further work is required to prove or disprove hydrogen as the embrittling species in this study.

- Crack growth rate is significantly reduced after two hours of exposure. Potentially, this may be due to a reduction of available HCl and $Cl_2$ as most of the NaCl has reacted with $SO_2/SO_3$ to form $Na_2SO_4$ by that time. The suppression of HCl will also supress the chlorination reactions and therefore, the formation of $H_2$ at the alloy/scale interface.
- This mechanism has been observed at 450°C, so this mechanism extends to temperature between 450-550°C.

# 8 Suggestions for further work

This study has raised a number of unanswered questions regarding the mechanisms of near surface weakening. Experiments to prove or disprove the role of hydrogen should be undertaken. Some suggestions for future testing are as follows.

- The first suggestion is to attempt removing water inclusions retained in the salt and examining its effect on the embrittlement of the alloy. As investigated previously in HSSCC on Ti alloys, the sample and the salt could be baked in the furnace for 7 days to minimise the concentration of water inclusions retained in the salt. This would supress the formation of HCl, and form $Cl_2$ instead. As a result, the formation of metal chlorides would not lead to a significant amount of hydrogen injection into the alloy and would supress crack initiation, if it is due to high temperature $H_2$ embrittlement.

  A research test plan should be undertaken, where the concentration of water crystallisation in the salt can be measured before the baking procedure and afterwards using infrared (IR) spectroscopy. The fact that using this method supressed crack initiation in previous studies shows partial evidence of hydrogen embrittlement in HSSCC in Ti alloys, and it is thought that it may prove beneficial in the NaCl assisted mechanism reported in this thesis.
- Tests should be undertaken in HCl only, to examine whether the fracture surface in HCl can replicate the fracture surface generated when samples are deposited with NaCl and exposed in an $SO_2$ – containing atmosphere.
- Tests should be done at a pressure of 30 bar to see if the injection of H is suppressed. This test would have significant implications for in-service turbine blades as they operate at high pressures.
- If the H embrittlement holds true, the physical mechanism of embrittlement should be studied. In particular any evidence of hydrogen-induced localised plasticity or decohesion should be investigated.

- Attempts should be made to find a relationship between fractographic appearance and hydrogen embrittlement.
- Examination of gaseous products formed during the exposure could be done using mass spectroscopic analysis. This would help validate the concentrations of HCl and $Cl_2$ formed predicted by FactSage 8.1, which ultimately form a key part in the hydrogen embrittlement mechanism proposed in this study.
- Using isotopes of deuterium could be used to track hydrogen in the alloy after the exposure. One way to do this could be using NaCl in a heavy water solution (water composed of $D_2O$) to spray the salt onto the surface of the C-ring before the exposure. Characterisation techniques, such as TOF-SIMS, NanoSims or atom probe tomography (APT) could be used identify potential trapping sites of deuterium (e.g. dislocations).
- Although still in the early stages of investigation, the role of dendrites on the crack initiation mechanism needs to be further explored. This is based on some nano XCT work undertaken with ZEISS, that seem to show cracks aligned with the interface between the dendritic and interdendritic region of CMSX-4 (see Figure 77). This observation was not clear enough to make an accurate statement and further microscopy work should be undertaken to confirm. If the interface between the dendritic and interdendritic region is preferentially attacked, work should be done to understand the mechanism further. Potentially, the local misfit stresses in the interface between the dendritic and interdendritic region may

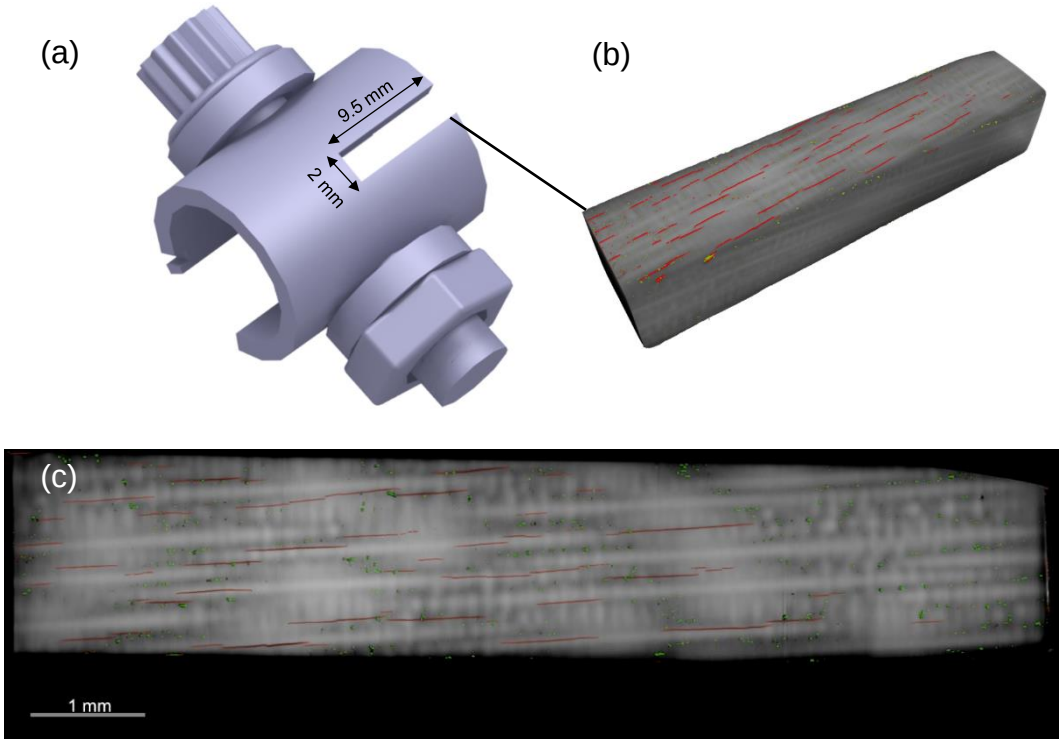


*Figure 77 – (a) Image showing the dimensions of the section taken for nano XCT examination, (b) side view of nano XCT reconstruction and (c) top view of the nano XCT reconstruction*

# 9 References


[1] Li Muzi, “Characterization and modelling of the mechanical properties of the isolated phases in γ/γ’ microstructures,” Imperial College London, 2017.

[2] R. C. Reed, *The Superalloys: Fundamentals and Applications*. Cambridge, United Kingdom: Cambridge University Press, 2006.

[3] A. Evangelou, “Oxidation-fatigue mechanisms at moderate service temperatures in single crystal turbine blade materials,” University of Southampton, 2017.

[4] A. Gregori, “Survey of welding and repairing of nickel super-alloys for gas turbines.” 2003.

[5] A. Sengupta *et al.*, “Tensile behavior of a new single-crystal nickel-based superalloy (CMSX-4) at room and elevated temperatures,” *J. Mater. Eng. Perform.*, vol. 3, no. 1, pp. 73–81, Feb. 1994.

[6] P. H. Thorton, R. G. Davies, and T. L. Johnston, “The temperature dependence of the flow stress of the γ’ phase based upon Ni3Al,” *Metall. Mater. Trans. A*, vol. 1, pp. 207–218, 1970.

[7] M. B. Krisak, B. I. Bentley, A. W. Phelps, and T. C. Radsick, “Review of Calcium Sulfate as an Alternative Cause of Hot Corrosion,” *J. Propuls. Power*, vol. 33, no. 3, 2017.

[8] A. S. Khanna, *Introduction to high temperature oxidation and corrosion*. ASM International, 2002.

[9] N. Birks, G. H. Meier, and F. . Pettit, *Introduction to the high temperature oxidation of metals*, 2nd Editio. Cambridge University Press, 2006.

[10] J. Phother-Simon, “High Temperature Corrosion of Superheaters in Biomass- and Waste-Fired Boilers: Combat on two fronts,” CHALMERS UNIVERSITY OF TECHNOLOGY, 2019.

[11] D. J. Young, *High temperature oxidation and corrosion of metals*. Elsevier,

2008.

[12] P. Kofstad, *High temperature corrosion*, no. 7. John Wiley & Sons, Ltd, 1988.

[13] P. Heitjans and J. Kärger, “Diffusion in condensed matter: Methods, materials, models,” *Diffus. Condens. Matter Methods, Mater. Model.*, pp. 1–965, 2005.

[14] H. T. Mallikarjuna, W. F. Caley, and N. L. Richards, “Oxidation Kinetics and Oxide Scale Characterization of Nickel-Based Superalloy IN738LC at 900 °C.”

[15] J. Klöwer, U. Brill, and U. Heubner, “High temperature corrosion behaviour of nickel aluminides: effects of chromium and zirconium,” *Intermetallics*, vol. 7, no. 10, pp. 1183–1194, 1999.

[16] A. Atkinson and R. I. Taylor, “The diffusion of Ni in the bulk and along dislocations in NiO single crystals,” *Philos. Mag. A Phys. Condens. Matter, Struct. Defects Mech. Prop.*, 1979.

[17] C. K. Kim and L. W. Hobbs, “Microstructural evidence for short-circuit oxygen diffusion paths in the oxidation of a dilute Ni-Cr alloy,” *Oxid. Met.*, 1996.

[18] R. Haugsrud, “On the influence of sol-gel derived CeO2 coatings on high-temperature oxidation of Co, Ni and Cu,” *Corros. Sci.*, 2002.

[19] H. Long *et al.*, “Effect of lattice misfit on the evolution of the dislocation structure in Ni-based single crystal superalloys during thermal exposure,” *Acta Mater.*, vol. 120, pp. 95–107, Nov. 2016.

[20] A. Evangelou, K. A. Soady, S. Lockyer, N. Gao, and P. A. S. Reed, “On the mechanism of oxidation-fatigue damage at intermediate temperatures in a single crystal Ni-based superalloy,” *Mater. Sci. Eng. A*, vol. 742, pp. 648–661, Jan. 2019.

[21] K. N. Strafford, “The sulphidation of metals and alloys,” *Metall. Rev.*, vol.

14, no. 1, pp. 153–174, 1969.

[22] C. Grosenick, “Sulphidation: High temperature turbine blade corrosion,” 2003. [Online]. Available: https://www.aviationpros.com/home/article/10387209/sulfidation-high-temperature-turbine-blade-corrosion.

[23] B. Gleeson, “Alloy degradation under oxidizing-sulfidizing conditions at elevated temperatures,” *Mater. Res.*, vol. 7, no. 1, pp. 61–69, Mar. 2004.

[24] M. R. Wootton and N. Birks, “The oxidation of nickel in atmospheres containing sulphur dioxide,” *Corros. Sci.*, vol. 12, no. 11, 1972.

[25] K. Przybylski and S. Mrowec, “High temperature sulfide corrosion and transport properties of transition metal sulfides,” in *JAERI*, 2003, pp. 1–8.

[26] D. Young, *High temperature oxidation and corrosion of metals*. ElsevierCorrosion Series, 2008.

[27] S. Mrowec and J. Janowski, “Similarities and Differences in Defect Dependent Properties of Transition Metal Sulphides and Oxides,” in *Studies in Inorganic Chemistry*, vol. 9, no. C, 1989, pp. 55–99.

[28] A. Jalowicka, W. J. Nowak, D. Naumenko, and W. J. Quadakkers, “Effect of SO2 addition on air oxidation behaviour of CM247 and CMSX-4 at 1050C,” *Model. Mater. Extrem. Environ.*, vol. 68, no. 11, pp. 2776–2785, 2016.

[29] A. Jalowicka, W. Nowak, D. Naumenko, L. Singheiser, and W. J. Quadakkers, “Effect of nickel base superalloy composition on oxidation resistance in SO2 containing, high pO2 environments,” *Mater. Corros.*, vol. 65, no. 2, pp. 178–186, 2014.

[30] F. Petit, “Hot corrosion of metals and alloys,” *Oxid. Met.*, vol. 76, no. 1–21, 2011.

[31] X. Zheng and R. A. Rapp, “Electrochemical impedance of a platinum electrode in fused Na2SO4 melts in SO2-O2 environments,” *J.*

*Electrochem. Soc.*, vol. 24, pp. 303–310, 1993.

[32] J. Stringer, “High temperature corrosion of superalloys,” *Mater. Sci. Technol.*, vol. 3, no. 7, pp. 482–493, 1987.

[33] R.L. Jones, “Hot Corrosion in Gas Turbines.” Washington D.C., pp. 3–29, 1983.

[34] K. P. Lillerud and P. Kofstad, “Sulfate-Induced Hot Corrosion of Nickel,” *Oxid. Met.*, vol. 21, no. 5, 1984.

[35] F. S. Pettit and G. H. Meier, “OXIDATION AND HOT CORROSION OF SUPERALLOYS,” Pittsburgh, 1984.

[36] I. Gurrappa, I. V. . Yashwanth, I. Mounika, H. Murakami, and S. Kuroda, “The importance of hot corrosion and its effective prevention for enhanced efficiency of gas turbines,” in *Gas Turbines - Materials, Modelling and Performance*, 2015.

[37] J. Sumner, A. Encinas-Oropesa, N. J. Simms, and J. R. Nicholls, “Type II Hot Corrosion: Kinetics Studies of CMSX-4,” *Oxid. Met.*, vol. 80, no. 5–6, pp. 553–563, Dec. 2013.

[38] A. Potter, “Hot Corrosion in Industrial Gas Turbines,” Cranfield University, 2018.

[39] G. H. Meier, “A review of advances in high-temperature corrosion,” *Mater. Sci. Eng. A*, vol. 120–121, no. PART 1, pp. 1–11, Nov. 1989.

[40] A. Encinas-Oropesa, “Study of hot corrosion in single crystal nickel based superalloys and platinum-aluminide coatings,” 2005.

[41] J. A. Goebel, F. S. Pettit, and G. W. Goward, “Mechanisms for the Hot Corrosion of Nickel-Base Alloys.”

[42] P. D. Jose, “Solubility of α-Al2O3 in Fused Na2SO4 at 1200 K,” *J. Electrochem. Soc.*, vol. 132, no. 3, p. 735, Jun. 2006.

[43] A. K. Misra, D. P. Whittle, and W. L. Worrell, “Thermodynamics of Molten

Sulfate Mixtures," *J. Electrochem. Soc.*, vol. 129, no. 8, pp. 1840–1845, 1982.

[44] S. Shih, Y. Zhang, and X. Li, "Sub-melting point hot corrosion of alloys and coatings," *Mater. Sci. Eng. A*, vol. 120–121, no. PART 1, pp. 277–282, Nov. 1989.

[45] E. Kistler, W. T. Chen, G. H. Meier, and B. Gleeson, "A new solid-state mode of hot corrosion at temperatures below 700°C," *Mater. Corros.*, vol. 70, no. 8, pp. 1346–1359, Aug. 2019.

[46] M. Zhu, H. Ma, M. Wang, Z. Wang, and A. Sharif, "Effects of Cations on Corrosion of Inconel 625 in Molten Chloride Salts," *High Temp. Mater. Process.*, vol. 35, no. 4, pp. 337–345, Apr. 2016.

[47] C. Schwalm and M. Schütze, "The corrosion behavior of several heat resistant materials in air + 2 vol-% Cl2 at 300 to 800 °C. Part I - Fe-base and Fe-containing alloys," *Mater. Corros.*, vol. 51, no. 1, pp. 34–49, Jan. 2000.

[48] Y. N. Chang and F. I. Wei, "High-temperature chlorine corrosion of metals and alloys - A review," *Journal of Materials Science*, vol. 26, no. 14. Kluwer Academic Publishers, pp. 3693–3698, Jul-1991.

[49] H. P. Nielsen, F. J. Frandsen, K. Dam-Johansen, and L. L. Baxter, "Implications of chlorine-associated corrosion on the operation of biomass-fired boilers," *Progress in Energy and Combustion Science*, vol. 26, no. 3. Elsevier Science Ltd, pp. 283–298, 2000.

[50] R. Prescott, "No Title," University of Manchester, 1986.

[51] C. Proff, T. Jonsson, C. Pettersson, J.-E. Svensson, L.-G. Johansson, and M. Halvarsson, "Microstructural investigation of the KCl-induced corrosion of the austenitic alloy Sanicro 28 (35Fe27Cr31Ni) at 600C," *Mater. High Temp.*, vol. 26, no. 2, 2009.

[52] Y. Zeng, K. Li, R. Hughes, and J.-L. Luo, "Corrosion Mechanisms and

Materials Selection for the Construction of Flue Gas Component in Advanced Heat and Power Systems," 2017.

[53] H. J. Grabke, M. Spiegel, and A. Zahs, "Role of alloying elements and carbides in the chlorine-induced corrosion of steels and alloys," *Mater. Res.*, vol. 7, no. 1, pp. 89–95, Mar. 2004.

[54] M. Spiegel, "Reactions between gas phase, deposits and metallic materials in chlorine containing atmospheres Reactions between gas phase, deposits and metallic materials in chlorine containing atmospheres," *Mater. High Temp.*, 1997.

[55] L. Krumm and M. C. Galetz, "Impact of Deposits and Their Morphology on the Active Corrosion of Iron in Chlorine- and Sulfur-Containing Atmospheres in the Temperature Range of 350–500 °C."

[56] G. K, B. P, J. P, M. J, M. M, and M. E, "High temperature corrosion in biomass incineration plants," 1997.

[57] H. N, L. OH, B. R, and I. S, "High-temperature corrosion when co-firing coal and straw in pulverized coal boilers and circulating fluidized bed boilers," in *VGB Conference. Corrosion and Corrosion Protection in Power Plants*, 1995.

[58] S. Ozawa, K. Naruse, K. Ito, Y. Kojimo, H. M. Endo, and T. Yanase, "Evolution of HCl from KCl, CaCl2 and NaCl in an SO2-O2-H2O atmosphere under a simulated condition of municipal wastes incineration," *J. Chem. Eng. Japan*, vol. 36, no. 7, pp. 867–873, 2003.

[59] P. Tang, Y. C. Zhao, D. Z. Chen, and F. Y. Xia, "Volatility of heavy metals during incineration of tannery sludge in the presence of chlorides and phosphoric acid," *Waste Manag. Res.*, vol. 26, no. 4, pp. 369–376, Aug. 2008.

[60] F. J. Frandsen, "Ash formation, deposition and corrosion when utilizing straw for heat and power production," Technical University of Denmark, 2010.

[61] M. Broström, *Aspects of alkali chloride chemistry on deposit formation and high temperature corrosion in biomass and waste fired boilers*. 2010.

[62] D. Liu, W. Li, and S. Li, “Fundamental study of heterogeneous KCl sulfation under oxy-fuel combustion conditions,” *Int. J. Energy Res.*, vol. 43, no. 9, pp. 4093–4103, Jul. 2019.

[63] T. J. Pan and Y. Niu, “Internal attack of Fe–xCr–10Al alloys induced by the presenceof chlorine and sulfur in a reducing atmosphere at 973 K,” *Scr. Mater.*, vol. 57, pp. 97–100, 2007.

[64] T. J. Pan, F. Gesmundo, and Y. Niu, “Corrosion behavior of three iron-based model alloys in reducing atmospheres containing HCl and H2S at 600 °C,” *Corros. Sci.*, vol. 49, no. 3, pp. 1362–1377, Mar. 2007.

[65] H. H. Krause, “High Temperature Corrosion Problems in Waste Incineration Systems.”

[66] G. HJ, “Incinerating municipal andindustrial waste.” New York, p. 161, 1989.

[67] N. Hiramitsu, Y. Uematsu, T. Tanaka, and M. Kinugasa, “Effects of Alloying Elements on NaCl-induced Hot Corrosion of Stainless Steels,” *Mater. Sci. Eng. A*, vol. 120–121, pp. 319–328, 1989.

[68] Y. Liu, W. Fan, X. Wu, and X. Zhang, “Chlorine-Induced High-Temperature Corrosion of Boiler Steels Combusting Sha Erhu Coal Compared to Biomass,” 2018.

[69] N. Israelsson, • K A Unocic, • K Hellström, J.-E. Svensson, and L.-G. Johansson, “Cyclic Corrosion and Chlorination of an FeCrAl Alloy in the Presence of KCl.”

[70] E. Sadeghimeresht, L. Reddy, T. Hussain, N. Markocsan, and S. Joshi, “Chlorine-induced high temperature corrosion of HVAF-sprayed Ni-based alumina and chromia forming coatings,” *Corros. Sci.*, vol. 132, pp. 170–184, Mar. 2018.

[71] J. Pettersson *et al.*, “The effects of KCl, K2SO4 and K2CO3 on the high temperature corrosion of a 304-Type austenitic stainless steel,” *Oxid Met*, vol. 76, pp. 93–109, 2011.

[72] J. Sui, J. Lehmusto, M. Bergelin, and M. Hupa, “The Effects of KCl, NaCl and K2CO3 on the High-Temperature Oxidation Onset of Sanicro 28 Steel,” *Oxid. Met.*, vol. 85, no. 5–6, pp. 565–598, Jun. 2016.

[73] N. Israelsson, • K Hellström, J.-E. Svensson, and L.-G. Johansson, “KCl-Induced Corrosion of the FeCrAl Alloy Kanthal Ò AF at 600 °C and the Effect of H 2 O.”

[74] M. K. Hossain and S. R. J. Saunders, “A Microstructural Study of the Influence of NaCl Vapor on the Oxidation of a Ni-Cr-Al Alloy at 850~,” 1978.

[75] R. Prescott, F. H. Stott, and P. Elliottt, “Investigations of the Degradation of High-Temperature Alloys in a Potentially Oxidizing-Chloridizing Gas Mixture,” 1989.

[76] N. Folkeson, “Chlorine induced corrosion in biomass and waste fired boilers: Laboratory and field investigations,” Chalmers University of Technology, 2010.

[77] S. C. Okoro, M.; Montgomery, F. Jappe Frandsen, and K.; Pantleon, “Effect of Water Vapor on High-Temperature Corrosion under Conditions Mimicking Biomass Firing,” *Energy & Fuels*, vol. 29, no. 9, pp. 5802–5815, 2015.

[78] F. Wang and Y. Shu, “Influence of Cr Content on the Corrosion of Fe-Cr Alloys: The Synergistic Effect of NaCl and Water Vapor,” 2003.

[79] Z. Zeng, K. Natesan, Z. Cai, and D. J. Gosztola, “Effects of Chlorine in Ash on the Corrosion Performance of Ni-Based Alloys in a Simulated Oxy-Fuel Environment,” 2018.

[80] S. C. Cha and M. Spiegel, “Local reactions of KCl particles with iron, nickel and chromium surfaces,” *Mater. Corros.*, vol. 57, no. 2, pp. 159–164, Feb.

2006.

[81] C. C. Tsaur, J. C. Rock, C. J. Wang, and Y. H. Su, “The hot corrosion of 310 stainless steel with pre-coated NaCl/Na 2so4 mixtures at 750°C,” *Mater. Chem. Phys.*, vol. 89, no. 2–3, pp. 445–453, Feb. 2005.

[82] S. Joseph, T. C. Lindley, D. Dye, and E. A. Saunders, “The mechanisms of hot salt stress corrosion cracking in titanium alloy Ti-6Al-2Sn-4Zr-6Mo,” *Corros. Sci.*, vol. 134, pp. 169–178, Apr. 2018.

[83] T. Chevrot, “Pressure effects on the hot-salt stress-corrosion cracking of titanium alloys,” Cranfield University, 1994.

[84] A. Hatch, H. Rosenberg, and E. Erbin, “Effects of Environment on Cracking in Titanium Alloys,” *Stress. Crack. Titan.*, pp. 122-122–15, Aug. 1996.

[85] R. S. Ondrejcin, C. L. Selb, and S. P. Rideout, “Role of Chloride in Hot-Salt Stress-Corrosion Cracking of Titanium-Aluminium Alloys,” 1967.

[86] G. Lapasset, “Etude de la corrosion sous tension a chaud de l’alliage TA6V par le chlorure de sodium,” *La Rech. Aerosp.*, no. No.4, pp. 255–261, 1973.

[87] H. L. Logan, “Studies of hot salt cracking of the titanium 8 percent Al-1 percent Mo-1 percent V alloy.,” in *FUNDAMENTAL ASPECTS OF STRESS CORROSION CRACKING*, 1969, pp. 662–672.

[88] C. K. Kim and L. W. Hobbs, “Identification of Diffusing Species and the Dynamic Nature of Diffusion Paths During Oxidation of a Dilute Ni-Cr Alloy,” 1997.

[89] H. V. Atkinson, “A review of the role of short-circuit diffusion in the oxidation of nickel, chromium, and nickel-chromium alloys,” *Oxidation of Metals*, vol. 24, no. 3–4. Kluwer Academic Publishers-Plenum Publishers, pp. 177–197, Oct-1985.

[90] C. Bruns and M. Schütze, “Investigation of the Mechanical Properties of Oxide Scales on Nickel and TiAl,” 2001.

[91] V. K. Tolpygo and H. Viefhaus[2], “Segregation at the Al2O3± FeCrAl

Interface During High-Temperature Oxidation," 1999.

[92] R. Jiang, "Study of Fatigue Crack Initiation and Propagation Mechanisms in an Advanced Ni-based Superalloy: Effects of Microstructures and Oxidation," Southampton University, 2015.

[93] B. R. Barnard, P. K. Liaw, R. A. Buchanan, and D. L. Klarstrom, "Effects of applied stresses on the isothermal and cyclic high-temperature oxidation behavior of superalloys," *Mater. Sci. Eng. A*, vol. 527, no. 16–17, pp. 3813–3821, Jun. 2010.

[94] G. Calvarin-Amiri, R. Molins, and A. M. Huntz, "Effect of the application of a mechanical load on the oxide-layer microstructure and on the oxidation mechanism of Ni-20Cr foils," *Oxid. Met.*, vol. 53, no. 3, pp. 399–426, 2000.

[95] H. J. Christ, K. Wackerman, and U. Krupp, "On the mechanism of dynamic embrittlement and its effect on fatigue crack propagation in IN718 at 650°C," *Procedia Struct. Integr.*, vol. 2, pp. 557–564, 2016.

[96] U. Krupp, W. M. Kane, C. Laird, and C. J. McMahon, "Brittle intergranular fracture of a Ni-base superalloy at high temperatures by dynamic embrittlement," *Mater. Sci. Eng. A*, vol. 387–389, no. 1-2 SPEC. ISS., pp. 409–413, Dec. 2004.

[97] R. Jiang *et al.*, "Role of oxygen in enhanced fatigue cracking in a PM Ni-based superalloy: Stress assisted grain boundary oxidation or dynamic embrittlment?," *Corros. Sci.*, vol. 139, pp. 141–154, Jul. 2018.

[98] H. S. Kitaguchi *et al.*, "Oxidation ahead of a crack tip in an advanced Ni-based superalloy," *Acta Mater.*, vol. 61, no. 6, pp. 1968–1981, Apr. 2013.

[99] U. Krupp, W. Kane, J. A. Pfaendtner, X. Liu, C. Laird, and C. J. Mcmahon, "Oxygen-Induced Intergranular Fracture of the Nickel-Base Alloy IN718 during Mechanical Loading at High Temperatures 35," 2004.

[100] Z. Sun, C. Laitem, and A. Vincent, "Dynamic embrittlement at intermediate temperature in a Cu-Ni-Si alloy," *Mater. Sci. Eng. A*, vol. 477, no. 1–2, pp.

145–152, Mar. 2008.

[101] L. Brooking *et al.*, “Analysis of combined static load and low temperature hot corrosion induced cracking in CMSX-4 at 550°C,” *Corros. Sci.*, vol. 163, Feb. 2020.

[102] D. Siebörger, H. Knake, and U. Glatzel, “Temperature dependence of the elastic moduli of the nickel-base superalloy CMSX-4 and its isolated phases,” *Mater. Sci. Eng. A*, vol. 298, no. 1–2, pp. 26–33, Jan. 2001.

[103] L. G. Bland and J. S. Locke, “Chemical and electrochemical conditions within stress corrosion and corrosion fatigue cracks,” *npj Mater. Degrad.*, vol. 1, no. 1, p. 12, Dec. 2017.

[104] I.H. Craig, “Some mechanistic aspects of the environmental sensitive cracking of an 18Ni maraging steel,” Newcastle University, 1977.

[105] J. P. Gibbs, “Stress corrosion cracking and crack tip characterization of alloy X-750 in light water reactor environments,” Massachusetts Institute of Technology, 2012.

[106] H. Sheng, C.-F. Dong, K. Xiao, X.-G. Li, and L. Lu, “Anodic dissolution of a crack tip at AA2024-T351 in 3.5wt% NaCl solution,” *Int. J. Miner. Metall. Mater.*, vol. 19, no. 10, 2012.

[107] J. Yahalom and A. Aladjem, *Stress-corrosion cracking*, First. Freund Publishing House, 1980.

[108] R. E. Ricker and D. J. Ducuette, “The role of environment on time dependent crack growth,” New York, 1981.

[109] Y. F. Cheng, *Stress corrosion cracking of pipelines*. John Wiley and Sons Ltd, Wiley-Blackwell, 2013.

[110] X. Mao and D. Li, “Slip-step dissolution and micromechanical analysis to model stress-corrosion crack growth of type 321 stainless steel in boiling mgci2,” *Metall. Mater. Trans. A*, vol. 26, no. 3, pp. 641–646, Mar. 1995.

[111] O. F. Aly and M. M. Neto, “The slip-step dissolution and film rupture model

- A critical review and an alternative modelling proposal," *Trans. SMiRT*, vol. 22, 2013.

[112] C. Benedicks, "The 'wetting effect' strongly affecting the tensile strength of solids; 'Liquo-striction', A new effect resulting," in *Pittsburgh International Conference on Surface Reactions*, 1948, pp. 196–201.

[113] H. H. Uhlig, "New perspectives in the stress corrosion problem," in *Physical Metallurgy of Stress Corrosion Fracture*, T. Rhodin, Ed. New York, 1959, pp. 1–17.

[114] S. P. Lynch, "Mechanisms of liquid metal embrittlement and stress corrosion cracking in high-strength aluminium alloys and other materials," in *Mechanisms of Environment Sensitive Cracking of Materials*, P.R. Swann., The Metals Society, 1977, pp. 201–212.

[115] R. E. Ricker, J. L. Fink, J. S. Harris, and A. J. Shapiro, "Evidence for film-induced cleavage in rhodium plated nickel," *Scr. Metall. Mater.*, vol. 26, no. 7, pp. 1019–1023, Apr. 1992.

[116] A. Barnes, N. Senior, and R. C. Newman, "Revisiting the film-induced cleavage model of SCC," *Environ. Crack. Mater.*, pp. 47–57, Jan. 2008.

[117] M. P. Seah, "INTERFACE ADSORPTION, EMBRITTLEMENT AND FRACTURE IN METALLURGY - A REVIEW," *Surf. Sci.*, vol. 1975, pp. 168–212.

[118] R. P. Messmer and C. L. Briant, "The role of chemical bonding in grain boundary boundary embrittlement," *Acta Met.*, vol. 30, pp. 457–467, 1981.

[119] J. Shin and C. J. J. Mcmahon, "Mechanisms of stress relief cracking in a ferritic steel," *Acta Met.*, vol. 32, no. 9, pp. 1535–1552, 1984.

[120] M. T. Lapington, "High Resolution Characterisation of Oxidation Mechanisms in Polycrystalline Nickel Based Superalloys," Oxford University, 2019.

[121] "ISO - ISO 7539-5:1989 - Corrosion of metals and alloys — Stress

corrosion testing — Part 5: Preparation and use of C-ring specimens." [Online]. Available: https://www.iso.org/standard/14318.html. [Accessed: 06-Jan-2020].

[122] S. J. P. J.K. Thomson, "A Comparison of the C-Ring Test and the Jones Test as Standard Practice Test Methods for Studying Stress Corrosion Cracking in Ferritic Steels," in *NACE International Corrosion 2015*, 2015, pp. 1–11.

[123] L. Brooking, J. Sumner, S. Gray, and N. J. Simms, "Stress corrosion of Ni-based superalloys," *Mater. high Temp.*, vol. 35, no. 3, pp. 120–129, 2018.

[124] N. Chapman, S. Gray, J. Sumner, and J. Nicholls, "Stress Corrosion Testing of CMSX-4, CM247LC DS and IN6203DS Ni-Base Superalloys," *Oxid. Met.*, vol. 95, no. 1–2, pp. 85–104, Feb. 2021.

[125] D. Tomus and H. P. Ng, "In situ lift-out dedicated techniques using FIB-SEM system for TEM specimen preparation," *Micron*, vol. 44, no. 1, pp. 115–119, Jan. 2013.

[126] L. Gianuzzi and F. Stevie, "A review of focused ion beam milling techniques for TEM specimen preparation." pp. 197–204, 1999.

[127] E. Kistler, W.-T. Chen, G. H. Meier, and B. Gleeson, "A new solid-state mode of hot corrosion at temperatures below 700°C," *Mater. Corros.*, vol. 70, no. 8, 2019.

[128] A. Jardnas, J. E. Svensson, and L. G. Johansson, "The inhibitive effect of traces of SO2 on the oxidation of Iron," *Oxid. Met.*, vol. 60, no. 5/6, 2003.

[129] Z. L. Coull, "Exploring De-alloying in Fe-Ni-Cr Alloys and its Relationship to Stress Corrosion Cracking in Nuclear High Temperature Water Environments," University of Toronto, 2010.

[130] M. Martín, S. Weber, and W. Theisen, "A thermodynamic approach for the development of austenitic steels with a high resistance to hydrogen gas embrittlement," *Int. J. Hydrogen Energy*, vol. 38, no. 34, pp. 14887–14895,

Nov. 2013.

[131] J. Peng *et al.*, “Effect of platinum and pre-oxidation on the hot corrosion behavior of aluminide coating with NaCl at 1050 °c,” *Mater. Res. Express*, vol. 7, no. 11, p. 116402, Nov. 2020.

[132] S. Karlsson, T. Jonsson, J. Hall, J. E. Svensson, and J. Liske, “Mitigation of fireside corrosion of stainless steel in power plants: A laboratory study of the influences of SO2 and KCl on initial stages of corrosion,” *Energy and Fuels*, vol. 28, no. 5, pp. 3102–3109, May 2014.

[133] J. C. Shiloff, “Thermal analysis of the chromous chloride-sodium chloride system,” *J. Phys. Chem.*, vol. 64, no. 10, pp. 1566–1567, 1960.

[134] S. C. Okoro, S. Kiamehr, M. Montgomery, F. J. Frandsen, and K. Pantleon, “Effect of flue gas composition on deposit induced high temperature corrosion under laboratory conditions mimicking biomass firing. Part II: Exposures in SO2 containing atmospheres,” *Mater. Corros.*, vol. 68, no. 5, pp. 515–528, May 2017.

[135] Y. Shinata, “Accelerated Oxidation Rate of Chromium Induced by Sodium Chloride,” 1987.

[136] H. J. Grabke, E. Reese, and M. Spiegel, “The effects of chlorides, hydrogen chloride, and sulfur dioxide in the oxidation of steels below deposits,” *Corros. Sci.*, vol. 37, no. 7, pp. 1023–1043, 1995.

[137] M. Paneru, G. Stein-Brzozowska, J. Rg Maier, and G. Nter Scheffknecht, “Corrosion Mechanism of Alloy 310 Austenitic Steel beneath NaCl Deposit under Varying SO 2 Concentrations in an Oxy-fuel Combustion Atmosphere,” 2013.

[138] Y. Sun and Y. F. Cheng, “Thermodynamics of spontaneous dissociation and dissociative adsorption of hydrogen molecules and hydrogen atom adsorption and absorption on steel under pipelining conditions,” *Int. J. Hydrogen Energy*, vol. 46, no. 69, pp. 34469–34486, Oct. 2021.

[139] Q. Gao, Y. Lu, Y. Yang, Y. Wu, C. Zhang, and Z. Fan, “Are unexpected chloride ions in molten salt really harmful to stainless steel?,” *J. Energy Storage*, vol. 54, 2022.

[140] L. Zhu and Y. Li, “Cleavage-dissolution assisted stress corrosion cracking underelastic loads,” *Mater. Degrad.*, vol. 5, no. 1, 2021.

[141] Q. Ding, H. Bei, X. Zhao, Y. Gao, and Z. Zhang, “Processing, Microstructures and Mechanical Properties of a Ni-Based Single Crystal Superalloy,” *Cryst. 2020, Vol. 10, Page 572*, vol. 10, no. 7, p. 572, Jul. 2020.

[142] C. Chen, Q. Wang, C. Dong, Y. Zhang, and H. Dong, “Composition rules of Ni-base single crystal superalloys and its influence on creep properties via a cluster formula approach,” *Sci. Rep.*, vol. 10, no. 1, Dec. 2020.

[143] X. Chen *et al.*, “Pristine edge structures of T’’-phase transition metal dichalcogenides (ReSe2, ReS2) atomic layers.,” *Nanoscale*, 2020.

[144] Y. Wang *et al.*, “Comparison of Na2SO4, K2SO4 and Na2SO4-K2SO4 deposit induced hot corrosion of a β-NiAl coating,” *Corros. Sci.*, vol. 198, Apr. 2022.